Efficient Heterojunction Strategies in Multinary Sulfide Based Semiconductors for Enhanced Photocatalytic Performance

A Thesis Submitted to the
Indian Institute of Technology Guwahati
as Partial Fulfilment for the Degree of
DOCTOR of PHILOSOPHY

By

Gaurangi Gogoi

Department of Chemistry
Indian Institute of Technology Guwahati
Guwahati – 781039, Assam, India

April 2019

Efficient Heterojunction Strategies in Multinary Sulfide Based Semiconductors for Enhanced Photocatalytic Performance

A Thesis Submitted to the
Indian Institute of Technology Guwahati
as Partial Fulfilment for the Degree of

DOCTOR of PHILOSOPHY

By

Gaurangi Gogoi

Roll No. 136122031

Department of Chemistry
Indian Institute of Technology Guwahati
Guwahati – 781039, Assam, India

April 2019

STATEMENT

I hereby declare that this thesis entitled, "**Efficient Heterojunction Strategies in Multinary Sulfide Based Semiconductors for Enhanced Photocatalytic Performance**" is the outcome of research work carried out by me under the supervision of Prof. Mohammad Qureshi, at the Department of Chemistry, Indian Institute of Technology Guwahati, Assam, India, for the award of the degree of Doctor of Philosophy.

Research findings reported in this thesis based on the results of other investigators has been duly cited and acknowledged. To the best of my knowledge, the set of work described in this thesis is original and has not been submitted elsewhere for any degree or diploma.

Guwahati
April, 2019

Gaurangi Gogoi
(Candidate)
Department of Chemistry
IIT Guwahati
Guwahati- 781039, Assam
India

Dr. Mohammad Qureshi
Professor
Department of Chemistry
Indian Institute of Technology, Guwahati
781039 – India
Tel: +91 – 361 – 2582320
Fax: +91 – 361 – 2582349
Email: mq@iitg.ernet.in

Certificate

Certified that the work described in this thesis entitled "**Efficient Heterojunction Strategies in Multinary Sulfide Based Semiconductors for Enhanced Photocatalytic Performance**" by Miss Gaurangi Gogoi, Department of Chemistry, Indian Institute of Technology Guwahati has been carried out under my supervision and has not been submitted elsewhere for a degree or diploma.

Guwahati
April 2019

Mohammad Qureshi
(Thesis supervisor)
Department of Chemistry
IIT Guwahati
Guwahati – 781039, Assam
India

ACKNOWLEDGEMENT

Standing here at the closing end of the long and memorable journey of PhD, I realise that the support, inspiration, motivation and influence of many people throughout this journey have helped me pursue this dream into reality. I take this opportunity to thank all those wonderful souls who have helped me travel this experience at ease.

Firstly, with deepest respect and gratitude, I would acknowledge my supervisor, Prof. Mohammad Qureshi for providing me the privilege to work under his guidance. He had been a constant source of inspiration and motivation and his apt knowledge, keen observations and technical discussions have always helped me pursue my work. I further acknowledge him for providing the freedom of thought in designing and solving the scientific problems and lending his help and guidance whenever needed. Apart from the technical supervision, his attitude to life and his personality traits have indeed influenced and helped me a lot to develop into a better version of me.

I would also like to extend my gratitude to the doctoral committee members, Prof G. Krishnamoorthy, Prof. Aditya Narayan Panda and Dr. Bhubaneshwar Mandal for their constructive comments and time to time evaluation of my research work which helped to mould it to a better shape.

Spending most of the time in the laboratory would not have been possible without a healthy and friendly environment in the lab. I would sincerely thank my past lab members, Dipankar da, Tridip da, Anindya da, my friends–Shaad and Avishek, my juniors– Tushar, Adit, Suhaib, Moite, Manoj, Sourav and the interns for staying as a family, sharing light moments together and creating a pleasant atmosphere in the lab. I would specially like to thank Anindya da, for training me in handling equipments, experiments and guidance in many other technicalities. I am thankful to Sonia Ma'am for her encouragement and help, especially in the first work of my thesis.

I thank my collaborators, Prof Shane Ardo, Sam Keene (University of California, Irvine), Dr. N. Vinothkumar, Dr. Mahuya De, Devipriya Gogoi and Dr. Nageswara Rao Peela (Department of Chemical Enginering, IIT Guwahati) for their constructive discussions, comments and inputs in my research work.

I sincerely acknowledge IIT Guwahati for providing all the facilities necessary for smooth conduction of my research work. I am thankful to SAIF, NEHU for TEM facility and CSIR-NEIST for XPS analysis, CIF, IIT Guwahati for instrumental facilities, Department of Physics, IIT Guwahati for PXRD analysis. I also thank the scientific officers and operators of Department of

Chemistry, Physics and CIF, IIT Guwahati for helping me in analysis and characterisation. I am indebted to Ministry of Human Resource and Development (MHRD), India for the financial assistance.

Apart from the research activities, I have spent quite a delightful and memorable time in the campus and I owe it all to the wonderful friends I have met. I am thankful to my friends– Mahmuda, Dhriti, Anju, Ahalya, Aparajita, Sumana, Soumita, Jyoti, Titli, Anamika, Rashmi, Nilotpal, Amlan, Adil, Srinivasan, Subhra, Ravindra, Balram, all my AOL friends, for the lively time and unforgettable bond of friendship shared, seniors and juniors, my hostel mates – specially Nimisha, Prerona and Tripti for the relaxing talks and the homely environment after a tiring day at work, Joy, Pankaj and Alice for the jovial time spent with you.

I am thankful to all my loving family members for their support and encouragement, specially my uncle and aunt staying at Guwahati, who have always provided me a second home.

Lastly, I am extremely grateful and indebted to Maa (Manju Gogoi), Deuta (Umesh Chandra Gogoi) and Vaity (Jumon) for their immense emotional support, motivation, confidence, tremendous sacrifices and constant shower of love and blessings on me. I couldn't have completed this journey without you beside me.

Gaurangi

Dedicated to

Maa

&

Deuta

		Page
	Synopsis	i
CHAPTER 1	**Introduction**	1
1.1	GLOBAL ENERGY PERSPECTIVE	3
1.2	PHOTO–DRIVEN WATER SPLITTING	4
1.2.1	Particulate photocatalytic systems or powdered photocatalysis	6
1.2.2	Photoelectrochemical (PEC) Water Splitting	7
1.3	USE OF SACRIFICIAL REAGENTS	9
1.4	PHOTOCATALYST REQUIREMENTS AND STRATEGIES TO DEVELOP EFFICIENT PHOTOCATALYSTS	11
1.4.1	Band Gap Engineering	11
1.4.2	Micro/nano Engineering	12
1.4.3	Co–catalyst Engineering	13
1.4.4	Interface Engineering	14
1.5	SELECTION OF SULFIDE SEMICONDUCTORS	16
1.6	PHOTOCATALYTIC DYE DEGRADATION	19
1.7	SCOPE OF THIS THESIS WORK	21
1.8	REFERENCES	22
CHAPTER 2	**Experimental Section**	29
2.1	INTRODUCTION	31
2.2	MATERIALS AND CHEMICALS USED	31
2.3	CHARACTERISATION TECHNIQUES	31
2.4	EXPERIMENTAL PROCEDURES FOR PHOTOCATALYTIC ACTIVITY	33
2.4.1	Photocatalytic Hydrogen Production	33
2.4.2	Reusability of the Photocatalysts	34

2.4.3	Photocatalytic Rhodamine B Dye Degradation	35
2.4.4	Fabrication of Photoelectrode	35
2.4.5	Photoelectrochemical Water Oxidation	36
2.5	PHOTOCATALYTIC ACTIVITY EVALUATION	37
2.5.1	Apparent Quantum Yield	37
2.5.2	Electrochemical Impedance (EIS) Spectra	38
2.5.3	Faradaic Efficiency	41
2.6	REFERENCES	42
CHAPTER 3	**Quaternary Semiconductor Cu_2ZnSnS_4 Loaded With MoS_2 as a Co–catalyst for Enhanced Photocatalytic Activity**	43
3.1	INTRODUCTION	45
3.2	EXPERIMENTAL SECTION	46
3.2.1	Preparation of CZTS	46
3.2.2	Preparation of MoS_2	46
3.2.3	Preparation of CZTS–MoS_2	47
3.3	RESULTS AND DISCUSSION	47
3.3.1	Powder X-ray Diffraction (PXRD) Patterns	47
3.3.2	Field-Emission Scanning Electron Microscopy	48
3.3.3	Transmission Electron Microscopy	49
3.3.4	Ultraviolet-Visible Diffuse Reflectance Spectra and Band Gap Calculation	50
3.3.5	Raman Spectral Analysis	51
3.3.6	BET Surface Area Analysis	52
3.3.7	Steady-State Photoluminescence Spectra	53
3.3.8	Photocatalytic Hydrogen Production	53
3.3.9	Reusability of CZTS–MoS_2	55

3.3.10	Photocatalytic Dye Degradation Analysis	56
3.3.11	Photocatalytic Dye Degradation Mechanism	57
3.4	CONCLUSION	60
3.5	REFERENCES	60
CHAPTER 4	**Hybrid of g-C_3N_4 AND MoS_2 Integrated onto $Cd_{0.5}Zn_{0.5}S$: Rational Design with Efficient Charge Transfer for Enhanced Photocatalytic Activity**	63
4.1	INTRODUCTION	65
4.2	EXPERIMENTAL SECTION	66
4.2.1	Preparation of $Cd_{0.5}Zn_{0.5}S$	66
4.2.2	Preparation of MoS_2	67
4.2.3	Preparation of g-C_3N_4	67
4.2.4	Preparation of $Cd_{0.5}Zn_{0.5}S$–g-C_3N_4 and $Cd_{0.5}Zn_{0.5}S$–g-C_3N_4–MoS_2 Composites	67
4.3	RESULTS AND DISCUSSION	67
4.3.1	Powder X–ray Diffraction (PXRD) Patterns	67
4.3.2	X-Ray Photoelectron Spectroscopy (XPS) Spectra	69
4.3.3	Ultraviolet-Visible Diffuse Reflectance Spectroscopy	72
4.3.4	Field-Emission Scanning Electron Microscopy	73
4.3.5	Transmission Electron Microscopy	76
4.3.6	Steady-State Photoluminescence Study	78
4.3.7	Time-Resolved Photoluminescence Study	79
4.3.8	Raman Spectral Analysis	81
4.3.9	BET Surface Area Analysis	82
4.3.10	Photocatalytic Hydrogen Production Analysis	82
4.3.11	Photocatalytic Dye Degradation Analysis	87

4.3.12	Determination of Band Structure and Charge Transfer Mechanism	90
4.4	CONCLUSION	93
4.5	REFERENCES	94
CHAPTER 5	**A Direct Z-scheme Strategy Utilizing $ZnIn_2S_4$ and Hierarchical VS_2 Microflowers for Superior Photoelectrochemical Water Oxidation**	99
5.1	INTRODUCTION	101
5.2	EXPERIMENTAL SECTION	102
5.2.1	Preparation of $ZnIn_2S_4$	102
5.2.2	Preparation of VS_2	102
5.2.3	Preparation of $ZnIn_2S_4$–VS_2	102
5.3	RESULTS AND DISCUSSION	103
5.3.1	Powder X-ray Diffraction (PXRD) Patterns	103
5.3.2	Material Morphology and Elemental Analysis	104
5.3.3	Ultraviolet-Visible Diffuse Reflectance Spectra and Band Gap Calculation	106
5.3.4	Fourier Transformed Infra-Red (FT-IR) and Raman Spectra Analysis	107
5.3.5	X-ray Photoelectron Spectroscopy (XPS) Spectra	108
5.3.6	Determination of Charge Transfer Mechanism	111
5.3.7	Steady State and Time Resolved Photoluminescence	112
5.3.8	Electrochemical Characterisations for Water Oxidation	114
5.4	CONCLUSION	119
5.5	REFERENCES	120

CHAPTER 6 Thesis Overview and Future Scope 125

List of Publications and Conferences Attended 131

Thesis Title:	**Efficient Heterojunction Strategies in Multinary Sulfide Based Semiconductors for Enhanced Photocatalytic Performance**
Name of the Candidate:	Gaurangi Gogoi
Registration Number:	136122031
Thesis Supervisor:	Prof. Mohammad Qureshi
Department:	Chemistry
Institute:	Indian Institute of Technology Guwahati, Assam-781039

Chapter 1: Introduction

This chapter discusses the need for renewable and environmentally friendly alternative energy resources owing to the rising drift in energy consumption. Hydrogen, a clean, and energy efficient fuel is considered as the most ideal alternative fuel to meet the future energy demand. In order to deal with this problem of the use of almost exhaustible fossil fuel and production of CO_2, there has been a continuous endeavor for hydrogen production from earth abundant resource – water, utilizing the most abundant energy source – solar energy. Among the several ways for solar hydrogen production, photochemical water splitting fascinates much attention because it is a simple, inexpensive and highly efficient process. This chapter discusses the basic concepts and mechanism of photocatalytic and photoelectrochemical water splitting and the criteria for selection of semiconductor materials to be used in photocatalysis. As compared to widely used oxide semiconductor materials, sulfide semiconductors possess relatively high conduction band positions suitable for water reduction and better sunlight responses than oxides, due to the higher valence band positions composed of S 3p orbitals. However, sulfide semiconductor materials suffer from the drawback of faster photogenerated charge recombination owing to the narrow band gap and the problem of photo bleaching. To overcome this drawback and for efficient charge extraction, several strategies have been continuously adopted. This chapter includes a survey of different strategies developed to enhance the catalytic activity by a photocatalytic semiconductor material by efficient charge extraction. It also includes the rationale behind the adopted strategies of heterojunction formation for enhancement of photocatalytic efficiency of the bare sulfides

semiconductors. Recent advancement in the rational design of different heterojunction systems including Z-scheme as an efficient photocatalytic system is outlined in this chapter.

Chapter 2: Experimental Methods and Materials Characterizations

This chapter describes the comprehensive route adopted for the synthesis of the studied semiconductor materials. In order to characterise the compounds, various instrumentation techniques are adopted, which are discussed in details in this chapter. The experimental details for photocatalytic activity measurement like hydrogen generation rate, rhodamine B dye degradation, photoanode fabrication for photoelectrochemical water oxidation etc. are described. The experimental setup utilised for analysing the photocatalytic and photoelectrochemical properties of the synthesised materials are described. Finally, details of the various parameters utilised for assessing the photocatalytic property like apparent quantum yield, rate of hydrogen production etc. and photoelectrochemical water oxidation properties of the synthesised materials like current-voltage characteristics, electrochemical impedance spectroscopy (EIS) measurements are discussed in details in this chapter.

Chapter 3: Quaternary Semiconductor Cu_2ZnSnS_4 Loaded with MoS_2 as Co-catalyst for Enhanced Photocatalytic Activity (*RSC Adv.*, 2015, **5,** 40475)

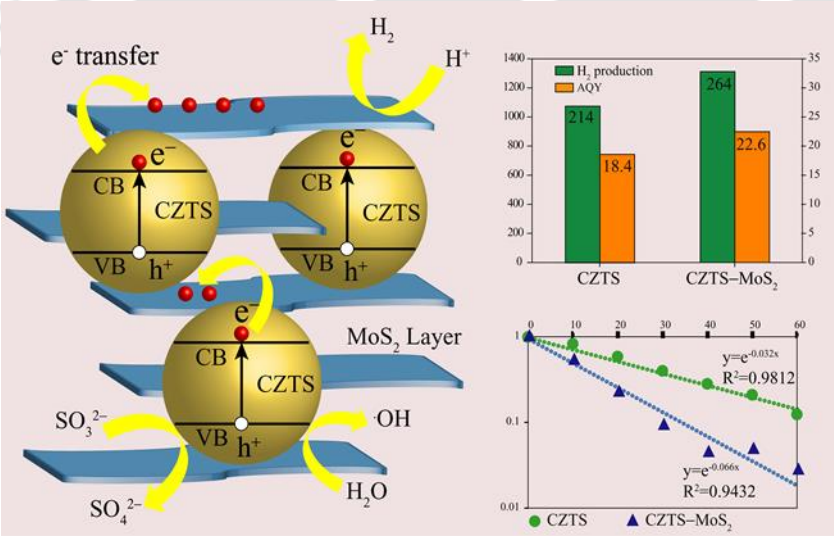

***Scheme 1**: Graphical representation of the probable charge transfer pathways in the composite CZTS-MoS_2 along with the comparison of photocatalytic efficiency of hydrogen production and Rhodamine B dye degradation for CZTS and CZTS-MoS_2*

Quaternary Cu_2ZnSnS_4 (CZTS) and its composite with a cocatalyst viz. MoS_2 (CZTS-MoS_2) are prepared by a facile hydrothermal method. The as synthesised compounds are characterised by several characterisation techniques like powder X-ray diffraction, Field Emission Scanning Electron Microscopy, Transmission Electron Microscopy etc. The materials are studied for their photocatalytic activity as shown in Figure 1. CZTS-MoS_2 composite shows a greater photo-catalytic activity with the H_2 production rate of 264 µmol/0.2g/h in comparison to bare CZTS (214 µmol/0.2g/h). The calculated Apparent Quantum Yield (AQY) of CZTS-MoS_2 is 22.67% which is about 1.23 times higher than that of CZTS i.e. 18.42%. It is also observed that RhodamineB (RhB) is degraded much faster by CZTS-MoS_2 than bare CZTS. ~ 97% degradation of RhB is achieved in case of CZTS-MoS_2 in about 40 minutes whereas it was only ~70% for bare CZTS.

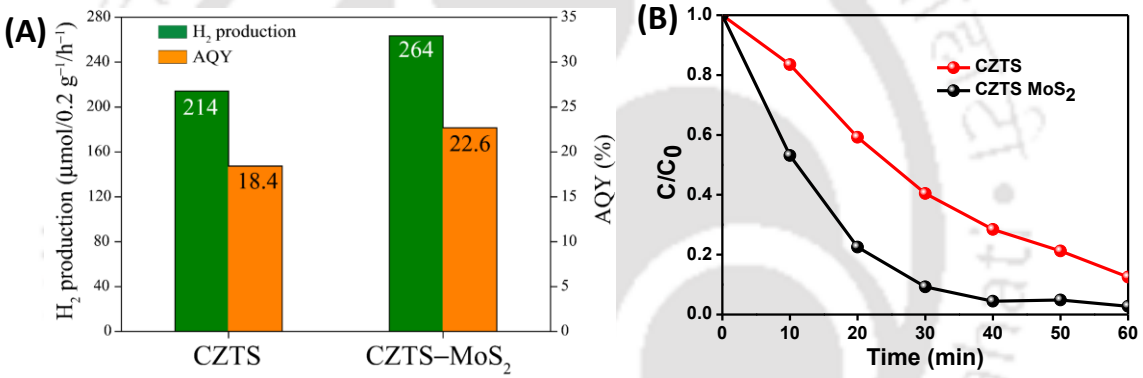

***Figure 1**: (A) Amount of H_2 generated from CZTS and CZTS-MoS_2 under visible light irradiation and their respective AQY (%) values, (B) C/C_0 versus irradiation time curves of photo-degradation of RhB by CZTS and CZTS-MoS_2.*

The higher photo-catalytic activity is attributed to more active sites in CZTS-MoS_2 as well as higher charge separation. A schematic of the band diagram showing energy alignments of CZTS-MoS_2 which facilitates an efficient transfer of electrons is shown in Figure 2. In order to study the mechanism of dye degradation, various scavenger tests were performed using Fe^{2+} salt, N_2 purging and EDTA as $^{\bullet}OH$, superoxide radical anion ($O_2^{\bullet-}$) and hole scavenger, respectively. From the kinetic data, hydroxyl radical could be the determining species in controlling the kinetics of the dye degradation.

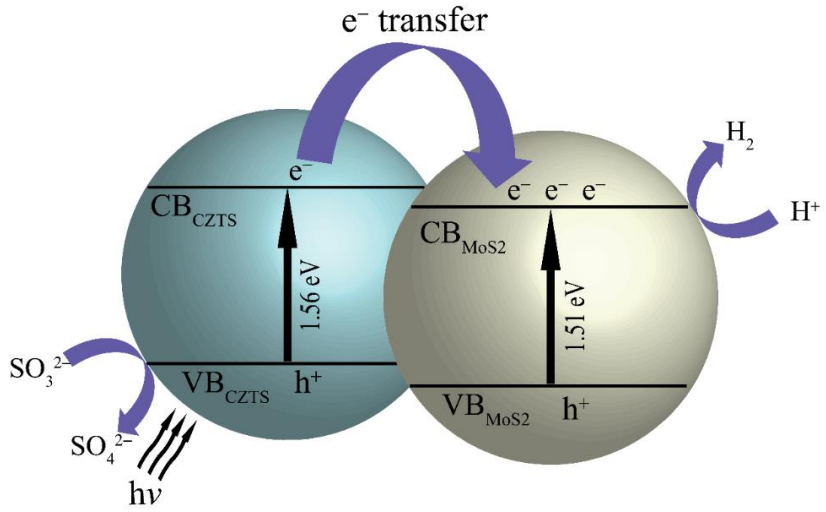

***Figure 2**: Schematic representation of probable electron transfer pathways in CZTS-MoS_2*

Chapter 4: Hybrid of g-C_3N_4 and MoS_2 Integrated onto $Cd_{0.5}Zn_{0.5}S$: Rational Design with Efficient Charge Transfer for Enhanced Photocatalytic Activity (*ACS Sustainable Chem. Eng.*, 2018, **6**, 6718)

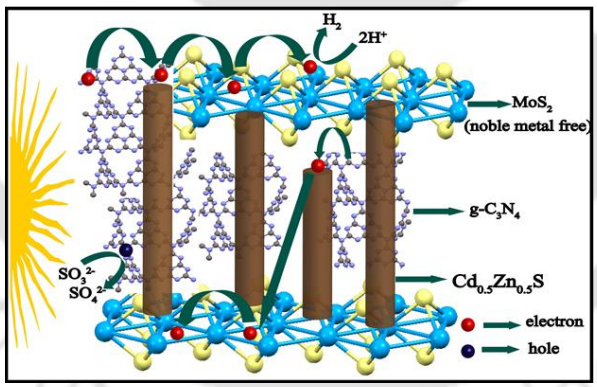

***Scheme 2**: Graphical representation of the probable charge transfer pathways in the composite $Cd_{0.5}Zn_{0.5}S$-g-C_3N_4-MoS_2*

In this chapter, a rational design of hierarchical nano-composites is developed for efficient energy harvesting. A noble-metal-free ternary hierarchical composite, $Cd_{0.5}Zn_{0.5}S$-g-C_3N_4-MoS_2, has been developed. Materials are chosen based on their relative band-edge alignments and they are studied as a composite for photocatalytic properties. In the composite, $Cd_{0.5}Zn_{0.5}S$ acts as electron sink for the photoinduced carriers transferred from g-C_3N_4 and thus profusely help in the prevention of charge recombination by separating the photogenerated electron- hole pair and lead to an enhanced photo activity. Furthermore, the

conjugated MoS_2 can act as an excellent supporting matrix for electron transport and can play an important role for the enhancement of photocatalytic activity. Thus the synergistic integration of $Cd_{0.5}Zn_{0.5}S$-g-C_3N_4 with MoS_2 can serve as a better catalytic system. The charge transfer mechanism in the composite is proved by the several experimental techniques like X-ray photoelectron spectroscopy, steady and time resolved photoluminescence. A schematic of the proposed charge transfer pathway in the composite is shown in Figure 3.

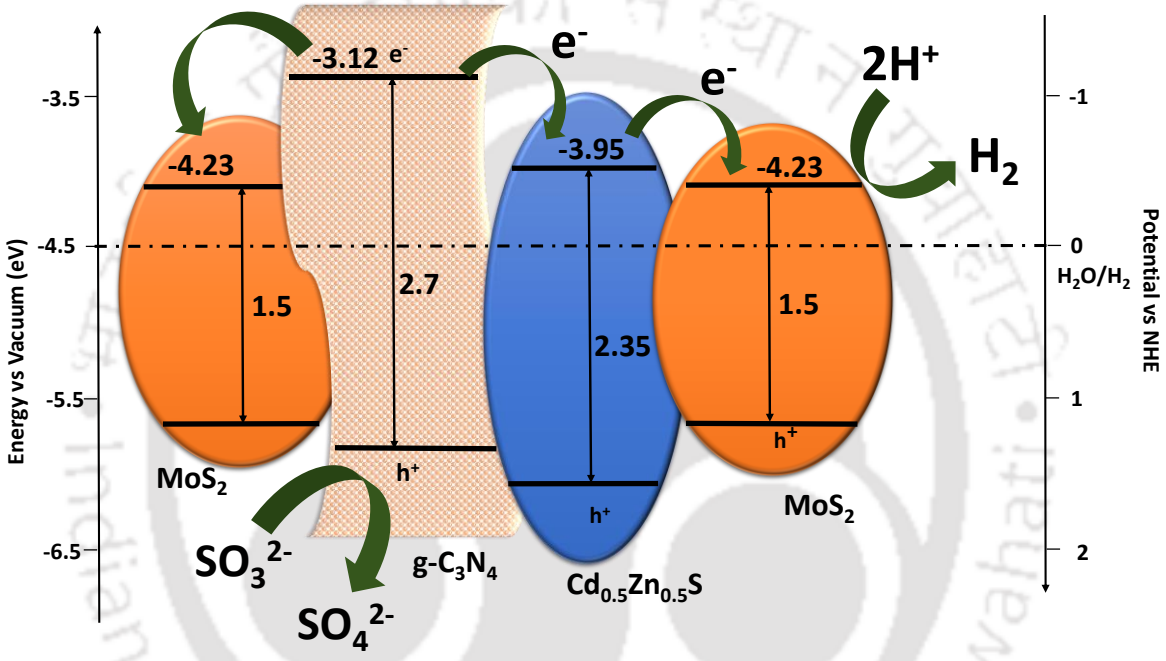

***Figure 3**: Schematic representation of electron transfer in $Cd_{0.5}Zn_{0.5}S$-g-C_3N_4-MoS_2.*

The photocatalytic activity was evaluated by measuring the rate of photo-driven H_2 evolution with concomitant degradation of organic pollutants, such as Rhodamine B. Optimization of the loading of g-C_3N_4 and MoS_2 onto $Cd_{0.5}Zn_{0.5}S$ results in an enhanced yield of hydrogen evolution by ~120% ($Cd_{0.5}Zn_{0.5}S$-g-C_3N_4) and ~197% ($Cd_{0.5}Zn_{0.5}S$-g-C_3N_4-MoS_2) compared to bare $Cd_{0.5}Zn_{0.5}S$. The ternary hybrid, $Cd_{0.5}Zn_{0.5}S$-g-C_3N_4-MoS_2 resulted in an apparent quantum yield (AQY) of 38 % at 420 nm. The significant improvement in photocatalytic performance in the composite can be attributed to enhanced interfacial charge transfer of electrons from g-C_3N_4 to $Cd_{0.5}Zn_{0.5}S$ and MoS_2. The results of photocatalytic hydrogen production are shown in Figure 4.

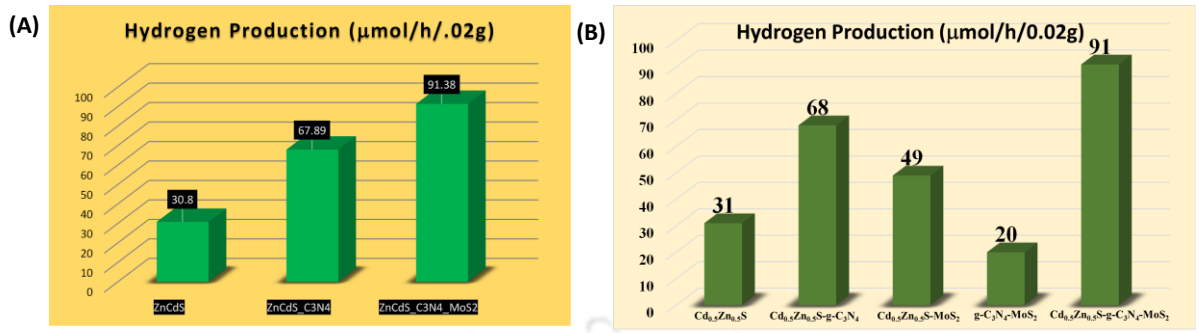

***Figure 4**: (A) Comparison of photocatalytic activity of $Cd_{0.5}Zn_{0.5}S$-g-C_3N_4-MoS_2, $Cd_{0.5}Zn_{0.5}S$-g-C_3N_4 and $Cd_{0.5}Zn_{0.5}S$. (B) Comparison of photocatalytic activity of $Cd_{0.5}Zn_{0.5}S$-MoS_2, g-C_3N_4-MoS_2 along with $Cd_{0.5}Zn_{0.5}S$-g-C_3N_4-MoS_2, $Cd_{0.5}Zn_{0.5}S$-g-C_3N_4 and $Cd_{0.5}Zn_{0.5}S$.*

The Rhodamine B dye degradation efficiencies of $Cd_{0.5}Zn_{0.5}S$, $Cd_{0.5}Zn_{0.5}S$-g-C_3N_4 and $Cd_{0.5}Zn_{0.5}S$-g-C_3N_4-MoS_2 are 50.1%, 95.6% and 96% respectively. C/C_0 versus time (min) plot of all the composites are shown in Figure 5.

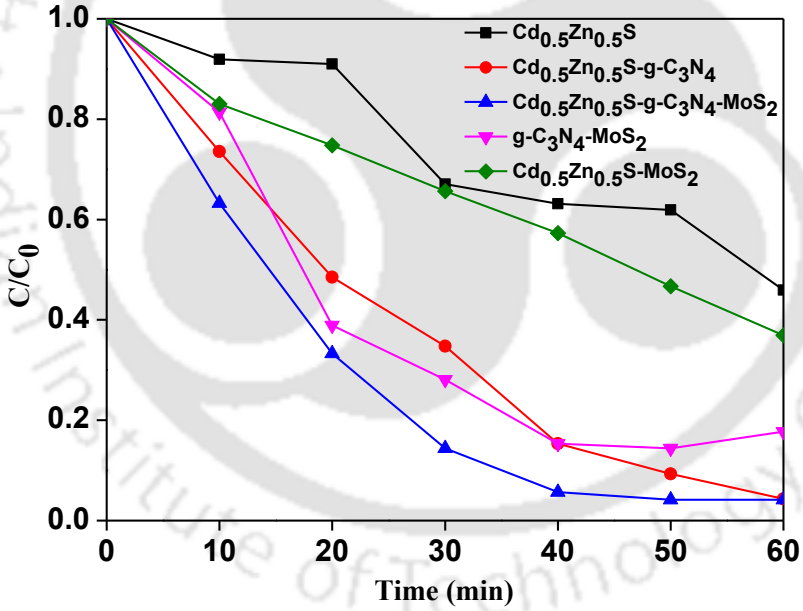

***Figure 5**: C/C_0 versus time (min) plot of $Cd_{0.5}Zn_{0.5}S$, $Cd_{0.5}Zn_{0.5}S$-g-C_3N_4, $Cd_{0.5}Zn_{0.5}S$-g-C_3N_4- MoS_2, g-C_3N_4-MoS_2 and $Cd_{0.5}Zn_{0.5}S$-g-C_3N_4.*

Chapter 5: A Direct Z-scheme Strategy Utilizing $ZnIn_2S_4$ and Hierarchical VS_2 Microflowers for Superior Photoelectrochemical Water Oxidation (*Manuscript under Communication*)

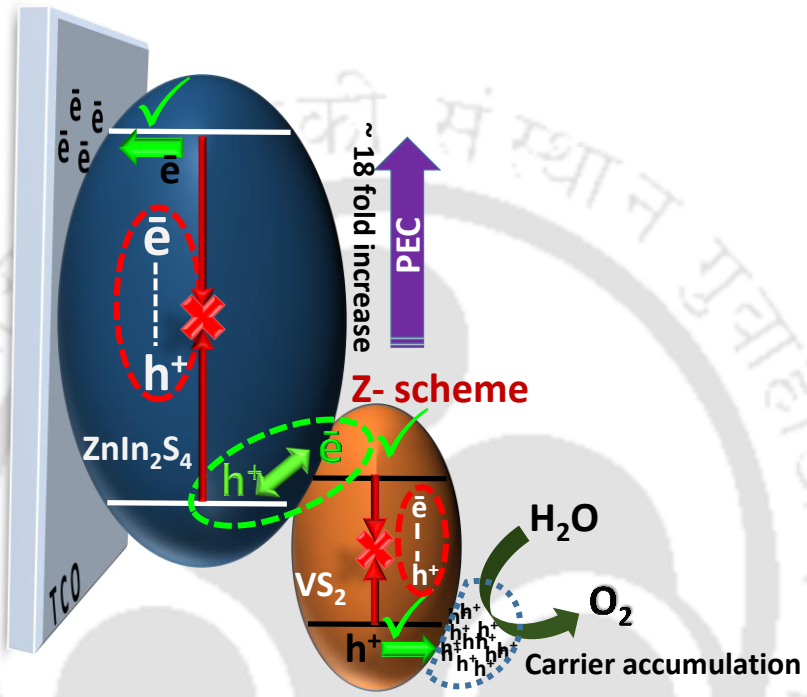

***Scheme 3**: Graphical representation of the probable charge transfer pathways in the composite $ZnIn_2S_4$-VS_2*

In this chapter, for the first time, we have developed a strategy for a widely studied I-III_2-VI_4 photocatalyst, $ZnIn_2S_4$, using hierarchical VS_2 microflowers for a direct Z-scheme pathway, without an electron mediator, for efficient charge separation. The materials are synthesised by hydrothermal method and the composite synthesised by sonication of the components in definite weight percentage. Figure 6 shows the morphological features of the composite as well as the individual components.

***Figure 6**: Field emission scanning electron microscopy images of (A) $ZnIn_2S_4$, (B) VS_2 and (C) $ZnIn_2S_4$-VS_2. Anticipated VS_2 in $ZnIn_2S_4$-VS_2 is encircled in red dotted circles in (C).*

The charge transfer dynamics is established to be following a direct Z-scheme pathway in the composite which results in reduced charge recombination and greater accumulation of surface charges. Further owing to the advantage of Z-scheme the sites for oxidation and reduction are at the more positive and negative sites respectively. The experimental findings establish successful chemical interaction of the components through sulfur edge. The advantage of better charge extraction in Z-scheme is observed from an impressive ~ 18-fold increase in the photocurrent value observed in $ZnIn_2S_4$-VS_2 over its bare counterpart. A thorough investigation of dynamics of charge transfer in the composite is carried out by electrochemical impedance spectroscopy (EIS) experiments. Furthermore, slow kinetics of surface reaction in the composite $ZnIn_2S_4$-VS_2 is correlated to the increased surface charge capacitance. This feature of the composite facilitates partial storage of the photo generated charge carriers (e^- /h^+) under illumination and dark current conditions, thus storing and utilizing the solar energy. The current voltage characteristics along with the Nyquist plot is shown in Figure 7.

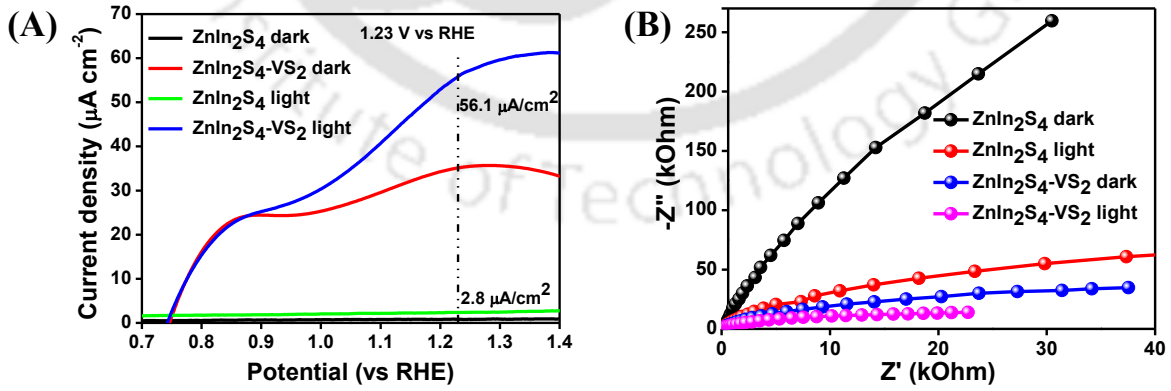

***Figure 7**: (A) J-V curves and (B) Nyquist plots of $ZnIn_2S_4$ and $ZnIn_2S_4$-VS_2 under dark and illumination.*

Chapter 6: Thesis Overview and Future Scope

This chapter summarizes the overall work carried out by developing different multinary sulfide based semiconductor systems for utilization as efficient photocatalysts for water reduction or dye degradation. It also provides some directions for future study based on the current findings.

Chapter 1

Introduction

This chapter describes the basics of powdered photocatalysis, photoelectrochemical water splitting and dye degradation. It briefly describes the different strategies generally adopted in order to increase the efficiency of semiconductor photocatalysts. This chapter gives an insight behind the rational of selection of sulphide photocatalytic materials in the thesis. Finally, it presents a brief literature survey of some sulphide based materials used in photocatalytic and photoelectrochemical system.

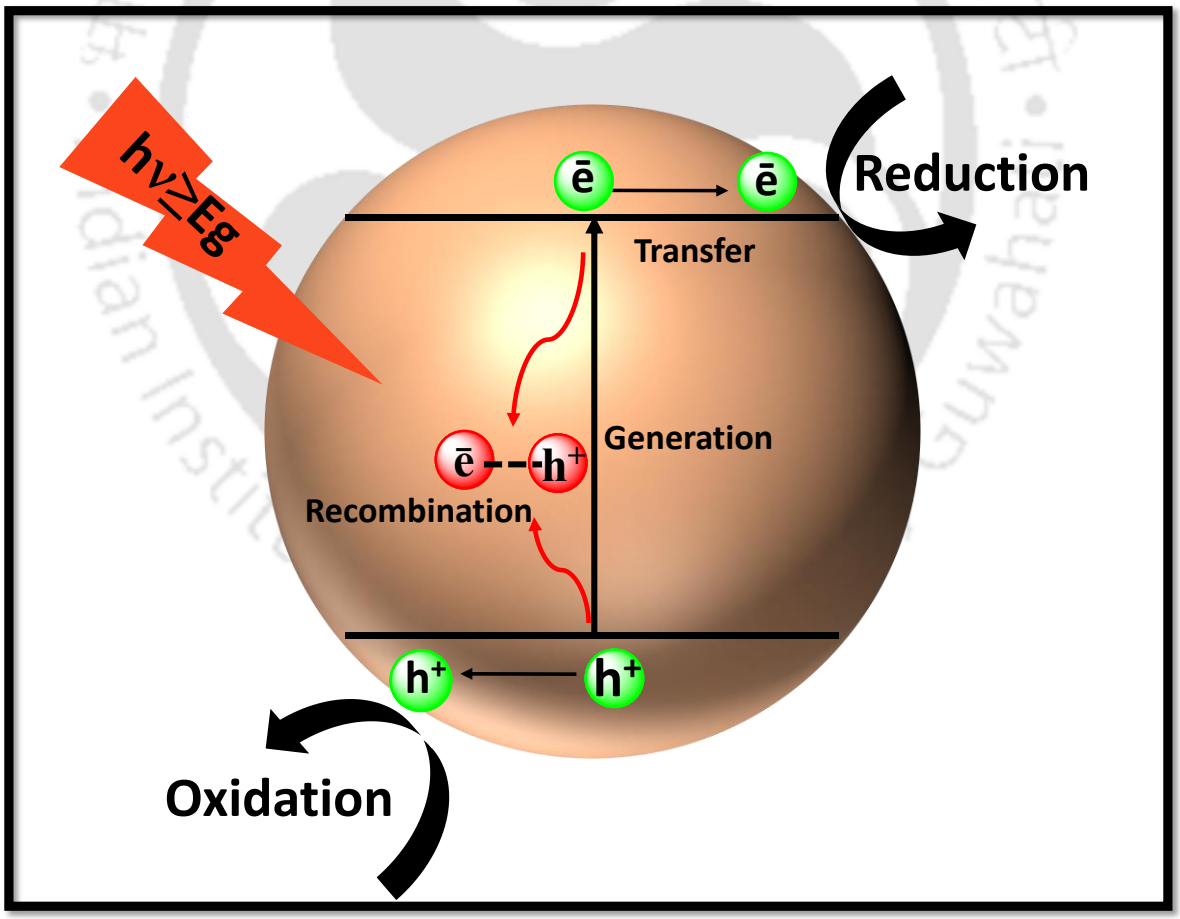

1.1 GLOBAL ENERGY PERSPECTIVE

The socio–economic development of the world population is most importantly dependent on the access to affordable energy resources. Energy consumption patterns have changed significantly over time.[1] The world energy consumption was 575 quadrillion British thermal units (Btu) in 2015 and is projected to rise to 663 quadrillion Btu by 2030.[2] Over 80% of the current energy usage is from fossil fuels consisting of liquid petroleum, coal, and natural gas.[3,4] The high rate of consumption of this non–renewable energy source leads to its fast depletion, which necessitates a transition to an alternative source of energy.

In view of increasing greenhouse gas emissions and exploitation of non–renewable energy resources, utilization of sustainable and renewable energy sources, such as solar, hydro, wind or biomass is highly desirable. The projected high energy demand could be easily fulfilled by an abundantly available energy source, solar energy, as the energy from sunlight falling on the earth in 1 h (4.3×10^{20} J) is more than the total energy consumed annually.[3] Energy harvested from solar energy is estimated to be the largest by 2050, surpassing other major sources like fossil fuels, wind, hydro and nuclear.[5] However, the sporadic availability of solar energy during the course of the day as well as season, makes it challenging to maintain the continuous extraction of energy. Thus, for the fulfilment of a significant portion of our total power by solar energy, large scale storage solutions have to be implemented. An attractive and feasible way of energy storage to terawatt scale is by capturing energy in chemical bonds of a renewable fuel — hydrogen.[3] Hydrogen, one of the most promising energy carriers due to its very high energy content per unit mass (142 kJ/g), which is much higher compared to other chemical fuels (e.g. liquid hydrocarbons, with an energy content of 47 kJ/g), gives away only heat and water when burnt.[6]

A major portion of the hydrogen consumed worldwide is derived from steam reforming of natural gas (around 48%), while other contributions are mainly based on partial oxidation of refinery oil (about 30%), gasification of coal (18%) and water electrolysis (4%).[7] The pathways generating almost 96% of the total hydrogen produced, involves fossil fuels (i.e. natural gas, refinery oil and coal), which releases harmful carbon dioxide into the atmosphere. However, water electrolysis which involves splitting of water into its components, hydrogen (H_2) and oxygen (O_2) is a carbon–free method and is thus highly desirable.

Different methods to generate H_2 can be categorised as: (i) thermal, (ii) electrolytic and (iii) photolytic processes. Thermal processes utilise the energy associated with chemical reactions to obtain H_2. H_2 generation by steam reforming of natural gas and coal gasification occurs by thermal processes. Electrolytic process uses electricity for splitting water into H_2 and O_2 by an electrochemical approach. Photolytic process utilises ample source of energy — sunlight, to split abundantly available water into its constituents, H_2 and O_2 by photocatalytic, photo–electrochemical or photo–biological approaches.[8]

1.2 PHOTO–DRIVEN WATER SPLITTING

Semiconductor materials are often selected as artificial photocatalysts to carry out water splitting as they can capture solar photons for excitation of an electron from its valence band to conduction band and generates the potential required for driving chemical reactions at their surfaces.[9] Heterogeneous photocatalytic water splitting on a semiconductor material proceeds as shown in **Figure 1.1**. Semiconductor materials consists of a band structure with a conduction band and a valence band separated by a band gap. The first step in the solar driven water splitting on a semiconductor particle involves **(i) absorption of photons** by semiconductor materials to form electron–hole pairs. When light of energy greater than or equal to the band gap of the semiconductor is incident on it, electrons (e^-) and holes (h^+) are generated in the conduction band and valence band, respectively. Important criteria to be fulfilled by the semiconductor material for overall water splitting is the band gap of the semiconductor and the levels of valence band and conduction band. The bottom level of the conduction band has to be more negative than the redox potential of H^+/H_2 (0 V vs. NHE) for reduction of water to H_2, while the top level of the valence band of the semiconductor has to be more positive than the redox potential of O_2/H_2O (1.23 V vs. NHE). Therefore, theoretically the minimum band gap of a semiconductor for overall water splitting is 1.23 eV that corresponds to light of wavelength of about 1000 nm. The second step as shown in **Figure 1.1** involves **(ii) charge separation and migration** of photogenerated charge carriers. This step is limited by a detrimental process of charge recombination. This efficient separation of charge is influenced by the crystal structure, crystallinity and particle size of the semiconductor material. Defects present in the material act as trap sites or recombination centres for the photogenerated electrons and holes. The recombination probability decreases for smaller particle size as the photogenerated charge carriers can easily migrate to the surface

reaction sites. The final step involves the **(iii) chemical reactions** at the surface reaction sites. The photogenerated electrons and holes that avoid recombination and migrate to the surface reaction sites of the semiconductor photocatalyst, can reduce and oxidize water molecules adsorbed at the semiconductor to H_2 and O_2 respectively. This step is determined by the number of active sites and the surface area of the semiconductor material.[10]

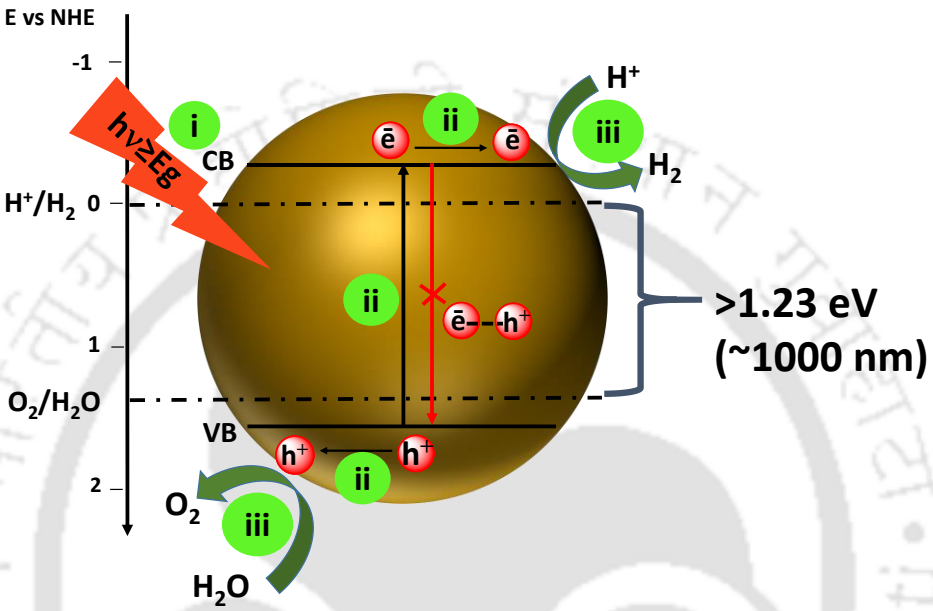

Figure 1.1: Graphical representation of the various steps involved in photo–driven water splitting on a semiconductor particle. The red arrow represents the unfavourable process of charge recombination. Adopted from Ref. 71.

Photocatalytic water decomposition on a semiconductor, though conceptually seems simple, but involves a high positive Gibbs free energy change of ΔG^0 = +237 kJ/mol which corresponds to ΔE_0 = 1.23 V according to the Nernst equation. Photo–driven water decomposition is an imitation of photosynthesis where water is converted into H_2 and O_2 using inorganic semiconductors in the presence of sunlight as the following reaction (**Equation (1.1)**): [11]

$$H_2O \longrightarrow H_2 + \frac{1}{2} O_2 \; ; \; \Delta G° = +237 \text{ kJ/mol} \qquad \textbf{(1.1)}$$

The overall water splitting process can be expressed as (**Equation (1.2)–Equation (1.5)**):

$$\text{Photocatalyst} + \text{light} \longrightarrow h^+_{VB} + e^-_{CB} \qquad \textbf{(1.2)}$$

$$\text{Oxidation: } H_2O + 2h^+_{VB} \longrightarrow 2H^+ + \frac{1}{2}O_2 \qquad \textbf{(1.3)}$$

$$\text{Reduction: } 2H^+ + 2e^-_{CB} \longrightarrow H_2 \qquad \textbf{(1.4)}$$

$$\text{Overall reaction: } H_2O \longrightarrow H_2 + \frac{1}{2}O_2 \qquad \textbf{(1.5)}$$

Photochemical water splitting can be carried out in two different types of configurations following identical basic principle:

(i) Particulate photocatalytic systems or powdered photocatalysis

(i) Photoelectrochemical cells

1.2.1 Particulate photocatalytic systems or powdered photocatalysis

In particulate photocatalytic water splitting, semiconductor photocatalysts are suspended in the form of powder or particles in aqueous solution and works on the principle as discussed in **Section 1.2**. The particles of powdered catalysts have dimensions in the range of nanoscale, which leads to much increase in the total surface area of the photocatalyst and thus increases the number of available reaction sites.[12] This photocatalytic system has the advantage of being simple and cost effective.[11] However, in smaller particles, the photogenerated electrons and holes are spatially confined within close vicinity which makes electron–hole pairs more likely to recombine without reacting. Another disadvantage of a powdered photocatalytic system is that the reaction products produced in close proximity makes the back reaction of the products (i.e. H_2 and O_2) more likely. The factors of recombination of photogenerated charge carriers and the back reaction of the reaction products leads to a loss of efficiency in such systems.[13, 14] Moreover, the problem of separation of the fine suspended particles after reaction, results in high operation costs. These disadvantages are less likely in the configuration of photoelectrochemical water splitting as discussed in the next section.

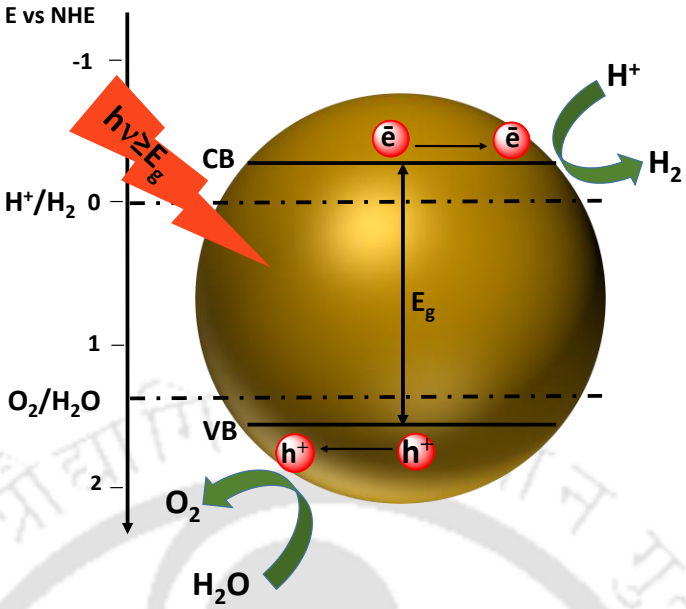

Figure 1.2: Schematic representation of water splitting on a semiconductor photocatalyst. Adopted from Ref. 71.

1.2.2 Photoelectrochemical (PEC) Water Splitting

Photoelectrochemical water splitting was first demonstrated by Honda and Fujishima in 1972, the basic cell of which consisted of an n–type rutile TiO_2 photoanode and platinum photocathode.[15] Basically, in a PEC device, photon energy is converted into electrochemical energy, in order to split water and convert into chemical energy in the form of H_2 and O_2.[16] The fundamental setup in a PEC device comprises of a working electrode with a photo absorber semiconductor material supported on a conductive substrate (usually an n–type semiconductor as a photoanode and p–type material as photocathode), a counter electrode (Pt) and a reference electrode (e.g. Ag/AgCl).[17]

When the semiconductor electrode is immersed in an electrolyte solution, the Fermi level of the semiconductor must equilibrate with the electrochemical potential of the electrolyte for which there is a flow of charge from one phase to the other, across the semiconductor–liquid junction (SCLJ), resulting in a "band bending" within the semiconductor.[18] The region within the semiconductor, near the junction, across which the charge flows during this equilibration process is termed as the space charge region or depletion layer, as the layer is depleted of the majority charge carriers.[19] An important

characteristic of a semiconductor in PEC water splitting, is the generation of built–in electric field in the space charge region which results in band bending near the interface. Upon illumination on the semiconductor, non–equilibrium population of electrons and holes are generated. The electrochemical potential of electrons and holes under non-equilibrium (i.e. illuminated) conditions is expressed as quasi–Fermi level (E_{fn}: quasi–Fermi level of electrons, E_{fp}: quasi–Fermi level of holes). The gradient in the quasi–Fermi level results in an electric field near the semiconductor surface. The voltage generated by the built–in electric field of the semiconductor is termed the 'photovoltage' (V_{ph}) or 'open–circuit voltage' (V_{OC}).[18] The photoinduced charges in the photoelectrodes are separated and transferred at a timescale of picoseconds by applying electrochemical potentials assisted by the built–in electric field (E_{in}) in the depletion region.[20, 21]

Incoming photons of suitable energy ($h\nu$) generate electrons (e^-) and holes (h^+) which are separated and travel through the semiconductor in opposite directions. In an n–type semiconductor, the photoinduced minority carriers (holes) migrate to the surface to participate in the oxygen evolution reaction and the majority carriers (electrons) are driven through an external circuit to carry out the H_2 evolution reaction at the counter electrode.[16] However, additional overpotential is required to compensate the energy losses associated with the photogenerated holes in passing through the space charge region and electrons in transferring through the external circuit to the counter electrode (e.g. platinum).[18] In a PEC cell, electrons and holes are separated to different electrodes thus decreasing the possibilities of recombination. Additionally, the chances of back reaction are much reduced as H_2 and O_2 are evolved at different locations i.e. at the photocathode and photoanode surface respectively, and the reaction products can be collected in separate chambers.[22, 23] However, a drawback that acts as a barrier to the implementation of practical PEC cell for water splitting is the cost of constructing long lived and efficient PEC system.

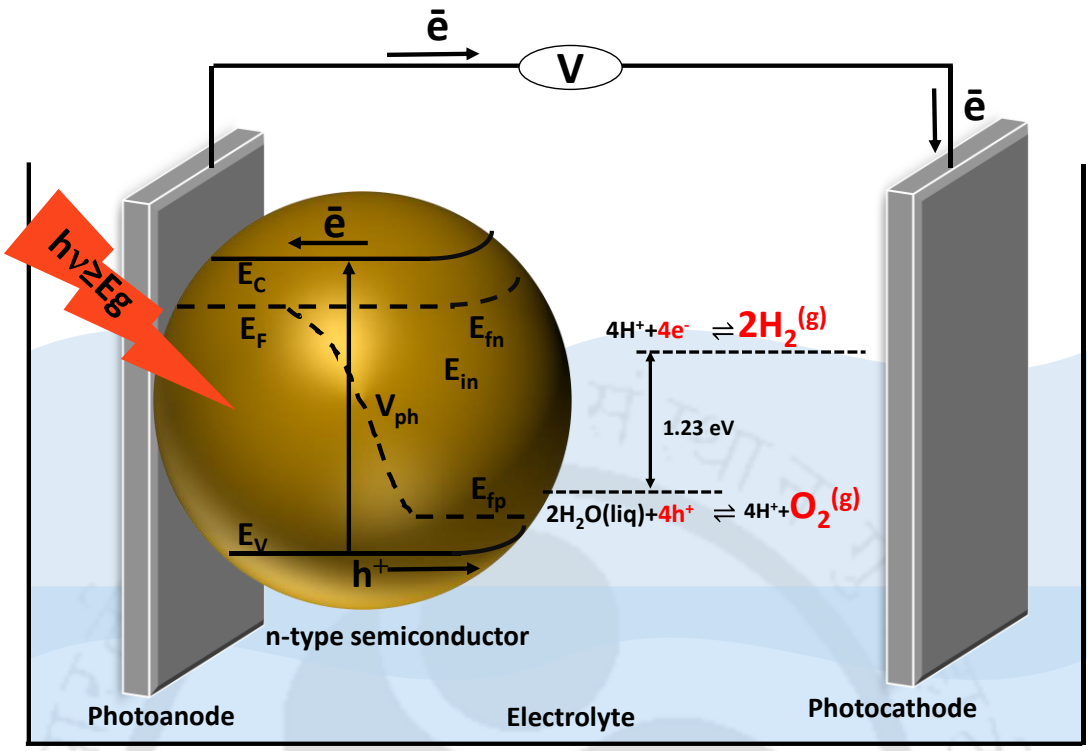

Figure 1.3: Schematic representation of the basic principle of a photoelectrochemical water splitting cell considering an n–type semiconductor as the photoanode. The electrons transferred to the counter electrode, and the holes migrate to the surface to participate in the surface redox reactions. Ev: valence band edge, Ec: conduction band edge, E_f: Fermi level, E_{fn}: quasi–Fermi level of electrons, E_{fp}: quasi–Fermi level of holes, E_{in}: built–in electric field in depletion region. Adopted from Ref. 18.

1.3 USE OF SACRIFICIAL REAGENTS

As seen in **Section 1.2.1**, in a powdered photocatalysis, reverse reaction of the products is more likely, due to the close proximity of the products formed. Also, as the simultaneous reduction and oxidation of water is a complex multistep reaction, application of photocatalysis for overall water decomposition employing pure water is practically less feasible.[24] Thus, a photocatalytic reaction can be carried out in the presence of a reducing or an oxidising reagent, that is, hole scavengers or electron scavengers. In the presence of a reducing agent, photogenerated holes oxidize the reducing reagent instead of water. As holes are scavenged by the reducing agents, the chance of charge carrier recombination can be greatly reduced and more number of electrons are available for the reduction reaction.[25]

Further, back reaction to produce water is suppressed, as O_2 is not produced, thus increasing the H_2 yield and avoiding a subsequent gas separation stage. These sacrificial reagents can be basically divided into organic and inorganic electron donors. Organic compounds such as hydrocarbons, alcohols and organic acids are employed as hole scavengers (i.e., as electron donors) for photocatalytic H_2 generation.[26] Inorganic sacrificial reagents such as sulfide, S^{2-}, and sulfite, SO_3^{2-}, are widely used for the photocatalytic H_2 generation as they are efficient hole acceptors, thus enabling the effective separation of the charge carriers.[27, 28] Similarly, photogenerated electrons in the conduction band can be consumed by oxidizing reagents (i.e. electron scavengers) such as Fe^{3+}, Ag^+ etc. which leads to enhanced O_2 evolution reaction.[29, 30] The schematic representation for H_2 and O_2 production in the presence of electron and hole scavengers is illustrated in **Figure 1.4**. Photocatalytic H_2 and O_2 generation from water in the presence of sacrificial reagents are considered as semi reactions or half–reactions of water splitting, and are used to assess the catalytic activity of the photocatalysts.[31, 24]

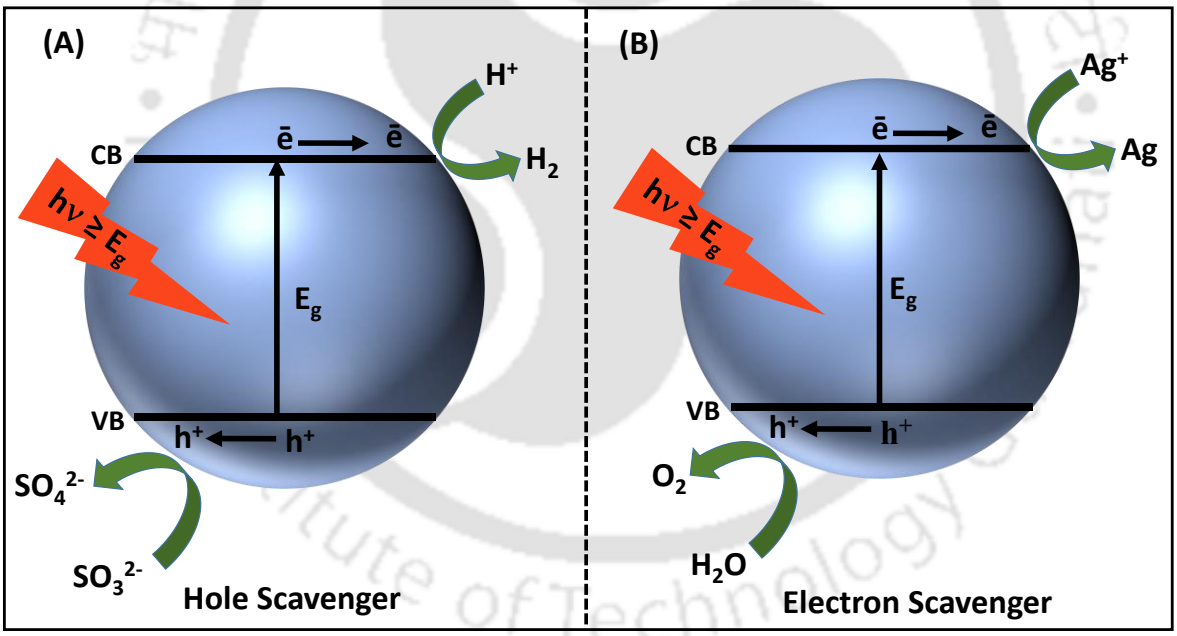

Figure 1.4: (A) Photocatalytic hydrogen production and (B) photocatalytic oxygen production by semiconductors in presence of sacrificial reagents. Adopted from Ref. 10.

1.4 PHOTOCATALYST REQUIREMENTS AND STRATEGIES TO DEVELOP EFFICIENT PHOTOCATALYSTS

In view of the various processes involved in the photo–driven water splitting process on a semiconductor as discussed in **Section 1.2**, apart from the thermodynamic criteria of band energy and band positions, there are functional requirements to be fulfilled by the semiconductor photocatalyst such as: **(i)** suitable visible–light absorption capability with appropriate band edge potentials for overall water splitting; **(ii)** efficient separation of photogenerated electrons from reactive holes; **(iii)** reduction of energy losses associated with charge transport and recombination of photo generated charges; **(iv)** chemical stability to prevent corrosion and photocorrosion in aqueous environments; **(v)** efficient kinetics of electron transfer reaction at photocatalyst surface–water interface and **(vi)** lowered cost and toxicity of photocatalyst. Although a large number of semiconductor materials have been identified, hardly any material can satisfy all of the necessary requirements.[11] In order to enhance the overall efficiency of photocatalyst materials, several strategies are adopted as discussed below:

1.4.1 Band Gap Engineering

In order to make semiconductors absorb in the visible region, band gap can be optimized by introducing chemical impurities or structural defects into the semiconductor lattice. Doping with metal, non–metal or co–doping are widely studied. Metal ion dopants can introduce a donor level above the valence band or an acceptor level below the conduction band in wide band gap semiconductors thus narrowing the band gap and enhance visible light activity. Doping of non–metal ions (such as C, N, S etc.) may result in upshift of the valence band edge of a wide band gap semiconductor.[26]

Another promising way of tuning band gap is by fabrication of multi–component semiconductor in which band gap can be tuned by changing composition via the control of stoichiometry of the constituent elements. It can also utilize the advantages of the different components.[32, 33] As an example, CdS is a promising visible light active photocatalyst due to its appropriate band width and band edge position. However, it suffers from drawback such as faster recombination of photo–generated charge carriers due to a smaller band gap (~ 2.4 eV) and photo–corrosion under visible–light irradiation. The band gap can be optimized by

combining with another wide band gap semiconductor, ZnS, to form $Zn_{1-x}Cd_xS$ solid solution.[34] A great variety of multicomponent semiconductor solid solutions, such as $LaTiO_2N$,[35] $(Ga_{1-x}Zn_x)(N_{1-x}O_x)$,[36] $(AgIn)_xZn_{2(1-x)}S_2$,[28] $ZnS–CuInS_2–AgInS_2$,[37] $(CuGa)_{1-x}Zn_{2x}S_2$,[38] $Mn_xCd_{1-x}S$,[39] $Zn_{1-x}Cd_xS$[40, 41] etc. are widely studied for photocatalytic water splitting.

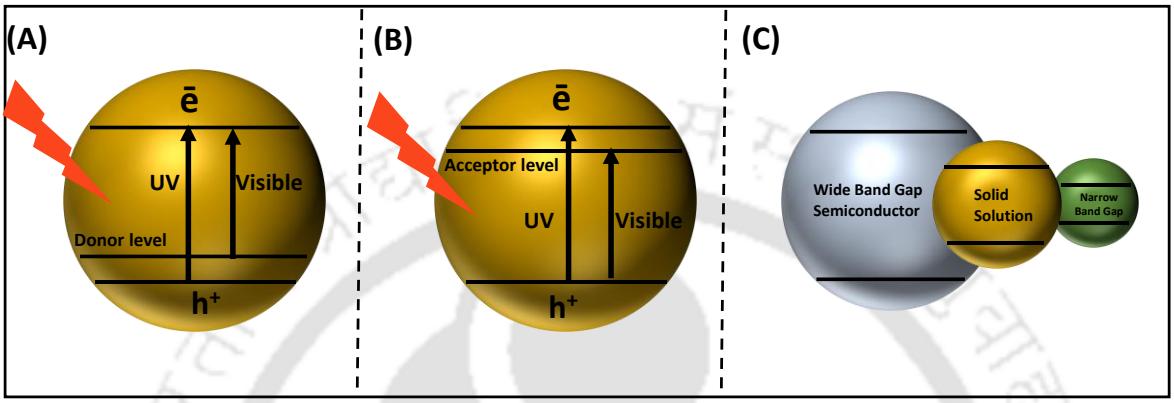

Figure 1.5: Optimisation of band gap by (A–B) doping, (C) solid solution. Adopted from Ref. 55.

1.4.2 Micro/nano Engineering

Compared to bulk materials, semiconductor nanomaterials have advantages of increased surface areas, more number of active sites and increased surface area to volume ratios, short diffusion length, which leads to an efficient separation of photo generated charge carriers.[42] The activity of nanomaterials is largely enhanced with a decrease in the particle size, which is proved by many examples like Fe_2O_3, [43] CdS, [44] etc. in which the smaller size and higher surface area showed enhanced photocatalytic activity. There have been several efforts directed towards development of materials with increased active sites, specific surface area, interfacial transport and readily accessible surface catalytic sites. Development of three dimensional (3D) hierarchical architectures formed by the assembly of nanostructured building blocks such as nanoclusters, nanosheets, nanowires etc. show improved activity due to the anisotropic properties and high specific surface areas due to the nanostructured building blocks.[45] Simple hierarchical microarchitecture, comprising of nanoflowers, proves excellent photocatalytic activity due to combination of several factors, such as high surface areas, presence of mesopores, better interfacial contacts of the semiconductor with the reactant molecules etc. For example, 3D flowerlike nanostructures of metal sulfides like CdS, [46]

$CuInS_2$, [47] ZnS, [48] $ZnIn_2S_4$, [49] etc. exhibited enhanced photocatalytic activity for H_2 generation from water splitting.

1.4.3 Co–catalyst Engineering

The final step in photocatalytic water splitting, i.e., water oxidation and reduction, is promoted by the presence of a H_2–evolution or O_2–evolution co–catalyst, which could efficiently extract photogenerated charge carriers, can act as active sites to host for catalytic H_2 or O_2 evolution and improve the stability of photocatalysts by suppressing photo–corrosion.[50] Co–catalysts minimize the overpotential required to drive the multi electron processes of hydrogen evolution reaction (HER) and oxygen evolution reaction (OER), and helps in reduction of the activation energy necessary for gas evolution.[51, 52] Another function of loading a co–catalyst is to provide a junction/interface between the co–catalysts and semiconductor to enhance electron-hole separation or charge transport.[52] Therefore, co–catalysts play a significant role in improving both the activity and stability of semiconductor photocatalysts. However, excessive loading of co–catalyst could decrease the photocatalytic activity of a semiconductor due to covering of active sites on the semiconductor, shielding the incident light on the photocatalyst, decreasing the surface area or by acting as recombination centre.[53] Since the first introduction of loading Pt as a co–catalyst onto the surface of TiO_2 by Kraeutler and Bard in 1978, [54] co–catalyst loading is widely used to obtain high activities and to increase the reaction rates in photocatalysis. Best known co–catalysts for the hydrogen evolution reaction (HER) are generally precious metals (e.g., Rh, Pd, Ir and Pt).[55] However, as an alternate to rare and expensive noble metals, several earth abundant and low–cost transitional metals, such as Co,[56] Ni[57] and Cu,[58] are widely used. The loading of these metals on semiconductor surface leads to the formation of a Schottky barrier at the metal/semiconductor interface. The Schottky barrier is a kind of junction, which could promote charge separation.[50] Several transition metal oxides, such as NiO,[59] NiOx,[60] CuO[61] etc. are well–known as noble–metal–free co–catalysts for photocatalytic H_2 production. Many transition metal sulfides, such as FeS,[62] NiS,[62] NiS_2,[63] CuS,[64] MoS_2,[65, 66] MoS_3[67] and WS_2[68] have also been widely reported as excellent candidates for cost–effective co–catalysts with an aim to substitute for noble metals in photocatalytic H_2 evolution.[50]

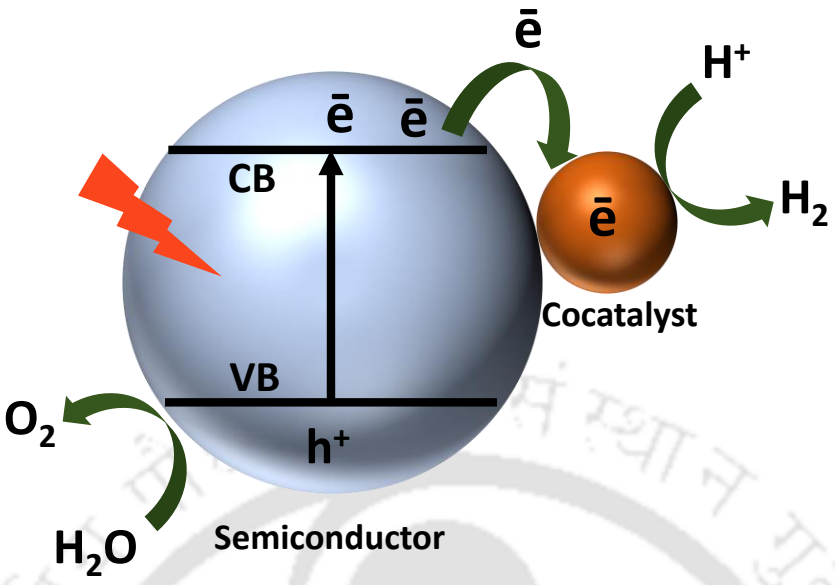

Figure 1.6: Schematic illustration of photocatalytic hydrogen production in the presence of a co–catalyst. Adopted from Ref. 50.

1.4.4 Interface Engineering

For efficient separation of the photogenerated electron–hole pairs, interface engineering by formation of heterojunctions is proved to be one of the most promising ways due to its feasibility and effective spatial separation of the photogenerated charge carriers at the heterojunction interface. A heterojunction, generally, is defined as the interface between two semiconductors with dissimilar band structure resulting in a band alignment for favourable charge transfer.[69, 70] Junction of two or more semiconductors or a semiconductor/co–catalyst junction plays a crucial role in enhancing the photocatalytic or PEC activity for water splitting. Favourable charge transfer from a semiconductor to another semiconductor (or a co–catalyst) in a heterojunction basically depends on the electronic properties and an efficient interaction among the components. Typically, conventional heterojunction photocatalysts are of three types — type–I (straddling gap) heterojunction, type–II (staggered gap) heterojunction, and type–III (broken gap).[71] In type–I heterojunction (**Figure 1.7 (A)**), the electron–hole pair cannot effectively separate as electrons and holes get accumulated on the same semiconductor. Further, as the site for reduction reaction is the semiconductor with lower redox potential, redox ability of the heterojunction is reduced. In type–II heterojunction (**Figure 1.7 (B)**), because of the feasible band alignments, electrons

migrate to semiconductor B while holes will transfer to semiconductor A under light irradiation, thus spatially separating the electron–hole pairs. However, the redox ability in a type–II heterojunction is also compromised as the site for the reduction and the oxidation reaction is at a lower reduction potential and lower oxidation potential, respectively. In type–III heterojunction (**Figure 1.7 (C)**), the electron–hole migration and thus separation is not possible as the bandgaps of the semiconductors do not overlap due to very high staggered gap. Among the conventional heterojunctions, type II heterojunction is the most effective, due to its suitable alignment for efficient separation of electron–hole pairs, wide range of absorption of light, and faster mass transfer and it is widely studied for enhancing photocatalytic activity e.g. TiO_2/g–C_3N_4,[72] $BiVO_4/WO_3$,[73] $CuSbSe_2/TiO_2$[74] etc. In the conventional heterojunctions, electron–hole separation occurs efficiently at the cost of the redox ability of the photocatalyst, as the site for reduction and oxidation processes has a lower reduction and oxidation potential, respectively.[75] As a solution to this problem, in 1979, Bard et al. proposed a Z–scheme heterojunction system wherein the redox potential of the photocatalytic system is increased.[76] A conventional Z–scheme photocatalytic system consists of two different semiconductors, A and B, and a reversible redox couple (e.g. I^-/IO^{3-}, Fe^{2+}/Fe^{3+}) (**Figure 1.7 (D)**) (e.g. Pt-$Sm_2Ti_2S_2O_5$–IO^{3-}/I^-–TiO_2) [77]or noble-metal nanoparticle (e.g. Pt, Au) as the electron mediator (e.g. CdS–Au–TiO_2,[78] TiO_2–Pt–CdS[79]). In the Z–scheme system, photogenerated electrons from the conduction band of A, migrate to the valence band of B through the redox mediator. As electrons are accumulated on semiconductor B, having a higher reduction potential, and holes get accumulated on semiconductor A, possessing higher oxidation potential, along with the spatial separation of electron–hole pairs, a higher redox ability can also be achieved in the Z–scheme heterojunction. However, conventional Z–scheme photocatalysts can only be constructed in the liquid phase (in case of shuttle redox couple) or has the drawback of utilisation of noble metal electron mediator, thereby limiting its wide range of photocatalytic application.[80] In order to overcome these disadvantages, in 2013, Yu et. al proposed a direct Z–scheme heterojunction photocatalyst concept which consists of two different semiconductors to form a heterojunction with high redox ability, without an electron mediator (**Figure 1.7 (E)**).[81] Since then, huge accomplishments have been achieved based on direct Z–scheme based photocatalysts e.g. $CuInS_2$/g–C_3N_4,[82] CdS/Co_9S_8[83] etc.

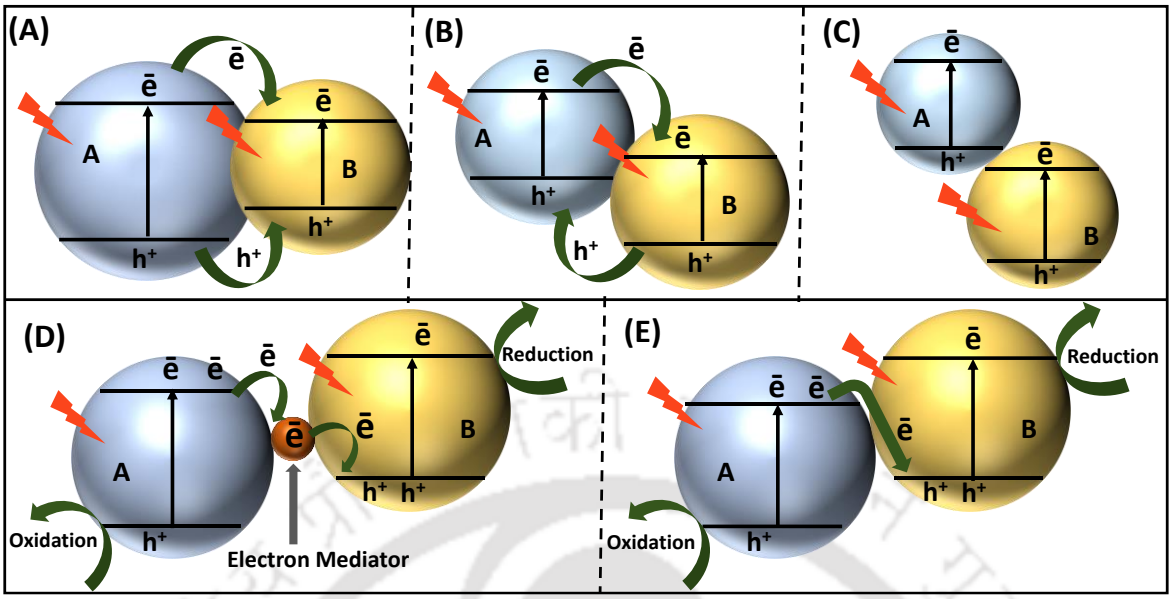

Figure 1.7: Schematic illustration of the electron–hole separation on (A) type–I, (B) type–II, (C) type–III heterojunctions, (D) Z–scheme and (E) direct Z–scheme heterojunction. Adopted from Ref. 71.

1.5 SELECTION OF SULFIDE SEMICONDUCTORS

Several semiconductors such as oxides, oxynitrides and metal sulfides are widely studied for H_2 evolution by water splitting under solar irradiation.[10] However, most of the metal oxides have a wide bandgap due to the deep O 2p orbital which constitute their valence band, thus making them mostly active under ultraviolet light, which accounts for only ~ 4% of the solar spectrum. In case of metal sulfide photocatalysts metal cations are of d^0, d^5 and d^{10} configurations. The conduction bands of sulfide photocatalysts generally comprises of d and sp orbitals, while the valence bands is constituted of S 3p orbitals, which are much more negative than O 2p orbitals, thus resulting in narrow band gaps with suitable response to the solar spectrum.[18] Most metal sulfides display negative conduction band, suggesting strong reduction ability. However, in spite of the excellent visible light responses, metal sulfide photocatalysts suffer from the drawback of photocorrosion, in which the photogenerated holes oxidize the metal sulfide photocatalyst itself. To prevent it, sulfide photocatalysts usually require hole scavengers such as S^{2-} and SO_3^{2-} to achieve photocatalytic H_2 production.[38] Numerous metal sulfides, in the presence of sacrificial reagents, have widely been reported as photocatalysts for water splitting in the past several decades. Over 30 kinds of sulfide materials can act as efficient photocatalysts for H_2 evolution via water splitting.[84]

Among them, multinary metal sulfides have attracted great attention because of the advantage of flexible constituents of more than two component elements. These inorganic compounds are advantageous due to the flexibility of using environmentally benign elemental components, tuning the band structures through alloying and thus exhibit excellent light–harvesting properties.[85, 86] Many metal sulfide photocatalysts with one or more strategies to enhance the efficiency have been reported for efficient photocatalytic activity as well as photoelectrochemical water oxidation and are tabulated in **Table 1.1** and **Table 1.2** respectively:

Table 1.1: Tabulation of some sulfide based systems /modified by one or more of the above mentioned strategies and utilised in photocatalytic hydrogen generation.

Photocatalyst	**Sacrificial reagent used**	**Rate of hydrogen evolution**	**Apparent quantum yield (AQY) (%)**	**Reference**
$Zn_{0.2}Cd_{0.8}S/MoS_2$ 3%	Na_2S (0.35 M) and Na_2SO_3 (0.25 M)	0.42 $mmolh^{-1}$ g^{-1}	—	87
$Cd_{0.2}Zn_{0.8}S/g\text{-}C_3N_4$	Na_2S (0.1 M) and Na_2SO_3 (0.1 M)	0.208 $mmolh^{-1}$	—	88
$Zn_{0.5}Cd_{0.5}S@MoS_2/RGO$	lactic acid	2.31$mmolh^{-1}$	—	89
$Pt\text{-}RuS_2\text{-}Cd_{0.5}Zn_{0.5}S$	Na_2S (0.6 M) and Na_2SO_3 (0.8 M)	0.72 $mmolh^{-1}$ g^{-1}	4%	90
$Mn_{0.8}Cd_{0.2}S/g\text{-}C_3N_4$	Na_2S (0.1 M)and Na_2SO_3 (0.5 M)	4 $mmolh^{-1}$ g^{-1}	4.1% at 420 nm	91
AuPd/ $Cd_{0.5}Zn_{0.5}S$	Na_2S (0.44 M) and Na_2SO_3 (0.31 M)	3.65 $mmolh^{-1}$ g^{-1}	—	92
$ZnS\text{-}In_2S_3\text{-}CuS$ NCs	Na_2S (0.1 M) and Na_2SO_3 (1.2 M)	0.036 $mmolh^{-1}$ g^{-1}	22.6% at 420 nm	93
Ag_2S/CdS	Na_2S (0.35 M)and Na_2SO_3 (0.25 M)	0.087 $mmolh^{-1}$	—	94
$CaIn_2S_4/g\text{-}C_3N_4$	Na_2S (0.5 M)	0.102 $mmolh^{-1}$ g^{-1}	—	95

	and Na_2SO_3 (0.5 M)			
MoS_2-$Mn_{0.2}Cd_{0.8}S$/MnS	Na_2S (0.35 M) and Na_2SO_3 (0.25 M)	0.995 $mmolh^{-1}$	—	96
1 mol% CuS/$Mn_{0.3}Cd_{0.7}S$	Na_2S (0.35 M) and Na_2SO_3 (0.25 M)	106.84 $mmolh^{-1}$ g^{-1}	—	97
$MoS_2/ZnIn_2S_4$	triethanolamine	8.898 $mmolh^{-1}$ g^{-1}	—	98
Cu_2ZnSnS_4-Pt	Na_2S (0.1 M) and Na_2SO_3 (0.1 M)	1.02 $mmolh^{-1}$ g^{-1}	—	99
MoC-QDs/C/ZIS	Lactic acid	1.131 $mmolh^{-1}$ g^{-1}	—	100
MoS_2/CQDs/$ZnIn_2S_4$	Na_2S (0.1 M) and Na_2SO_3 (0.1 M)	0.750 mmol5h^{-1}	25.6% at 420 nm	101
Cubic quantum dot/hexagonal microsphere $ZnIn_2S_4$	Na_2S (0.35 M) and Na_2SO_3 (0.25 M)	0.114 $mmolh^{-1}$	—	102
CdS quantum dot sensitized $ZnFe_2O_4/ZnIn_2S_4$	Na_2S (0.35 M) and Na_2SO_3 (0.25 M)	0.079 $mmolh^{-1}$	1.18% at 405 nm	103

Table 1.2: Tabulation of performance of some sulfide based systems or modified by one or more of the above mentioned strategies and utilised in photoelectrochemical water oxidation

Photocatalyst	**Synthesis method**	**Electrolyte**	**Photocurrent generated ($mAcm^{-2}$)**	**Reference**
$CuInS_2$:Sb films	Chemical bath depositon	K_2SO_3 (0.25 M) and Na_2S (0.35 M)	−8.58 (at 1.0 V vs Pt)	104
$CuInS_2$	solvothermal	Na_2SO_3 (0.1 M)	0.072 (at −0.45 V)	105
$CuIn_{0.96}Sn_{0.04}S_2$	mechanical ball milling	Na_2S (0.25 M)	3.52 (at 0 V vs Ag/AgCl)	106
Cu_2ZnSnS_4 powder	solid–state reaction	K_2SO_4 (0.1 M), Na_2HPO_4 (0.025 M), KH_2PO_4 (0.025 M)	0.3 (at 0.95 V vs Ag/AgCl)	107

$Cu_2ZnSnSe_4$ NCs	solvent assisted	NaCl (1 M)	~5 (at 1.2 V vs Ag/AgCl)	108
CZTS-Ag_2S NCs	colloidal	$Eu(NO_3)_3$ (1 M)	0.58 (at 0.5 V vs Ag/AgCl)	109
$CuInS_2$ nanorod array	template–assisted	Na_2SO_4 (0.5 M)	0.01 (at 0.3 V vs RHE)	110
$CuInS_2$-MoS_2	hydrothermal	Na_2SO_4 (0.5 M)	7.8×10^{-3}	111
$(Cu_2Sn)_{x/3}Zn_{1-x}S$	solvothermal	Na_2SO_4 (0.2 M)	0.31 (at 0.3 V)	112
In_2S_3/Co-Pi	hydrothermal	Na_2S (0.35 M) and Na_2SO_3 (0.25 M)	0.68 (at 1.23 V vs RHE)	113
graphene/CdS/Ag_2S	SILAR	Na_2S (0.1 M)	5.18	114
$Cu_xZn_{1-x}In_2S_4$@TiO_2 nanotube array	solvothermal	Na_2S (0.24 M) and Na_2SO_3 (0.35 M)	1.11 (at 0.6 V vs Ag/AgCl)	115

1.6 PHOTOCATALYTIC DYE DEGRADATION

The rapid advancement of industrial revolution has brought in a wide scale of problems to the society, apart from its developmental contributions. One of the major issues is contamination of water due to disposal of harmful industrial waste directly into water bodies which leads to adverse effect on the environment and wildlife. Among all industrial wastes, textile waste is one of the most harmful contaminant based on the amount and composition of the effluents from the textile industries.[116] The textile industries produces more than 7×10^5 tons of dyes per annum, and about 10–15% of these dyes are discharged as effluents into the water bodies during manufacturing and processing procedures.[117] Many methods like precipitation, adsorption, flocculation, flotation, electrochemical, oxidation, reduction, aerobic, anaerobic, and biological treatment methods are conventionally used for water treatment. However, these methods fail in complete degradation of the dyes as they have limitations such as less efficiency and production of secondary sludge, which has to be further disposed thus making them less effective.[118] Hence, there has been constant search

among industrialists and researchers for an eco–friendly treatment method to completely degrade the pollutants. Presently, much of the degradation of synthetic dyestuff in industry is carried out by heterogeneous photocatalyst by formation of highly reactive chemical species that degrade the pollutant/dye molecules into biodegradable compounds and is known as the advanced oxidation process (AOP). In AOP, pollutants are completely oxidised into simple molecules like water and carbon dioxide in the presence of strong radicals ($OH^{\bullet}$ and $O_2^{\bullet-}$) . AOP has been approved by the Environmental Protection Agency (EPA) as the best available technology to meet the standard to provide safety and sufficiently control the pollution of industrial processes and contaminated sites. There are several different ways to produce these oxidative radicals via AOP, viz., Fenton based processes, ozone based processes, photocatalysis etc.[119–122] Conventional AOPs can be classified into two types — (a) non–photochemical and (b) photochemical AOPs. Photocatalytic degradation technology, a photochemical AOP, generates radicals for the degradation of contaminants in the presence of a semiconductor photocatalyst. The basic mechanism of photocatalytic dye degradation is represented in **Figure 1.8** and it involves the following steps: **(i)** absorption of photons of energy (hν) greater than the band gap of the semiconductor, which result in generation of an electron–hole pair in the conduction and valence band respectively. (**Equation (1.6)**). **(ii)** reaction of the photogenerated e^- and h^+ with available oxidants and reductants, respectively. The photogenerated electrons could reduce the dye or react with electron acceptors such as O_2 adsorbed on surface of the catalyst or dissolved in water, reducing it to superoxide radical anion ($O_2^{\bullet-}$). The photogenerated holes, on the other hand, can oxidize the organic molecule to form R^+, or react with OH^-or H_2O, oxidizing them into $OH^{\bullet}$ radicals. (**Equation (1.7)** and **Equation (1.8)**) **(iii)** The $OH^{\bullet}$ radicals could combine to form highly oxidant species, H_2O_2 (**Equation (1.9)**). **(iv)** The resulting radical, $OH^{\bullet}$, being a very strong oxidizing agent (standard redox potential +2.8 V) can oxidize most azo dyes to the mineral end–products, carbon dioxide and water (**Equation (1.10)** and **Equation (1.11)**). All the steps can be summarised as follows: [123, 124]

$$\text{Photocatalyst} + h\nu \longrightarrow h_{VB}^{+} + e_{CB}^{-} \qquad \textbf{(1.6)}$$

$$e_{CB}^{-} + O_2 \longrightarrow O_2^{\bullet-} \qquad \textbf{(1.7)}$$

$$h_{VB}^{+} + H_2O \longrightarrow OH^{\bullet} + H^{+} \qquad \textbf{(1.8)}$$

$$OH^{\bullet} + OH^{\bullet} \longrightarrow H_2O_2 \qquad \textbf{(1.9)}$$

$$H_2O_2 + O_2^{\bullet -} \longrightarrow OH^{\bullet} + OH^{-} + O_2 \qquad \textbf{(1.10)}$$

$$Dye + OH^{\bullet} \longrightarrow CO_2 + H_2O \qquad \textbf{(1.11)}$$

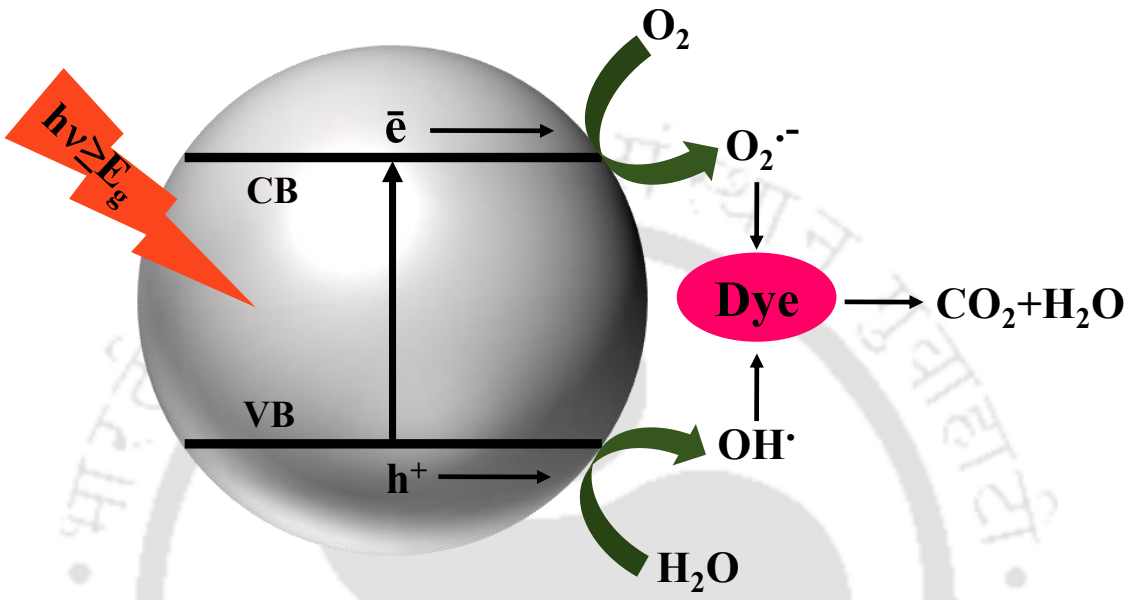

Figure 1.8: Schematic illustration of photocatalytic dye degradation process. Adopted from Ref. 118.

1.7 SCOPE OF THIS THESIS WORK

As discussed in **Section 1.5**, sulfide semiconductors constitute a promising class of heterogeneous photocatalyst owing to its suitable band gap for absorbing visible region of the spectrum. Furthermore, most sulfide semiconductors possess negative conduction band, suggesting strong reduction ability thus proving to be a promising H_2 evolution catalyst. However, sulfide semiconductor materials suffer from the drawback of charge carrier recombination owing to the small band gap. Thus in the present work, taking model sulfide semiconductors, the increase in photocatalytic and photoelectrochemical water oxidation and dye degradation is studied by adopting one or more of the widely adopted strategies as discussed in **Section 1.5**. The work carried out in this thesis constitute of the following objectives:

- Design and synthesis of different multinary sulfide semiconductors for utilization in photocatalytic application
- Improving the charge carrier availability and efficient absorption of solar irradiation by designing strategies like formation of heterojunction with other semiconductors with suitable band positions, formation of solid solution, utilization of co–catalyst and formation of direct Z–scheme heterojunction
- Understanding the details of the charge transfer mechanism and carrier dynamics in the designed systems leading to the enhanced photocatalytic activity in the modified systems
- Application of the designed semiconductor heterostructures for improved photocatalytic water oxidation as well as dye degradation (Chapter 3 and 4) and photoelectrochemical water oxidation (Chapter 5) compared to the bare counterpart

1.8 REFERENCES

1. R. York and S. E. Bell, *Energy Res. Soc. Sci*., 2019, **51**, 40.
2. https://www.eia.gov/outlooks/ieo/pdf/0484(2017).
3. N. S. Lewis and D. G. Nocera, *Proc. Nat. Acad. Sci.*, 2006, **103**, 15729.
4. T. M. Letcher, *Managing Global Warming An Interface of Technology and Human Issues*, Academic Press, Elseveir, 2019.
5. C. Philibert, *Technology Roadmap: Solar Photovoltaic Energy*, International Energy Agency, 2014.
6. R. Kato and H. Nishide, *Polym. J.*, 2018, **50**, 77.
7. P. Corbo, F. Migliardin and O. Veneri, Hydrogen Fuel Cells for Road Vehicles, Green Energy and Technology, DOI: 10.1007/978-0-85729-136-3_2.
8. A. Züttel, A. Borgschulte and L. Schlapbach, *Hydrogen as a Future Energy Carrier*, Wiley–VCH Verlag GmbH&Co. KGaA, Weinheim, 2008.
9. R. van de Krol and M. Grätzel, *Photoelectrochemical Hydrogen Production*, Springer US, 2012.
10. A. Kudo and Y. Miseki, *Chem. Soc. Rev.*, 2009, **38**, 253.
11. R. M. N. Yerga, M. C. Á. Galvan, F. del Valle, J. A. V. Mano and J. L. G. Fierro, *ChemSusChem*, 2009, **2**, 471.
12. W. J. Albery and N. B. Philip, *J. Electrochem. Soc*., 1984, **131**, 315.

13. F. E. Osterloh, *Chem. Mater*., 2008, **20**, 35.
14. M. D. Hernandez-Alonso, F. Fresno, S. Suarez and J. M. Coronado, *Energy Environ. Sci*., 2009, **2**, 1231.
15. A. Fujishima and K. Honda, *Nature*, 1972, **238**, 37.
16. Z. Chen, H. N. Dinh and E. Miller, *Photoelectrochemical Water Splitting: Standards, Experimental Methods, and Protocols*, Springer, 2013.
17. J. Li and N. Wu, *Catal. Sci. Technol.*, 2015, **5**, 1360.
18. C. Jiang, S. J. A. Moniz, A. Wang, T. Zhang and J. Tang, *Chem. Soc. Rev.,* 2017, **46**, 4645.
19. S. Licht, A. J. Bard and M. Stratmann, *Semionductor eletrodes and Photoelectrochemistry*, Wiley–VCH, Weinheim, 2002.
20. J. Dashdorj, R. Ahrenkiel and W. Metzger, *Mater. Res. Soc. Symp. Proc*, 2004, **799**, Z4.5.1.
21. T. Yao, X. An, H. Han, J. Q. Chen and C. Li, *Adv. Energy Mater*., 2018, 1800210.
22. D. A. Tryk, A. Fujishima and K. Honda, *Electrochim. Acta*, 2000, **45**, 2363.
23. L. Li, P. A. Salvador and G. S. Rohrer, *Nanoscale*, 2014, **6**, 24.
24. J. Schneider and D. W. Bahnemann, *J. Phys. Chem. Lett*. 2013, **4**, 3479.
25. T. Kawai and T.Sakata, *Nature*, 1980, **286**, 474.
26. X. B. Chen, S. H. Shen, L. J. Guo and S. S. Mao, *Chem. Rev*., 2010, **110**, 6503.
27. W. F. Yao, X. L. Song, C. P. Huang, Q. J. Xu and Q. Wu, *Catal. Today*, 2013, **199**, 42.
28. I. Tsuji, H. Kato, H. Kobayashi and A. Kudo, *J. Am. Chem. Soc*., 2004, **126**, 13406.
29. A. Ishikawa, T. Takata, J. N. Kondo, M. Hara, H. Kobayashi and K. Domen, *J. Am. Chem. Soc*., 2002, **124**, 13547.
30. T. Ohmori, H. Takahashi, H. Mametsuka and E. Suzuki, *Phys. Chem. Chem. Phys*., 2000, **2**, 3519.
31. J. Yoshimura, Y. Ebina, J. Kondo, K. Domen and A. Tanaka, *J. Phys. Chem.* 1993, **97**, 1970.
32. K. Maeda, T. Takata, M. Hara, N. Saito, Y. Inoue, H. Kobayashi and K. Domen, *J. Am. Chem. Soc.*, 2005, **127**, 8286.
33. D. Wang, T. Kako and J. Ye, *J. Am. Chem. Soc*., 2008, **130**, 2724.
34. J. Yu, J. Zhang and M. Jaroniec, *Green Chem*., 2010, **12**, 1611.

35. F. Zhang, A. Yamakata, K. Maeda, Y. Moriya, T. Takata, J. Kubota, K. Teshima, S. Oishi and K. Domen, *J. Am. Chem. Soc*., 2012, **134**, 8348.
36. K. Maeda, K. Teramura, D. Lu, T. Takata, N. Saito, Y. Inoue and K. Domen, *Nature*, 2006, **440**, 295.
37. I. Tsuji, H. Kato and A. Kudo, *Angew. Chem., Int. Ed*., 2005, **44**, 3565.
38. T. Kato, Y. Hakari, S.Ikeda, Q. Jia, A. Iwase and A. Kudo, *J. Phys. Chem. Lett*. 2015, **6**, 1042.
39. L. Li, G. Liu, S. Qi, X. Liu, L. Gu, Y. Lou, J. Chen and Y. Zhao; *J. Mater. Chem. A*, 2018, **6**, 23683.
40. J. Zhang, L. Qi, J. Ran, J. Yu and S. Z. Qiao, *Adv. Energy Mater*., 2014, **4**, 1301925.
41. Q. Li, H. Meng, P. Zhou, Y. Zheng, J. Wang, J. Yu and J. Gong, *ACS Catal*., 2013, **3**, 882.
42. A. Bard and M. Fox, *Acc. Chem. Res*., 1995, **28**, 141.
43. T. K. Townsend, E. M. Sabio, N. D. Browning and F. E. Osterloh, *Energy Environ. Sci.*, 2011, **4**, 4270.
44. C. Li, J. Yuan, B. Han and W. Shangguan, *Int. J. Hydrogen Energy*, 2011, **36**, 4271.
45. B. Li and Y. Wang, *J. Phys. Chem. C*, 2009, **114**, 890.
46. Y. Liu, Y. Ma, W. Liu, Y. Shang, A. Zhu, P. Tan, X. Xiong and J. Pan, *J. Colloid Interface Sci.*, 2018, **513**, 222.
47. L. Zheng, Y. Xu, Y. Song, C. Wu, M. Zhang and Y. Xie, *Inorg. Chem*., 2009, **48**, 4003.
48. J. Zhang, Y. Wang, J. Zhang, Z. Lin, F. Huang and J. Yu, *ACS Appl. Mater. Interfaces*, 2012, **5**, 1031.
49. N. S. Chaudhari, S. S. Warule and B. B. Kale; *RSC Adv*., 2014, **4**, 12182.
50. J. Ran, J. Zhang, J. Yu, M. Jaroniec and S. Z. Qiao, *Chem. Soc. Rev.,* 2014, **43**, 7787.
51. K. Maeda and K. Domen, *J. Phys. Chem. Lett*., 2010, **1**, 2655.
52. F. E. Osterloh and B. A. Parkinson, *MRS Bull*., 2011, **36**, 17.
53. N. Chouhan, R. –S. Liu and J. Zhang, *Photochemical Water Splitting: Materials and Applications*, CRC Press, 2017.
54. B. Kraeutler and A. J. Bard, *J. Am. Chem. Soc*., 1978, **100**, 4317.
55. X. Li, J. Yu, J. Low, Y. Fang, J. Xiao and X. Chen, *Mater. Chem. A*, 2015, **3**, 2485.
56. P. D. Tran, L. F. Xi, S. K. Batabyal, L. H. Wong, J. Barber and J. S. C. Loo, *Phys. Chem. Chem. Phys*., 2012, **14**, 11596.

57. C. Dinh, M. Pham, F. Kleitzb and T. Do, *J. Mater. Chem. A*, 2013, **1**, 13308.
58. W. J. Foo, C. Zhang and G. W. Ho, *Nanoscale*, 2013, **5**, 759.
59. A. K. Agegnehu, C. J. Pan, J. Rick, J. F. Lee, W. N. Su and B. J. Hwang, *J. Mater. Chem*., 2012, **22**, 13849.
60. J. Choi, S. Y. Ryu, W. Balcerski, T. K. Lee and M. R. Hoffmann, *J. Mater. Chem*., 2008, **18**, 2371.
61. J. G. Yu, Y. Hai and M. Jaroniec, *J. Colloid Interface Sci*., 2011, **357**, 223.
62. M. Tabata, K. Maeda, T. Ishihara, T. Minegishi, T. Takata and K. Domen, *J. Phys. Chem. C*, 2010, **114**, 11215.
63. Y. P. Yuan, S. W. Cao, L. S. Yin, L. Xu and C. Xue, *Int. J. Hydrogen Energy*, 2013, **38**, 7218.
64. L. J. Zhang, T. F. Jiang, S. Li, Y. C. Lu, L. L. Wang, X. Q. Zhang, D. J. Wang and T. F. Xie, *Dalton Trans*., 2013, **42**, 12998.
65. X. Zong, H. J. Yan, G. P. Wu, G. J. Ma, F. Y. Wen, L. Wang and C. Li, *J. Am. Chem. Soc*., 2008, **130**, 7176.
66. F. A. Frame and F. E. Osterloh, *J. Phys. Chem. C*, 2010, **114**, 10628.
67. M. L. Tang, D. C. Grauer, B. Lassalle-Kaiser, V. K. Yachandra, L. Amirav, J. Yano, J. R. Long and A. P. Alivisatos, *Angew. Chem., Int. Ed*., 2011, **50**, 10203.
68. X. Zong, J. F. Han, G. J. Ma, H. J. Yan, G. P. Wu and C. Li, *J. Phys. Chem. C*, 2011, **115**, 12202.
69. K. Vinodgopal and P. V. Kamat, *Environ. Sci. Technol.*, 1995, **29**, 841.
70. K. Ranjit and B. Viswanathan, *J. Photochem. Photobiol., A*, 1997, **108**, 79.
71. J. Low, J.Yu, M. Jaroniec, S. Wageh, and A. A. Al-Ghamdi; *Adv. Mater*., 2017, **29**, 1601694.
72. K. Li, S. Gao, Q. Wang, H. Xu, Z. Wang, B. Huang, Y. Dai and J. Lu, *ACS Appl. Mater. Interfaces*, 2015, **7**, 9023.
73. S. J. Hong, S. Lee, J. S. Jang and J. S. Lee, *Energy Environ. Sci.*, 2011, **4**, 1781.
74. A. S. Kshirsagar, and P. K. Khanna, *Mater. Chem. Front.*, 2019, **3**, 437.
75. K. Maeda, *ACS Catal.*, 2013, **3**, 1486.
76. A. J. Bard, *J. Photochem.*, 1979, **10**, 59.
77. W. Zhao, K. Maeda, F. Zhang, T. Hisatomi and K. Domen, *Phys. Chem. Chem. Phys.*, 2014, **16**, 12051.

78. H. Tada, T. Mitsui, T. Kiyonaga, T. Akita and K. Tanaka, *Nat. Mater.* 2006, **5**, 782.
79. Y. Wei, J. Jiao, Z. Zhao, W. Zhong, J. Li, J. Liu, G. Jiang and A. Duan, *J. Mater. Chem. A*, 2015, **3**, 11074.
80. J. Low, C. Jiang, B. Cheng, S. Wageh, A. A. Al-Ghamdi and J. Yu, *Small Methods*, 2017, **1**, 1700080.
81. J. G. Yu, S. H. Wang, J. X. Low and W. Xiao, *Phys. Chem. Chem. Phys.*, 2013, **15**, 16883.
82. X. Li, K. Xie, L. Song, M. Zhao and Z. Zhang, *ACS Appl. Mater. Interfaces*, 2017, **9**, 24577.
83. B. Qiu, Q. Zhu, M. Du, L. Fan, M. Xing and J. Zhang, *Angew. Chem. Int. Ed*., 2017, **56**, 2684.
84. K. Zhang and L. Guo, *Catal. Sci. Technol.*, 2013, **3**, 1672.
85. M. D. Regulacio and M. –Y. Han, *Acc. Chem. Res*., 2016, **49**, 511.
86. S. Shen and Q. Wang, *Chem. Mater*., 2013, **25**, 1166.
87. M. Nguyen, P. D. Tran, S. S. Pramana, R. L. Lee, S. K. Batabyal, N. Mathews, L. H. Wong and M. Graetzel, *Nanoscale*, 2013, **5**, 1479.
88. H. Liu, Z. T. Jin and Z. Z. Xu, *Dalton Trans.*, 2015, **44**, 14368.
89. R. Du, Y. Zhang, B. Li, X. Yu, H. Liu, X. An and J. Qu, *Phys. Chem. Chem. Phys.*, 2016, **18**, 16208.
90. A. P. Gaikwad, D. Tyagi, C.A. Betty and R. Sasikala, *Appl. Catal., A*, 2016, **517**, 91.
91. H. Liu, Z. Xu, Z. Zhang and D. Ao, *Appl. Catal., A*, 2015, **518**, 150.
92. L. Wu, J. Gong, L. Ge, C. Han, S. Fang, Y. Xin, Y. Li and Y. Lu, *Int. J. Hydrogen Energy*, 2016, **41**, 14704.
93. Y. Li, G. Chen, Q. Wang, X. Wang, A. Zhou and Z. Shen, *Adv. Funct. Mater.*, 2010, **20**, 3390.
94. S. Shen, L. Guo b, X. Chen, F. Ren and S. S. Mao, *Int. J. Hydrogen Energy*, 2010, **35**, 7110.
95. D. Jiang, J. Li, C. Xing, Z. Zhang, S. Meng and M. Chen, *ACS Appl. Mater. Interfaces*, 2015, **7**, 19234.
96. J. Wang1, J. Luo, D. Liu, S. Chen and T. Peng, *Appl. Catal. B*, 2019, **241**, 130.
97. Y. Han, X.Dong and Z. Liang, *Catal. Sci. Technol.*, 2019, **9**, 1427.
98. W. Li, Z. Lin and G. Yang, *Nanoscale*, 2017, **9**, 18290.

99. X. Yu, A. Shavel, X. An, Z. Luo, M. Ibáñez and A. Cabot, *J. Am. Chem. Soc.,* 2014, **136**, 9236.
100. F. Gao, Y. Zhao, L. Zhang, B. Wang, Y. Wang, X. Huang, K. Wang, W. Feng and P. Liu, *J. Mater. Chem. A*, 2018, **6**, 18979.
101. B. Wang, Z. Deng, X. Fu and Z. Li, *J. Mater. Chem. A*, 2018, **6**, 19735.
102. J. Wang, Y. Chen, W. Zhou, G. Tian, Y. Xiao, H. Fu and H. Fu, *J. Mater. Chem. A*, 2017, **5**, 8451.
103. Y. Chen, G. Tian, W. Zhou, Y. Xiao, J. Wang, X. Zhang and H. Fu, *Nanoscale*, 2017, **9**, 5912.
104. E. Garskaite, G.-T. Pan, T. C.-K. Yang, S.-T. Huang and A. Kareiva, *Sol. Energy*, 2012, **86**, 2584.
105. J. Xia, Y. Liu, X. Qiu, Y. Mao, J. He and L. Chen, *Mater. Chem. Phys*., 2012, **136**, 823.
106. C. Yang, M. Qin, Y. Wang, D. Wan, F. Huang and J. Lin, *Sci. Rep*., 2013, **3**, 1286.
107. K. Iwashina, A. Iwase, Y. H. Ng, R. Amal and A. Kudo, *J. Am. Chem. Soc*. 2015, **137**, 604.
108. P.-Y. Lee, S.-P. Chang and S.-J. Chang, *J. Environ. Chem. Eng*., 2015, **3**, 297.
109. X. Yu, J. Liu, A. Genç, M. Ibáñez, Z. Luo, A. Shavel, J. Arbiol, G. Zhang, Y. Zhang and A. Cabot, *Langmuir*, 2015, **31**, 10555.
110. W. Yang, Y. Oh, J. Kim, H. Kim, H. Shin and J. Moon, *ACS Appl. Mater. Interfaces*, 2016, **8**, 425.
111. Y.-J. Yuan, D.-Q. Chen, Y.-W. Huang, Z.-T. Yu, J.-S. Zhong, T.-T. Chen, W.-G. Tu, Z.-J. Guan, D.-P. Cao and Z.-G. Zou, *ChemSusChem*, 2016, **9**, 1003.
112. Z. Zhang, J. Zhu, S. Li, X. Liu and Y. Mao, *Int. J. Hydrogen Energy*, 2014, **39**, 4198.
113. D. Chen and Z. Liu, *ACS Sustainable Chem. Eng.*, 2018, **6**, 12328.
114. B. Wang, Z. Liu, J. Han, T. Hong, J. Zhang, Y. Li and T. Cui, *Electrochim. Acta*, 2015, **176**, 334.
115. Z. Wu, C. Gong, J. Yu, L. Sun, W. Xiao and C. Lin, *J. Mater. Chem. A*, 2017, **5**, 1292
116. P. Vandevivere, R. Bianchi and W. J. Verstraete, *Chem. Technol.Biotechnol*., 1998, **72**, 289.
117. W. Ruan, J. Hu1, J. Qi, Y. Hou, C. Zhou and X. Wei, *Adv. Mater. Lett.*, 2019, **10**, 09.
118. N. M. Julkapli, S. Bagheri, and S. B. A. Hamid, *Sci. World J.*, 2014, **2014**, 692307.

119. A. Babuponnusami and K. Muthukumar, *J. Environ. Chem. Eng.,* 2014, **2**, 557.

120. P. A. Gogate and A. B. Pandit, *Adv. Environ. Res.*, 2004, **8**, 501.

121. R. Andreozzi, V. Caprio, A. Insola and R. Marotta, *Catal. Today*, 1999, **53**, 51.

122. S. Rashidi, M. Nikazar, A. V. Yazdi, and R. Fazaeli, *J. Environ. Sci. Health, Part A*, 2014, **49**, 452.

123. L. V. Bora and R. K. Mewada, *Renewable Sustainable Energy Rev.*, 2017, **76**, 1393.

124. U. G. Akpan and B. H. Hameed, *J. Hazard. Mater.*, 2009, **170**, 520.

Chapter 2

Experimental Section

This chapter summarises the chemicals and materials used and basic instrumental techniques adopted for characterisation of the photocatalytic materials in the entire thesis. It describes the detailed experimental procedure for analysis of different photocatalytic activity. It also explains the various methods used for the evaluation of photocatalytic activity of the synthesised compounds.

2.1 INTRODUCTION

This chapter summarizes various materials and chemicals used in the preparation of all the compounds in this thesis. The synthesis were carried out by hydrothermal method or ultrasonic dispersion which gives product with decent yield. The detailed characterisation of the compounds were carried out by different experimental techniques which are listed in this chapter. Finally, the experimental setup and the various parameters adopted to evaluate the photocatalytic/photoelectrochemical/dye degradation activity of the compounds is described in this chapter.

2.2 MATERIALS AND CHEMICALS USED

The various chemicals used in the synthesis of the compounds and required for the different experiments are listed here. Copper(II) acetate monohydrate (Merck), zinc(II) nitrate hexahydrate (Himedia), tin(II) chloride dehydrate (Rankem), ethylenediamine (Merck), thiourea (Merck), ammonium heptamolybdate (Sigma Aldrich), cetyltrimethylammonium bromide (CTAB) (Rankem), zinc acetate dihydrate (Merck), cadmium acetate dihydrate (Merck), thioacetamide (Spectrochem), hexamine (Merck), L-cysteine (Sigma Aldrich), melamine (Sigma Aldrich), ethylenediaminetetraacetic acid disodium salt dehydrate (Himedia), *p*-Benzoquinone (Sigma Aldrich), Isopropanol (Merck), sodium sulfate anhydrous (Merck), zinc chloride (Sigma Aldrich), indium (III) chloride (Sigma Aldrich), sodium orthovanadate (Alfa Aesar), sodium sulfate (Merck), N methyl pyrollidone (Merck), terephthalic acid (Loba Chemie), sodium hydroxide (Sigma Aldrich), Nafion perfluorinated resin solution (5 wt% in lower aliphatic alcohols and water) (Sigma Aldrich), FTO coated glass substrates (Sigma Aldrich) and ethanol. All the chemicals were used as received without any further purification.

2.3 CHARACTERISATION TECHNIQUES

This section describes the various instrumental techniques used for characterisation of synthesized materials and their photocatalytic efficiency evaluation. The instruments used for different characterisations are listed below:

1. The crystal phase purity of the synthesized compounds were determined by powder X-ray diffraction patterns (PXRD) in Rigaku TTRAX III X- ray diffractometer with

Cu Kα radiation (λ = 1.540 Å) source (**Chapter 3** and **Chapter 4**) and Bruker D2 PHASER with Cu Kα X-ray generator (λ = 1.540 Å) (**Chapter 5**). The scan range was 10° − 80° with a step size of 0.03°/s

2. Morphological features of the synthesized compounds were obtained by field-emission scanning electron microscopy (FESEM) in a Zeiss Sigma instrument at an operating voltage of 3 – 10 kV
3. Elemental and compositional analysis were carried out by energy-dispersive X-ray (EDX) spectroscopic analysis using INCA, Oxford instruments
4. Structural analysis of the synthesized compounds were performed by transmission electron microscopy (TEM) in a JEOL JEM 2100 instrument at an operating voltage of 200 kV
5. Optical properties of the compounds were characterized by a UV-visible diffuse reflectance spectroscopy (UV-Vis DRS) in a JASCO V-650 spectrophotometer with an integrating sphere of 150 mm and $BaSO_4$ as an internal reflectance standard and a PerkinElmer Lambda 750 UV-visible spectrophotometer
6. The absorbance profile of Rhodamine B dye solution was measured in a Perkin Elmer Lambda 25 UV-visible spectrophotometer
7. Excited state charge transfer properties of the compounds were determined by steady-state photoluminescence spectra (PL) recorded in a Horiba Scientific Fluoromax-4 spectrophotometer
8. Excited state charge carrier kinetics were determined by time-resolved photoluminescence (TRPL) measurements performed on a LifeSpec II Edinburgh instrument
9. Fourier transformed infrared spectroscopic (FT-IR) study was performed in a PerkinElmer FT-IR instrument at room temperature with KBr pellet
10. Structural bonding nature in compounds were determined by Laser micro Raman analysis carried out in a Horiba LabRAM HR spectrometer at an excitaion of 514 nm (**Chapter 3** and **Chapter 5**) and 488 nm (**Chapter 4**)
11. Bonding state, surface properties, chemical environment and oxidation state of the compounds were characterized by X-ray photoelectron spectroscopy (XPS) carried out using a Kratos AXIS Supra photoelectron spectrometer with a monochromatized X-ray source of Al-K_α (hv = 1486.6 eV) (**Chapter 4**) and an ESCALAB Xi+ (Made:

Thermo Fisher Scientific Pvt. Ltd., UK) photoelectron spectrometer with a monochromatized Al-K_α ($h\nu$ = 1486.6 eV) X-ray source (**Chapter 5**)

12. Surface area analysis and pore size distribution in the samples were carried out in a Beckman-Coulter SA 3100 nitrogen adsorption apparatus at liquid N_2 temperature with prior degassing at 150 °C for 3h
13. Amount of gas produced in the photocatalytic experiment was analysed by gas chromatography using Nucon 5765 using a thermal conductivity detector (TCD) (**Chapter 3**), Agilent 7890A GC (**Chapter 4**) and Agilent 7820A (**Chapter 5**)
14. All the electrochemical measurements (**Chapter 4** and **Chapter 5)** were performed in a CH1120B electrochemical workstation
15. To determine the intrinsic charge transport properties in the photoelectrode, electrochemical impedance spectroscopic (EIS) analyses of the devices are performed using an electrochemical workstation provided by CH instruments model CHI680E, Inc., Austin, TX. (**Chapter 5**)

2.4 EXPERIMENTAL PROCEDURES FOR PHOTOCATALYTIC ACTIVITY

2.4.1 Photocatalytic Hydrogen Production

The photocatalytic H_2 evolution reaction from water was carried out at room temperature and atmospheric pressure in a two neck double walled borosilicate round-bottomed flask (100 mL) with a water circulation through the outer jacket. The necks of the reactor were sealed with rubber septa to prevent leakage of the gas produced. The photocatalytic reaction was initiated by irradiation from a 500 W tungsten–halogen lamp (Halonix, India) with emission profile in between the wavelength ranges 195 – 1100 nm, placed 15 cm away from the reactor. In order to carry out the experiment, definite amount of photocatalyst (0.2 g in **Chapter 3** and 0.02 g in **Chapter 4**) was dispersed in water (50 mL) with Na_2SO_3 and Na_2S (0.25 M and 0.35 M respectively in **Chapter 3**, 0.1 M and 0.1 M respectively in **Chapter 4**) as sacrificial reagents. The reactor was purged with N_2 for ~ 10 min at a flow rate of 0.1 L min^{-1} monitored by a rotameter and subsequently the system was evacuated in order to liberate the dissolved oxygen and any other gases. This process was repeated twice before irradiating the system by the light source. During irradiation, the suspension was continuously stirred so that the catalyst is uniformly exposed to the light

source. Aliquots of the gaseous headspace were collected every 15 min for a total of 1 h using a 1 mL gastight syringe, which was then analysed by gas chromatography (Nucon 5765 in **Chapter 3** and Agilent 7890A in **Chapter 4**), equipped with a thermal conductivity detector (TCD) and molesieve column with N_2 as the carrier gas. Blank reactions in the absence of photocatalyst or light were also carried out and in which case no H_2 was detected, suggesting the role of the photocatalysts in H_2 evolution. A schematic representation of the experimental setup for photocatalytic H_2 production is shown in **Figure 2.1**.

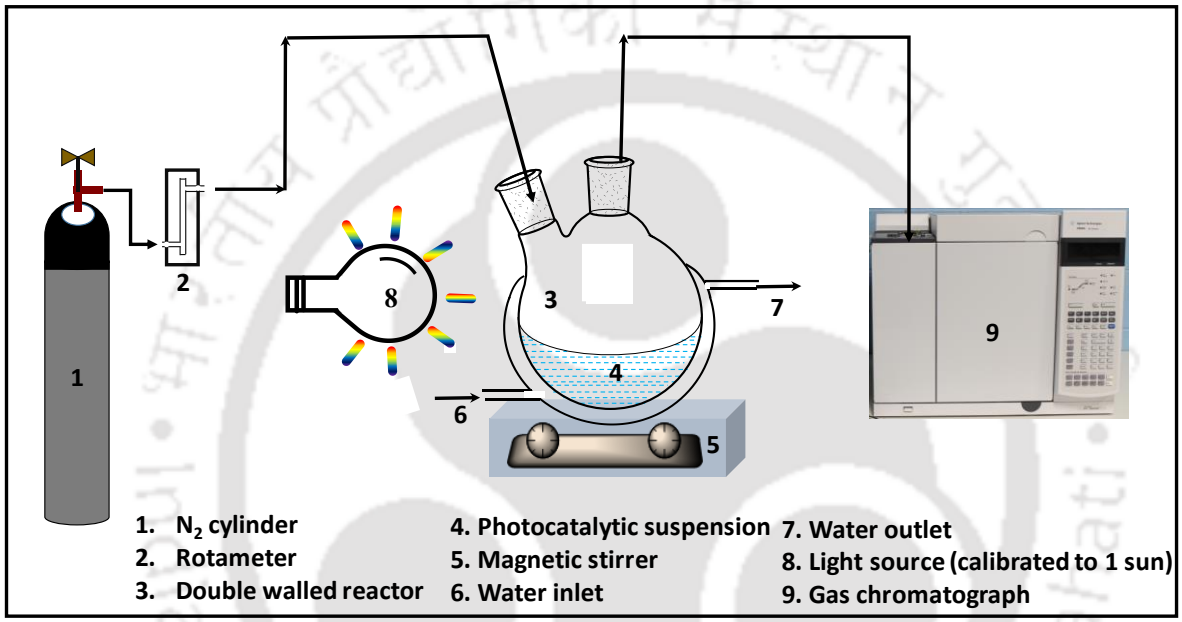

Figure 2.1: Schematic Representation of the experimental setup for photocatalytic H_2 evolution.

2.4.2 Reusability of the Photocatalysts

To examine the reusability of the photocatalyst, the best performing catalyst was tested for three cycles of the photocatalytic experiment for H_2 production. In a typical experiment specific amount of the catalyst was dispersed in 50 mL of water containing sacrificial reagents (Na_2SO_3/Na_2S) as described in **Section 2.4.1** and experiment for photocatalytic H_2 evolution was performed. After one hour of irradiation, the catalyst was washed with deionised water and ethanol and dried and the similar procedure for photocatalytic H_2 production was repeated with a fresh solution of sacrificial reagents. Similarly, the experiment was repeated for a third cycle.

2.4.3 Photocatalytic Rhodamine B Dye Degradation

The dye degradation efficiency of the catalysts were analyzed by monitoring the absorbance of Rhodamine B (RhB) dye solution. In **Chapter 3,** Rhodamine B dye degradation experiments were performed in a photochemical reactor with a double–walled immersion well that permits water circulation and it houses a MVL2 125W low pressure mercury vapour lamp as the light source to initiate the photocatalytic dye degradation reaction. The experimental setup in **Chapter 4** consisted of a double walled round bottomed flask (100 mL) irradiated with a 500 W tungsten−halogen lamp (Halonix, India) light source from a distance of 15 cm from the reactor. During the photocatalytic dye degradation experiment, photocatalyst (50 mg) was dispersed in aqueous Rhodamine B dye solution (100 mL (**Chapter 3**) and 50 mL (**Chapter 4**), 10^{-5} M). Before irradiation, the mixture was stirred in the dark for ~1 h to achieve adsorption−desorption equilibrium among the dye, photocatalyst particles, dissolved oxygen, and atmospheric oxygen. Solution aliquots (2 mL) were collected from the photoreactor in every 10 min upto 1 h followed by recording their electronic absorption spectra in the range of 200 − 800 nm. The degradation of Rhodamine B dye was determined by monitoring the decrease in the absorbance at 552 nm. The photocatalytic degradation efficiency was calculated as follows

$$\text{Efficiency}(\%) = \frac{(C_0 - C)}{C_0} \times 100$$

Where, C_0 is the initial RhB dye concentration and C is the concentration of dye after certain time of light irradiation.[1]

2.4.4 Fabrication of Photoelectrode

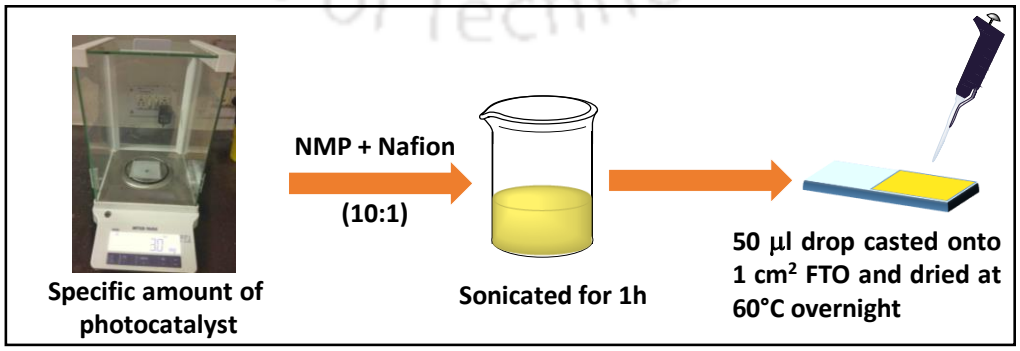

Figure 2.2: Schematic representation of various steps involved in photoelectrode preparation.

For the fabrication of photoelectrode for water oxidation, 3 mg of the catalyst was measured, followed by addition of 10 µL of Nafion solution and 100 µL of N-methyl pyrollidone and sonicated for 30 min to form a uniform slurry. 50 µL of the homogeneous catalyst ink is then uniformly drop casted onto an area of 1 cm^2 of a pre–cleaned FTO and dried at 60 °C overnight in a vacuum oven which are then used as the working electrodes for the photoelectrochemical characterisations. Step–by–step preparation of photoelectrode is shown in **Figure 2.2**.

2.4.5 Photoelectrochemical Water Oxidation

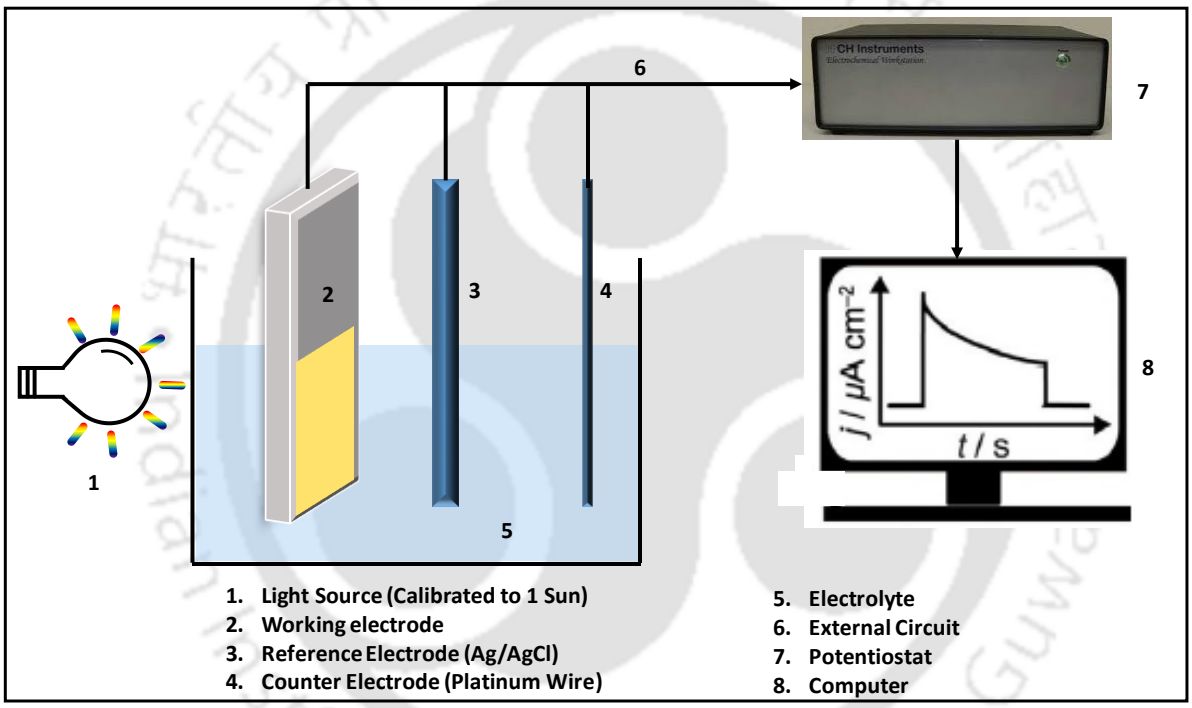

Figure 2.3: Schematic representation of the experimental setup for photoelectrochemical water oxidation.

The electrochemical characterisations were carried out at room temperature in a three electrode configuration in a CH1120B electrochemical workstation. A standard Ag/AgCl electrode and a platinum wire electrode are used as the reference and counter electrode, respectively. 0.5 M Na_2SO_4 aqueous solution is used as electrolyte for all the measurements (pH 6.8). Potential for the measurements are calibrated to the reversible H_2 electrode (RHE) according to the Nernst equation,

$$E_{RHE} = E_{Ag/AgCl} + 0.059 * pH + E^0_{Ag/AgCl}$$

Where E_{RHE} is the potential *vs.* RHE, $E_{Ag/AgCl}$ is the experimentally measured potential *vs.* Ag/AgCl, $E^0_{Ag/AgCl}$ is the standard potential of Ag/AgCl reference electrode against RHE (0.1976 V) and pH is the pH of the electrolyte. Polarization curves are obtained by linear sweep voltammetry (LSV) with a scan rate of 10 mV/s. The light response of the photocatalyst is measured by chronoamperometric curves measured at 0.7 V vs Ag/AgCl. The light source is a 300 W tungsten halogen lamp with the light intensity adjusted to 100 mW/cm^2. A schematic representation of the experimental setup for photocatalytic H_2 production is shown in **Figure 2.3**.

2.5 PHOTOCATALYTIC ACTIVITY EVALUATION

2.5.1 Apparent Quantum Yield

The performance of the photocatalysts were evaluated by measuring the Apparent Quantum Yield (AQY) of the photocatalysts according to the following equation:

$$AQY = \frac{\text{Number of reacted electrons}}{\text{Number of incident photons}} \times 100\%$$

$$= \frac{\text{Number of oxygen/hydrogen molecules produced in 1 hour}}{\text{Number of incident photons in 1 hour}} \times 100\%$$

Detailed calculation of AQY was carried out following Sasikala *et al.*[2] Total incident light intensity on the reactor was measured using an HTC LX101A lux meter. Considering the uniform intensity distribution of lamp, a correction for the difference in the area of the sensor of lux meter and the reactor surface area is evaluated. From the optical absorbance of all the photocatalysts, it is seen that all the photocatalysts absorb within the wavelength range of 200 – (200 + n) nm. Therefore, the fraction of light intensity only in this wavelength region (vary with different samples) is considered for quantum efficiency calculation. The emission profile of the lamp gives the incident light intensity in the range of 200 – 1100 nm. Now, the incident light intensity in the range of 200 – (200 + n) nm (E_m) was obtained by multiplying the total incident intensity with the ratio of the area in 200 – (200 + n) nm range to the total area of the emission profile. Thus, total incident light in 1 h in the wavelength range of 200 – (200 + n) nm (E_m) is given by

$$E_m = \frac{(\text{Total incident light intensity} \times \text{Area under the curve for the wavelength in the wavelength rangeof } 200-(200+n)\text{ nm})}{\text{Area under the curve for the entire emission profile}}$$

Since the light used was a polychromatic light, the energy of a single photon is considered as the weighted average energy (E_a) of all the photons in 200 – (200 + n) nm wavelength range. Now, the contribution of the photon of each wavelength λ_i (i from 200 – (200 + n)) towards the total energy can be calculated as

$$E_i = \frac{I_{\lambda_i}}{I_{total}} \times \frac{hc}{\lambda_i}$$

Where, $I_{\lambda i}$ is the intensity at wavelength λ_i and I_{total} is obtained from the lamp emission profile by adding the intensities of all photons in the wavelength range of 200 – (200 + n) nm. The weighted average energy of single photon (E_a) is calculated as

$$E_a = \sum_{\lambda=200}^{(200+n)} E_i(\lambda_i)$$

Total number of incident photons (N) in the wavelength range of 200 – (200 + n) nm is given by

$$N = \frac{E_m}{E_a}$$

$$\text{AQY}\ (\%) = \frac{2 \times \text{number of moles of } H_2 \text{ produced in 1 h} \times (6.023 \times 10^{23})}{\text{Total number of incident photons in 1 h (N)}} \times 100$$

2.5.2 Electrochemical Impedance (EIS) Spectra

Electrochemical impedance spectroscopy (EIS) is a widely used technique in order to study the kinetics of interfacial charge transfer at various interfaces in a photoelectrochemical device. EIS is a steady state method for measuring the current response to the modulation of a tiny ac voltage as a function of the angular frequency, ω. The impedance spectrum is measured in the frequency range of 0.1 Hz – 1 MHz and displayed in the Nyquist plot. Nyquist diagram shows real and imaginary part of impedance as displayed in **Figure 2.4 (A)**. The Nyquist plot typically features three semicircles, one at the low frequency region is attributed

to the Nernst diffusion within the electrolyte (Z_3), semicircle in the mid–frequency region corresponds to electron transfer at the semiconductor electrolyte interface (Z_2) and the smaller semicircle at the higher frequency region is attributed to the redox reaction at the platinum counter electrode/electrolyte interface (Z_1) (**Figure 2.4 (A)**).[3] R_h (or R_s) corresponds to the sheet resistance of FTO substrate in the high frequency region in the range of 10^6 Hz. **Figure 2.4 (B)** schematically represents a PEC cell with the various processes of charge transfer. The spectroscopic scan over the relevant window of frequencies is resolved into a combination of resistances and capacitors in a given arrangement by fitting it into an equivalent circuit (EC), which is a useful tool for the interpretation of experimental results.[4] For the interpretation of EIS, a classical physical model of a semiconductor–electrolyte junction is adopted to depict the charge carrier dynamics which shows the generation of photogenerated charge carriers on light absorption (G), along with the different surface state trapping, and interfacial charge-transfer reactions at the semiconductor–electrolyte junction (**Figure 2.4 (C)**). Based on the different processes as shown in **Figure 2.4 (C)**, an equivalent circuit (EC) model is depicted in **Figure 2.4 (D)** to interpret the EIS data. The model presents the central role of a surface state acting as a recombination centre, providing a resistance as given by $R_{trapping}$. Surface states can also affect the charge transfer of holes to the donor species in solution, as described by $R_{ct,trap}$. The crucial element for the analysis of EIS are the capacitances and their combination in the EC. There are two capacitances — capacitance of the bulk, C_{bulk} and capacitance of the surface states of the semiconductor, C_{trap} which are included in the EC model.[4]

In **Chapter 5**, electrochemical impedance spectra (EIS) was measured using an electrochemical work station (Model CHI760D, Inc., Austin, TX) in 0.5 M Na_2SO_4 aqueous solution in a frequency range of 100,000 Hz to 0.1 Hz with an amplitude of 10 mV.

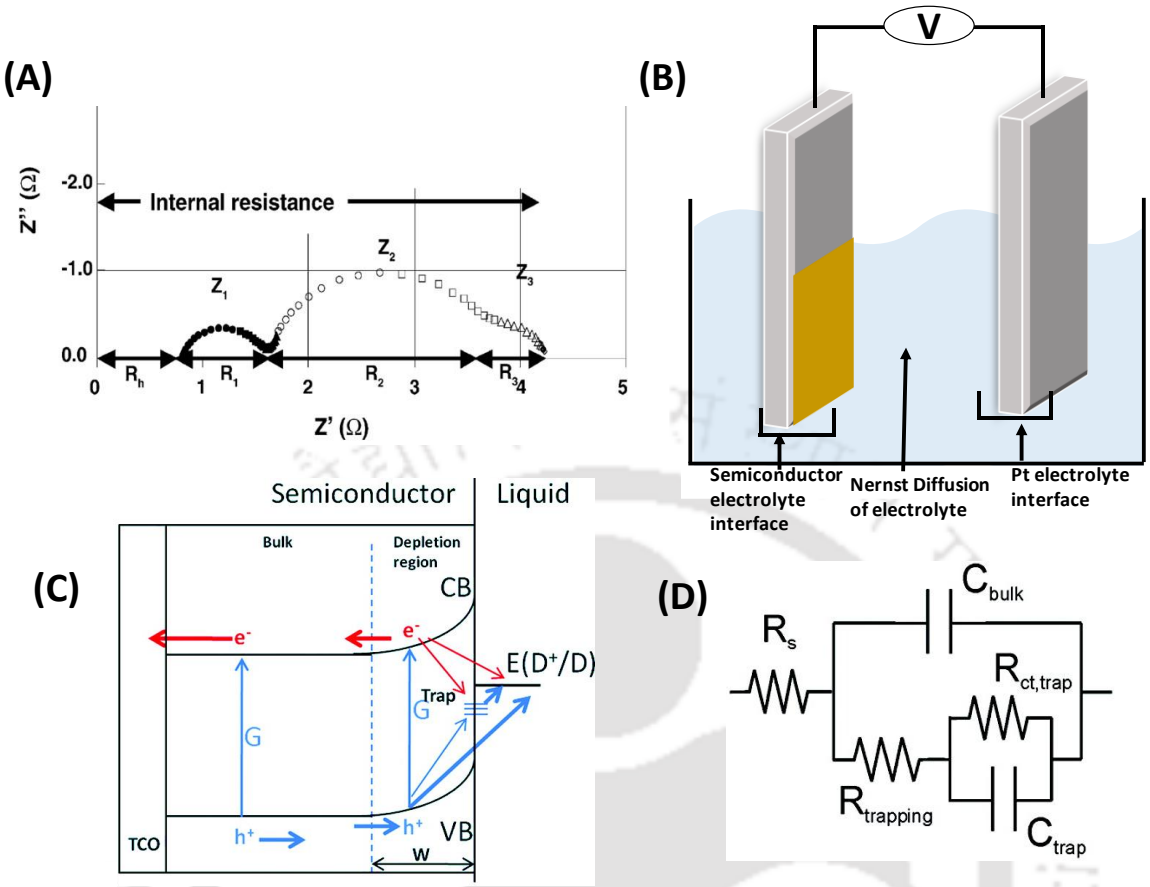

Figure 2.4: (A) A typical Nyquist plot. The three semicircles are assigned to the impedance related to the charge transport at Pt electrolyte interface (Z_1), semiconductor electrolyte interface (Z_2) and Nernst diffusion of ions within the electrolyte (Z_3), R_1, R_2 and R_3 are described as the real parts of Z_1, Z_2 and Z_3, respectively. R_h is defined as the sheet resistance in the high-frequency range over 10^6 Hz (Taken from Ref. 5), (B) Schematic representation of the experimental setup for photoelectrochemical water oxidation with the different interfaces of charge transfer, (C) A proposed physical model of a semiconductor–electrolyte junction (Taken from Ref. 4) and (D) Equivalent circuit used to interpret the electrochemical impedance data. (Taken from Ref. 4)

A fundamental property of any semiconductor–electrolyte system is its flat-band potential (V_{FB}) which is defined as the applied voltage such that there is no band bending or charge depletion at the semiconductor–electrolyte interface.[6] Many important parameters like the dopant type (n-type or p-type), donor density (N in the equation., N_A for p-type, and N_D for n-type) and flat-band potential (V_{FB}) can be determined by conducting analysis of the

applied potential (E) in relation to interfacial capacitance (C_{sc}) as described by Mott–Schottky equation,[7]

$$\frac{1}{C_{SC^2}} = \frac{1}{N_{e\varepsilon\varepsilon_0}}[E - E_{FB} - \frac{kT}{e}]$$

where C_{sc} is the interfacial capacitance of the semiconductor, N is the charge carrier density, e is the fundamental charge constant, ε_0 is the permittivity of vacuum, ε is relative permittivity of the semiconductor, E is applied potential, k is the Boltzmann constant, and T is the temperature. A plot of $1/C^2$ against V, yield a straight line from which V_{FB} can be determined from the intercept on the X–axis. The value of N can be determined from the slope knowing ε and A as shown in **Figure 2.5**.

In our experiments in **Chapter 5**, Mott–Schottky curves were obtained in a potential range from 0 to 1.5 V vs. Ag/AgCl at a frequency of 1000 Hz under dark condition.

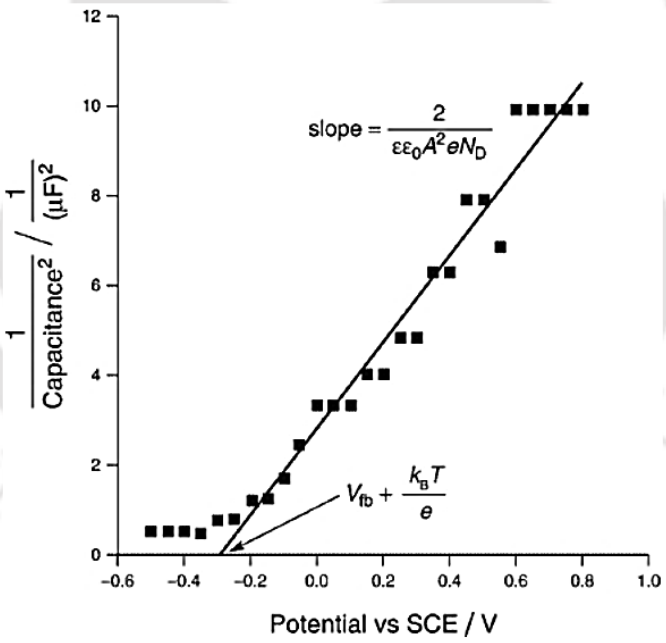

Figure 2.5: A typical Mott–Schottky plot. (Taken from Ref. 6)

2.5.3 Faradaic Efficiency

In order to evaluate the PEC activity of the catalysts, Faradaic efficiency was measured, which gives the effective utilisation of charges to generate the target products of H_2 or O_2 gas.[8] Determination of Faradaic efficiency is the most useful method to verify that

the generated photocurrent is in fact due to water splitting and not photocorrosion of the electrodes or other side reactions. It is defined as the ratio of the actual evolved gas divided by the theoretically evolved gas based on the measured photocurrent.[9]

$$\text{Faradaic Efficiency} = \frac{\text{Experimental Gas Evolution}}{\text{Theoritical Gas Evolution}}$$

$$= \frac{\text{Measured Oxygen Evolution}}{\text{Gas Evolution Based on Photocurrent}}$$

$$= \frac{\text{Oxygen Evolution Measured}}{((\frac{J_{photo} * A * t}{e})/4)/N_A} * 100\%$$

Where J_{photo} is the photocurrent density (A cm^{-2}) generated during the measurement time t (seconds); A is the illumination area of the photoelectrode (cm^2); e is the charge of an electron (1.602×10^{-19} C) and N_A is the Avogadro's number (6.022×10^{23} mol^{-1}).

2.6 REFERENCES

1. L. Karimi, S. Zohoori and M. E. Yazdanshenas, *J. Saudi Chem. Soc*., 2014, **18**, 581.
2. R. Sasikala, V. Sudarsan, C. Sudakar, R. Naik, T. Sakuntala and S. R. Bharadwaj, *Int. J. Hydrogen Energy*, 2008, **33**, 4966.
3. S. Phadke, A. D. Pasquier and D. P. Birnie, *J. Phys. Chem. C*, 2011, **115**, 18342.
4. B. Klahr, S. Gimenez, F. F. -Santiago, T. Hamann and J. Bisquert, *J. Am. Chem. Soc*., 2012, **134**, 4294.
5. N. Koide, A. Islam, Y. Chiba and L. Han, *J. Photochem. Photobiol., A*, 2006, **182**, 296.
6. K. Gelderman, L. Lee and S. W. Donne, *J. Chem. Educ.*, 2007, **84**, 685.
7. J. Cen, Q. Wu, M. Liu and A. Orlov, *Green Energy & Environment*, 2017, **2**, 100.
8. D. Li, J. Shi and C. Li, *Small*, 2018, **14**, 1704179.
9. C. Jiang, S. J. A. Moniz, A. Wang, T. Zhang and J. Tang, *Chem. Soc. Rev.,* 2017, **46**, 4645.

Chapter 3

Quaternary Semiconductor Cu_2ZnSnS_4 Loaded with MoS_2 as a Co-catalyst for Enhanced Photocatalytic Activity

This chapter explains the utilisation of quaternary Cu_2ZnSnS_4 and its composite with a co–catalyst, MoS_2 for photocatalytic water reduction and Rhodamine B dye degradation. The hydrogen evolution activity of Cu_2ZnSnS_4–MoS_2 is ~20% higher than bare Cu_2ZnSnS_4 with an AQY value of 22.67%. The dye degradation activity of the composite is almost twice that of the bare counterpart. The faster photo degradation of Rhodamine B by Cu_2ZnSnS_4–MoS_2 in comparison to Cu_2ZnSnS_4 is substantiated by kinetic studies. Various scavenger tests are performed to determine the role of the intermediates in the photo degradation of Rhodamine B.

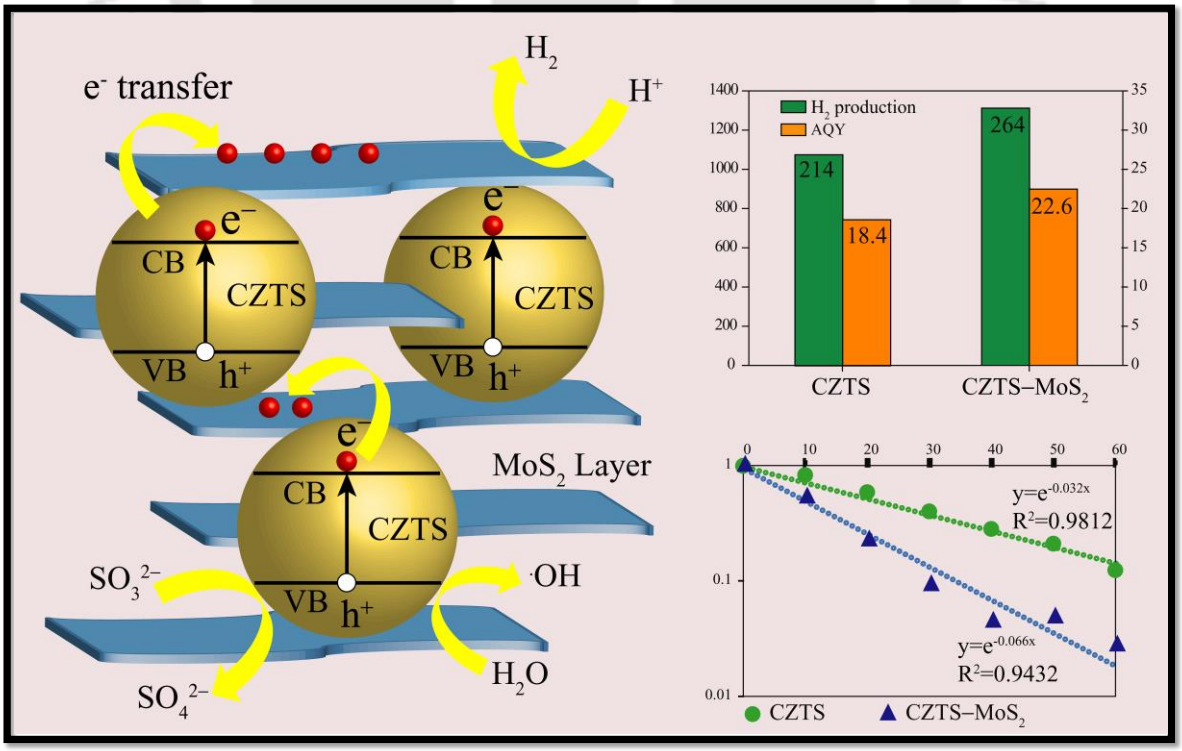

RSC Adv., 2015, **5**, 40475.

3.1 INTRODUCTION

Over the last few decades several sulfide-based polynary alloy semiconductors have been explored and they proved as ideal photo-absorbers because of their tunable electronic and optical properties.[1-3] Compared to binary materials, polynary alloy semiconductor nano–materials are able to produce new properties as they could inherent the properties from their parent binary materials.[4] For example, several Cu–chalcopyrite p–type semiconductors namely $Cu(In,Ga)Se_2$,[5] $CuGa_3S_5$,[6] $CuGa_3Se_5$,[7,8] $CuInS_2$,[9,10] $Cu(In,Ga)S_2$,[11] $(CuIn)_xZn_{2(1-x)}S_2$[10] $CuGaSe_2$,[12] owing to their high absorption coefficients, tunable band gap values (1.0 – 2.4 eV) and suitable band alignment for water reduction, are used for H_2 production from water. However, the scarcity and higher cost of In, Ga has led to the search of alternative photo-catalytic systems from earth abundant elements such as Copper, Zinc etc.[13] Cu_2ZnSnS_4 (CZTS), a non-toxic compound with abundantly available constituent elements (Cu: 50 ppm, Zn: 75 ppm, Sn: 2.2 ppm, S: 260 ppm)[14] has recently attracted much interest. CZTS has a near-optimum direct band gap energy of 1.4 – 11.6eV and a large absorption coefficient ($>10^4$ cm^{-1}). Being environment friendly and of natural abundance, CZTS is finding its place in replacing highly efficient materials like $Cu(InGa)Se_2$. Although, more emphasis is on fabricating photovoltaic solar cell devices of CZTS,[15-18] yet its photocatalytic activity for waste water treatment,[19] photoelectrochemical devices[20] and water oxidation for H_2 generation are also being explored.[21] The photocatalytic efficiency of semiconductor materials is further enhanced by coupling them with either noble metals e.g. Au, Pt,[19] which act as co–catalyst, or making composite with material having large specific surface area and good electrical conductivity, namely graphene oxide.[22] MoS_2 being a layered material with a large surface area,[23] is of interest as an alternative co–catalyst to the high cost noble metals. MoS_2 has shown high efficiencies when coupled with materials like TiO_2, CdS etc.[24-27] which are studied for their photocatalytic and solar water oxidation activity. Owing to their outstanding properties, we have studied CZTS and MoS_2 as possible candidates to replace noble and other expensive elements for their photocatalytic activity using CZTS as a photocatalyst with MoS_2 as a co–catalyst. The water oxidation efficiency of CZTS–MoS_2 was observed to be nearly 20% higher than CZTS owing to a lesser recombination rate of photogenerated electrons and holes as evident from the photoluminescence quenching in the CZTS–MoS_2 composite. The photocatalytic degradation of a representative dye viz. Rhodamine B (RhB) was studied for the photocatalytic activity of CZTS–MoS_2 composite;

which shows a higher activity compared to bare CZTS. Various scavenger tests established that hydroxyl radical ($OH^{\bullet}$) plays a major role as the reactive intermediate species participating in dye degradation.

3.2 EXPERIMENTAL SECTION

3.2.1 Preparation of CZTS

The synthesis of CZTS was adopted from a previously reported method.[14] In a typical procedure, copper(II) acetate monohydrate ($Cu(CO_2CH_3)_2.H_2O$) (0.04 M, 0.119 g), zinc(II) nitrate hexahydrate ($Zn(NO_3)_2.6H_2O$) (0.02 M, 0.089 g), and tin(II) chloride dehydrate ($SnCl_2.2H_2O$) (0.02 M, 0.067 g) were dissolved in 15 mL of a solvent mixture of ethylenediamine (EN) ($C_2H_4(NH_2)_2$) and deionised water (volume ratio 1 : 9), wherein EN acts as a chelating agent and stabilizer. 15 mL of thiourea ($SC(NH_2)_2$) (0.16 M, 0.182 g) was added drop–wise to the above solution. Precursors solution was then transferred into a 50 mL Teflon–lined stainless steel autoclave, sealed and heated at 180 ºC for 24 h. Liu *et al.* have proposed that this process involves, the reduction of Cu^{2+} ions to Cu^{+} and oxidation of Sn^{2+} ions to Sn^{4+} through the oxidation-reduction reactions.[20] After cooling, the powders were centrifuged, washed several times with deionised water and absolute ethanol and dried at 60 ºC overnight.

3.2.2 Preparation of MoS_2

MoS_2 catalysts were synthesized by a hydrothermal method[28] involving ammonium heptamolybdate ($(NH_4)_6Mo_7O_{24}.4H_2O$) (0.007 M, 0.276 g) and thiourea (CH_4N_2S) (0.15M, 0.36 g), dissolved in 30 mL distilled water. A surfactant cetyltrimethylammonium bromide (CTAB) ($C_{19}H_{42}BrN$), (0.003M, 0.036 g), was added into the above solution. Resultant mixture was added to a 50 mL Teflon-lined stainless steel autoclave and kept at 180 ºC for 24 h. After cooling, catalyst was separated, washed with distilled water and absolute ethanol several times to remove the residual water and water–soluble impurities. Finally, the resulting product was dried at 50 °C for 8 h.

3.2.3 Preparation of CZTS–MoS_2

For the preparation of CZTS–MoS_2 composite, 1wt.% of MoS_2 was added into the above precursor solution of CZTS and transferred to a Teflon-lined stainless steel autoclave, sealed and heated at 180 ºC for 24 h. Resulting powder, after cooling, was washed with water and ethanol several times and dried at 60 °C overnight.

3.3 RESULTS AND DISCUSSION

3.3.1 Powder X-ray Diffraction (PXRD) Patterns

The PXRD patterns of as–prepared CZTS, MoS_2 and the composite CZTS–MoS_2 are shown in **Figure 3.1**. As-prepared CZTS is found to be crystallizing in tetragonal kesterite phase (JCPDS card No. 26-0575) as identified by diffraction peaks at 2θ = 28.5° (112), 33.3°(200), 47.4° (220), 56.1° (312), 69.2° (008), and 76.5° (332).[29] No impurity peaks corresponding to ZnS or Cu_2SnS_3 phases is observed which confirms the purity of the phase.

MoS_2 is weakly crystalline, as seen from the broadening of diffraction peaks. The PXRD pattern matches well with the hexagonal structure (JCPDS card No. 37-1592) with diffraction peaks observed at 2θ = 16.7°, 33.4°, 43.5°, and 57.4° corresponding to (002), (100), (103) and (110) hkl planes, respectively.

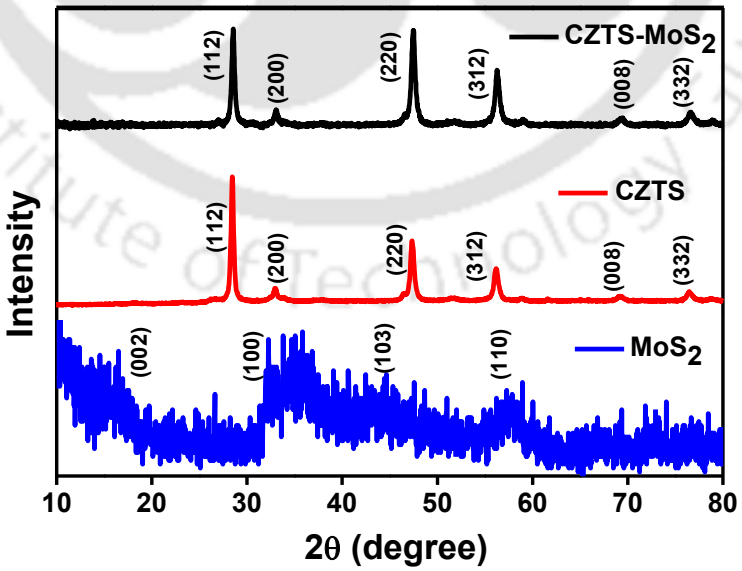

Figure 3.1: Powder X-ray diffraction pattern for as-synthesized CZTS, MoS_2 and CZTS–MoS_2.

The composite CZTS–MoS_2 shows the PXRD pattern of CZTS only, while no distinct peak corresponding to MoS_2 is observed. The absence of MoS_2 peaks could be attributed to the weak crystalline nature of MoS_2 compared to CZTS as well as the low content of MoS_2 loading in the CZTS–MoS_2 composite.

3.3.2 Field-Emission Scanning Electron Microscopy

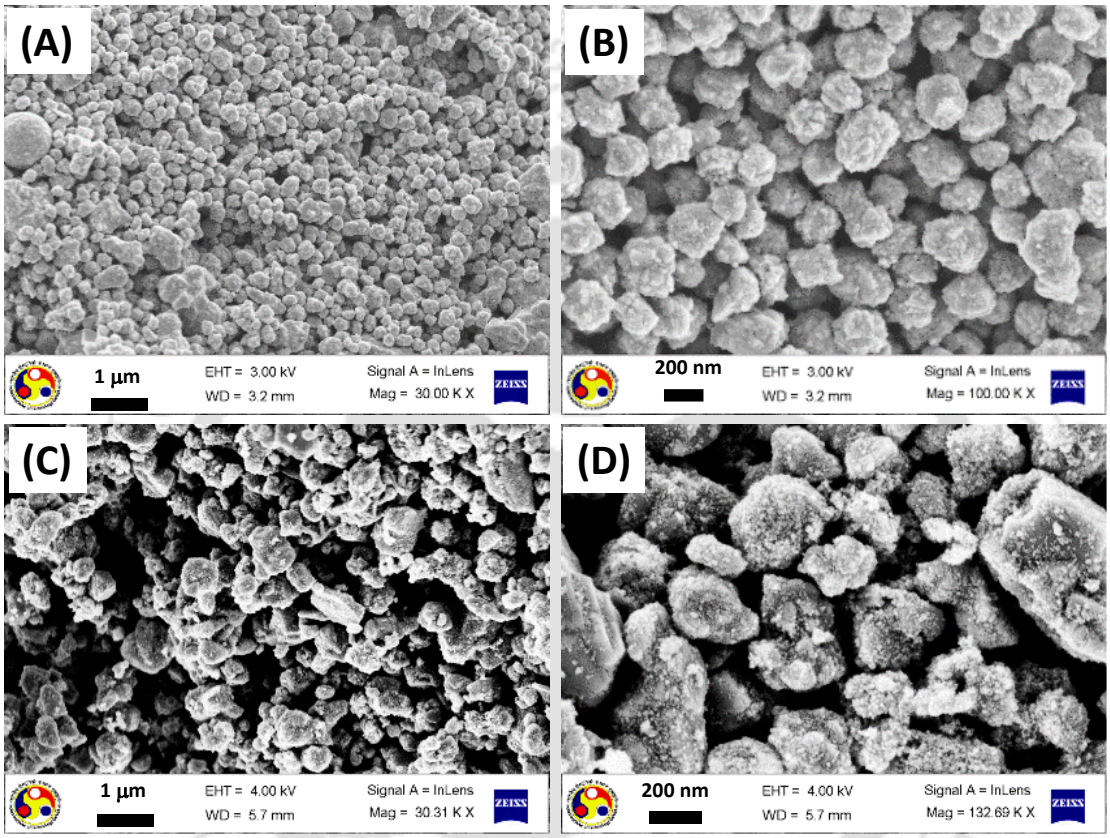

Figure 3.2: Field-emission scanning electron microscopy (FESEM) images of (A, B) CZTS and (C, D) CZTS–MoS_2.

The morphological features of CZTS and its composite with MoS_2 are studied by FESEM. **Figure 3.2 (A, B)** corresponds to CZTS which shows nearly spherical particles of uniform size distribution. The average particle size is observed to be in the range of ~ 200 nm, The FESEM images of CZTS–MoS_2 as shown in **Figure 3.2 (C, D)** are bigger than CZTS with more aggregation and irregular morphology. This might be probably due to aggregation of CZTS with MoS_2. In order to ascertain the distribution of MoS_2 in CZTS–MoS_2, the elemental mapping of the composite was recorded by energy dispersive X-ray analysis as shown in **Figure 3.3 (A)**. The elemental mapping proves the homogeneous distribution of all

the constituent elements (**Figure 3.3 (B–F)**) in the composite CZTS–MoS_2, in the scan area **Figure 3.3 (A)**.

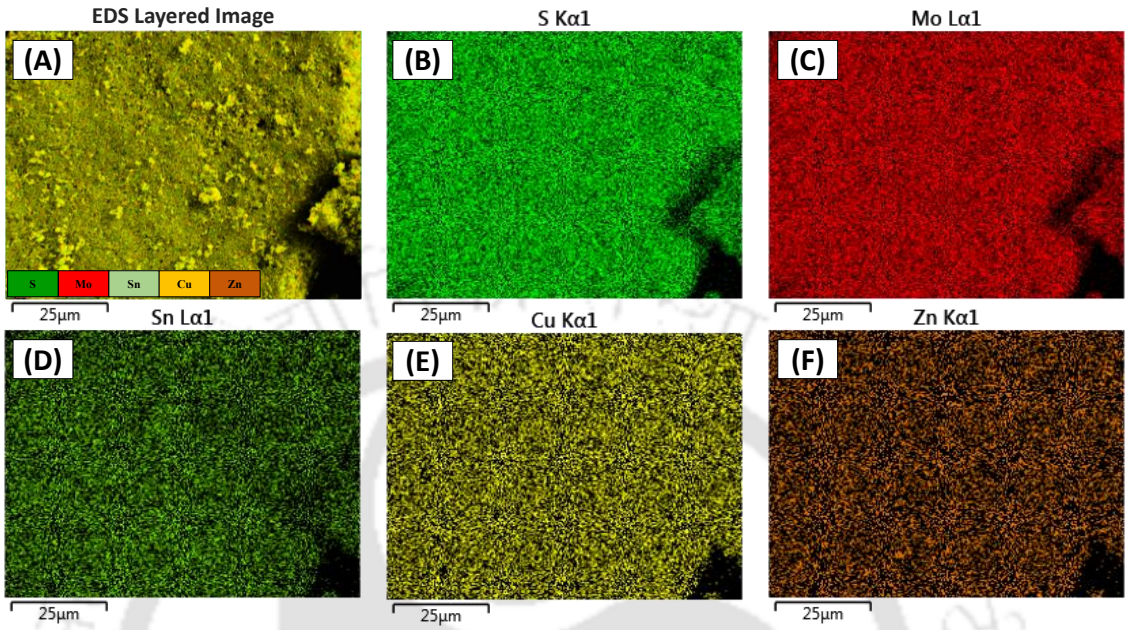

Figure 3.3: (A) Energy-dispersive X-ray (EDX) mapping of CZTS–MoS_2. Homogeneous elemental distribution of (B) S, (C) Mo, (D) Sn, (E) Cu and (F) Zn in the area (A)

3.3.3 Transmission Electron Microscopy

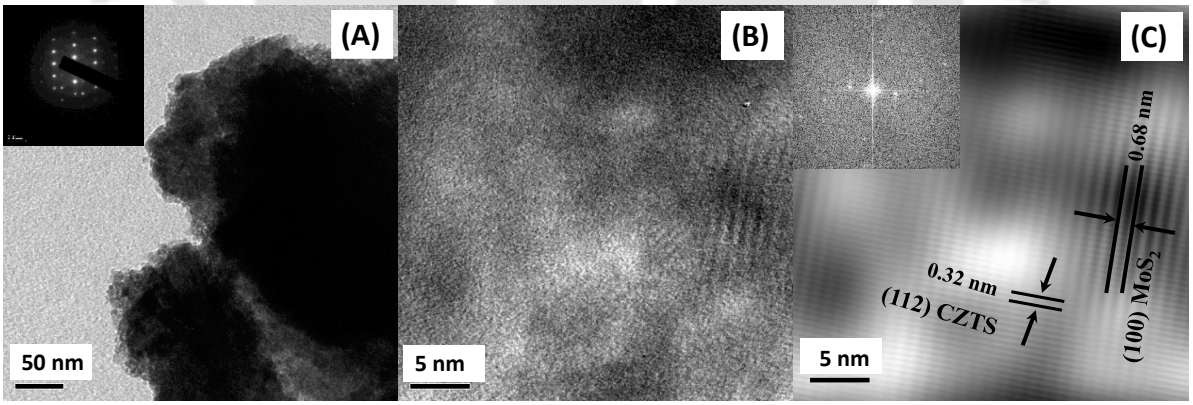

Figure 3.4: (A) Transmission electron microscopy (TEM) image of CZTS–MoS_2, inset to (A) shows the selected area electron diffraction (SAED) pattern, (B) high resolution transmission electron microscopy (HRTEM) image of CZTS–MoS_2 (C) HRTEM showing lattice patterns of CZTS and MoS_2. Inset of (C) shows the fast Fourier transform of the HRTEM image.

For the microstructural analysis of CZTS–MoS_2, transmission electron microscopy (TEM) and high resolution transmission electron microscopy (HRTEM) were performed. From **Figure 3.4 (A)**, irregular morphology of the composite is observed in accordance with the FESEM image. **Figure 3.4 (B)** shows the HRTEM image. In **Figure 3.4 (C)**, an inter–planar spacing of 0.68 nm is observed which corresponds to MoS_2 (100) and an inter–planar distance of 0.32 nm corresponding to CZTS (112) are observed. This observation substantiates successful interaction of MoS_2 and CZTS in the composite.

3.3.4 Ultraviolet-Visible Diffuse Reflectance Spectra and Band Gap Calculation

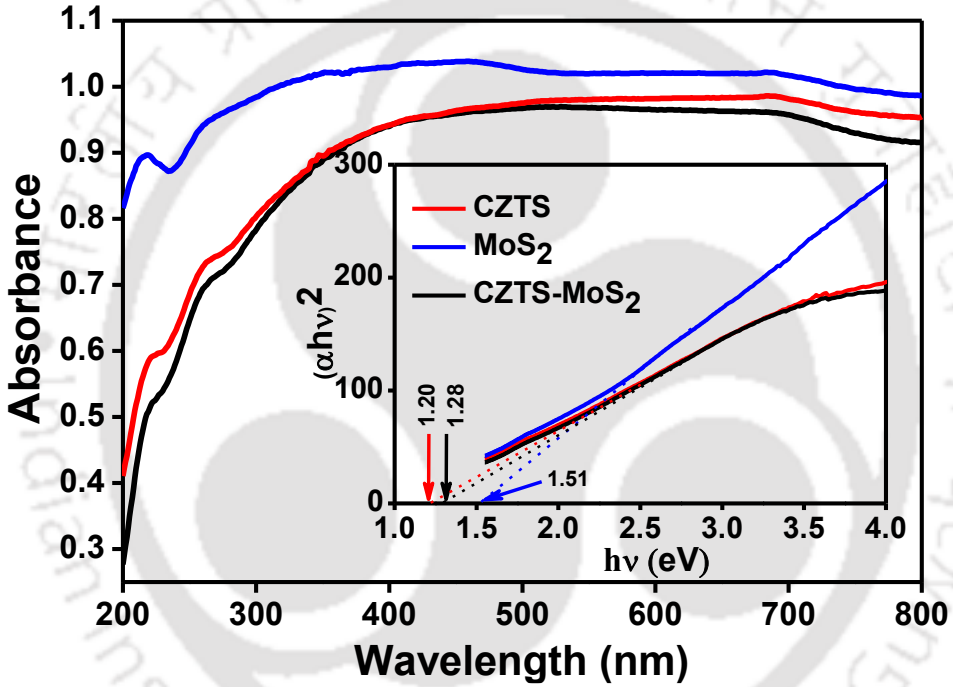

Figure 3.5: UV-visible diffuse reflectance spectra of CZTS, MoS_2 and CZTS–MoS_2. The inset shows the Tauc's plot to evaluate the optical band gap values for the three compounds.

UV-visible diffuse reflectance spectra of as-prepared CZTS, MoS_2 and their composite are shown in **Figure 3.5**. The absorbance profile of all the samples range in a wide range of spectrum covering the whole visible region. There is not much variation in the absorbance profile of the samples. Inset to **Figure 3.5** shows Tauc plot to calculate the optical band gap of the material. The Tauc plot is plotted between $(\alpha h\nu)^2$ (on Y–axis) and photon energy ($h\nu$) (on X–axis) which is related by the equation,

$$(\alpha h\nu)^{\frac{1}{n}} = C * (h\nu - E_g)$$

Where α is the absorption coefficient of the semiconductor at a certain value of wavelength λ , h is the Plank's constant, C is the proportionality constant, ν is the frequency of light, E_g is the band gap energy and n = ½ for direct transition mode materials, respectively.

The absorption coefficient is estimated from the equation,

$$\alpha = \frac{1}{t} * \ln\left(\frac{I_t}{I_0}\right) = \frac{1}{t} * A * \log e$$

Where A, t, I_t and I_0 represent the absorbance, thickness of the photocatalyst, intensity of transmitted light and intensity of incident light, respectively. The band gap energies are estimated by linear extrapolation to X–axis and the band gap values for CZTS, MoS_2 and CZTS–MoS_2 are determined to be 1.20, 1.51, and 1.28 eV, respectively.

3.3.5 Raman Spectral Analysis

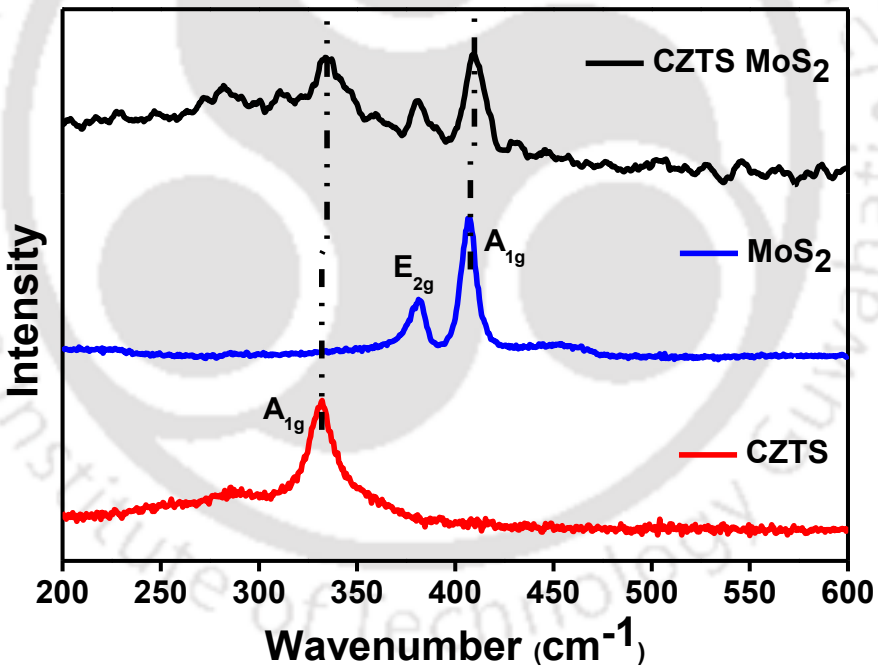

Figure 3.6: Raman spectra of CZTS, MoS_2 and CZTS–MoS_2.

Raman spectral analysis were carried out in order to characterise the structural bonding of the compounds and are shown in **Figure 3.6**. CZTS has a characteristic peak at 337 cm^{-1}, corresponding to single-phase CZTS.[30] This strong Raman peak is attributed to A_{1g} symmetry which is due to the vibration of the sulfur atom. Small peaks at ~ 288 cm^{-1} also correspond to CZTS.[31] It is a strong evidence of the presence of single-phase CZTS with the

kesterite structure.[32] In the Raman spectra of MoS_2, characteristic peaks at 380 and 407 cm^{-1} are observed which are assigned to the E^1_{2g} and A_{1g} modes of MoS_2, respectively. The E^1_{2g} mode is correlated with an in-plane motion of Mo and S atoms, while the A_{1g} mode is caused by an out-of-plane vibration of Mo and S.[33] In the Raman spectra of the composite CZTS–MoS_2, peaks of both CZTS and MoS_2 are observed with a slight shift towards higher wavenumber which implies interaction among the components in the composite.

3.3.6 BET Surface Area Analysis

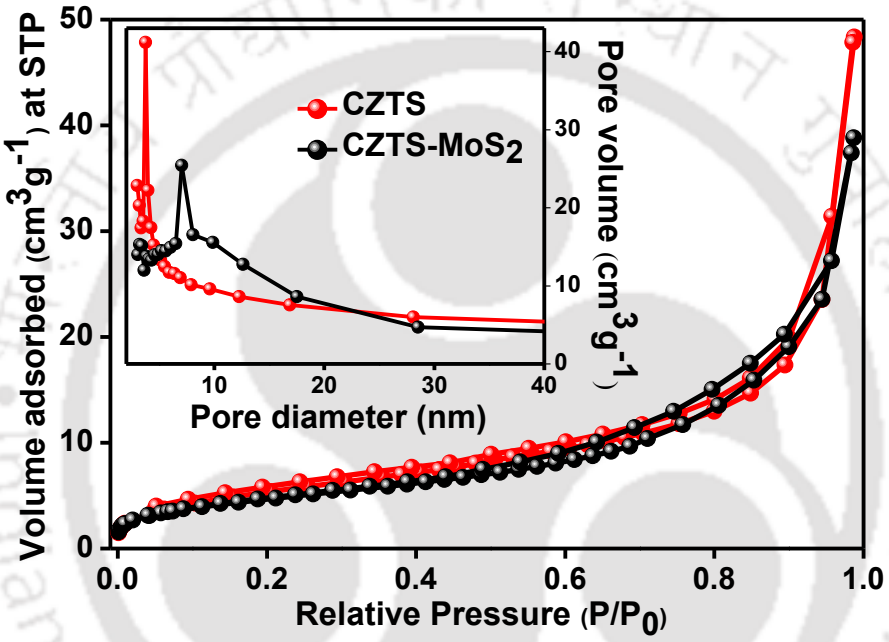

Figure 3.7: BET surface area analysis of CZTS and CZTS–MoS_2. Inset depicts Barrett–Joyner–Halenda pore size distribution curves for both the samples.

Figure 3.7 shows N_2 adsorption-desorption isotherm and corresponding pore size distribution curve (inset) for CZTS and CZTS–MoS_2. According to the Brunauer-Deming-Deming-Teller (BDDT) classification, the majority of physisorption isotherms can be grouped into six types. The shapes of hysteresis loops are often used to identify the specific pore structure.[20] Both the samples display a typical type-IV isotherms and type H3 hysteresis loops. Type IV isotherms are generally shown by mesoporous adsorbents.[34] The observed BET surface area of CZTS and CZTS–MoS_2 are 20.10, and 17.17 m^2/g, respectively. The Barrett–Joyner–Halenda (BJH) pore size distribution curve (inset) indicates a high degree of uniformity of pores in the range of ~ 3 nm for CZTS and ~ 7 nm for CZTS–MoS_2. Although the surface area for both samples are comparable, yet larger pore diameter in CZTS–MoS_2

suggests more effective active sites in the composite leading to enhanced photocatalytic efficiency.

3.3.7 Steady-State Photoluminescence Spectra

In order to access the charge transfer behavior, steady-state photoluminescence was carried out for CZTS and CZTS–MoS_2. On excitation at 580 nm, both the compounds emit at ~ 760 nm (**Figure 3.8**). From **Figure 3.8**, it is observed that the emission intensity of the composite, CZTS–MoS_2 is quenched (by ~ 11%), suggesting a decrease in recombination rate of photogenerated charge carriers in the composite. This observation might explain the increased charge separation in the composite owing to the favorable band alignments of CZTS and MoS_2.

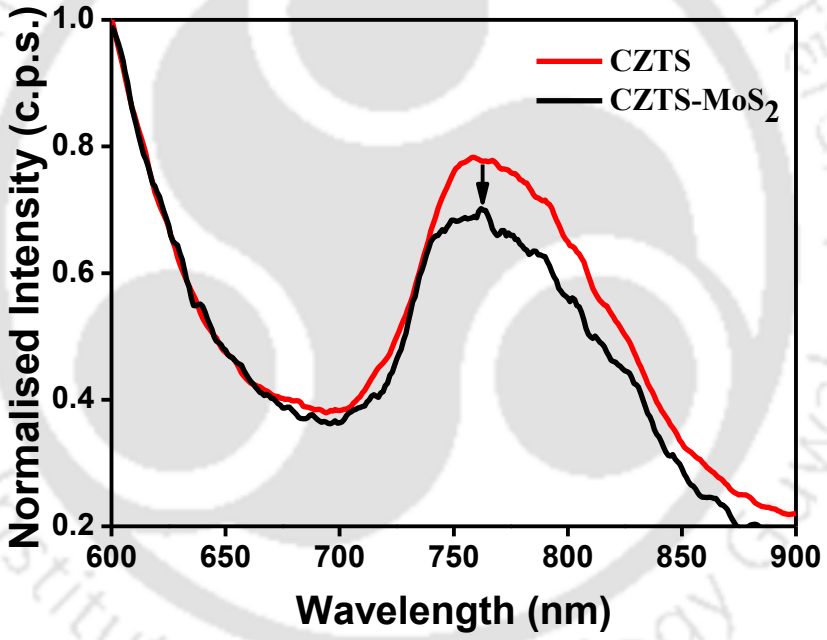

Figure 3.8: Steady-state photoluminescence spectra of CZTS and CZTS–MoS_2.

3.3.8 Photocatalytic Hydrogen Production

Photocatalytic water oxidation experiment was carried out using CZTS and CZTS–MoS_2 as the photocatalyst and the amount of H_2 liberated were estimated. The H_2 evolution rates under visible irradiation are shown in **Figure 3.9**. The CZTS–MoS_2 composite showed a higher photocatalytic activity with the H_2 production rate of 264 µmol/0.2g/h in comparison to bare CZTS (214 µmol/0.2g/h). The calculated AQY of CZTS–MoS_2 is 22.67% which is about 1.23 times higher than that of CZTS i.e. 18.42%.

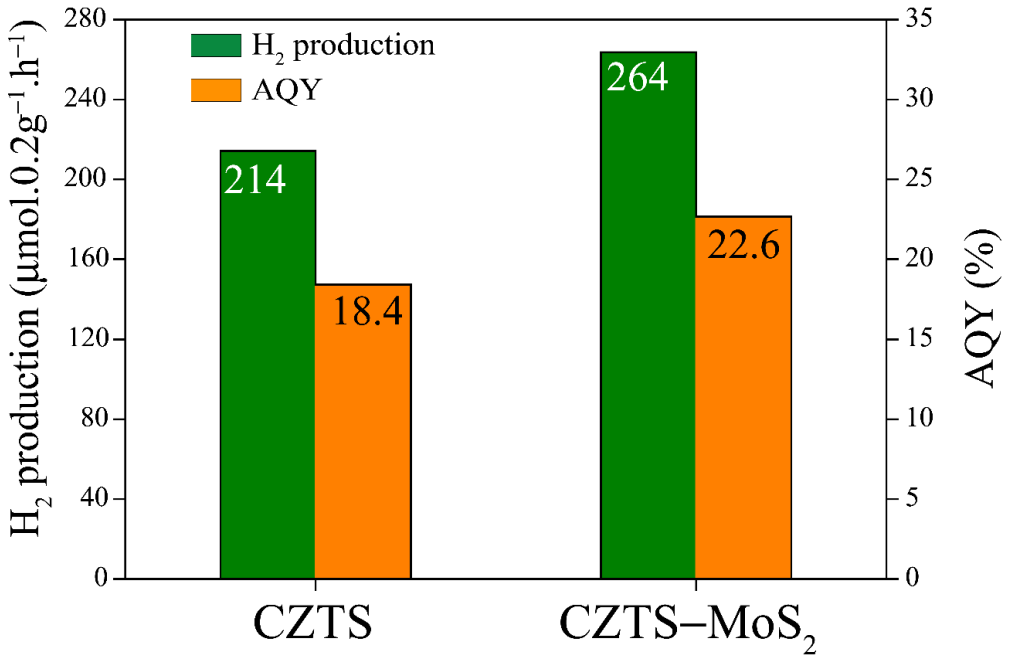

Figure 3.9: Amount of H_2 generated from CZTS and CZTS–MoS_2 catalyst under light irradiation and their respective AQY (%) values.

The higher photocatalytic activity in the composite is attributed to more active sites in CZTS–MoS_2 as well as higher charge separation. A schematic of the band diagram showing energy alignments of CZTS–MoS_2 which facilitates an efficient transfer of electrons is shown in **Figure 3.10**. Upon light irradiation on CZTS–MoS_2, electron-hole pair is generated in the conduction band and valence band of CZTS, respectively. The sacrificial electron donor (Na_2S/Na_2SO_3) rapidly consumes the oxidative holes in the valence band of CZTS, leaving the reductive electrons efficiently separated in the conduction band. At the same time, the reductive electrons are transferred from the conduction band of CZTS to the conduction band of MoS_2 because of the close proximity alignment of the conduction bands of the two, thereby leading to the reduction in the rate of electron–hole pair recombination and hence enhanced charge separation. The pool of reductive electrons thus generated in the conduction band of MoS_2 promotes the reduction of H^+ ions, thereby producing H_2 gas. Thus, improved photo-catalytic activity of CZTS–MoS_2 is attributed to the efficient separation and lesser recombination of photo-generated electron–hole pairs in the composite.

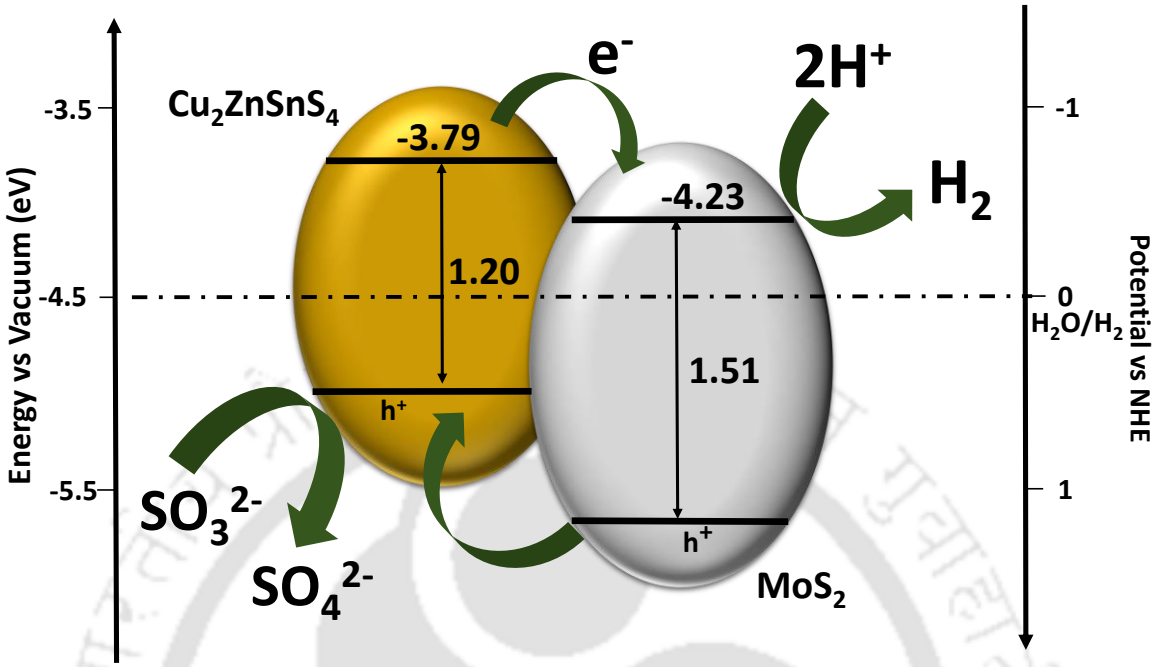

Figure 3.10: Band alignment and probable charge transfer pathways in CZTS–MoS_2.

3.3.9 Reusability of CZTS–MoS_2

In order to examine the reusability of the CZTS–MoS_2 catalyst, we have carried out three cycles of the photocatalytic experiment of H_2 production, with the catalyst. The catalyst retained optimal activity till three cycles, which shows the efficient reusability of the catalyst. The result of the repeated cycles is shown in **Figure 3.11**. In a typical experiment 0.2 g of sample was dispersed in 25 mL of water containing Na_2SO_3 (0.25 M) and Na_2S (0.35 M) as sacrificial reagents. Solution containing the photocatalyst was degassed for 30 min and then irradiated with UV–Vis light while stirring, to ensure uniform exposure of the suspension throughout the process. The produced gas was analysed by gas chromatography (Nucon 5765), using a thermal conductivity detector (TCD), after passing through moisture and oxygen traps. After irradiation of one hour, the solution was removed and the same experiment was repeated with fresh solution without any processing of the catalyst and the amount of gas evolved per 10 min was measured. Similarly, the experiment was repeated for a third cycle.

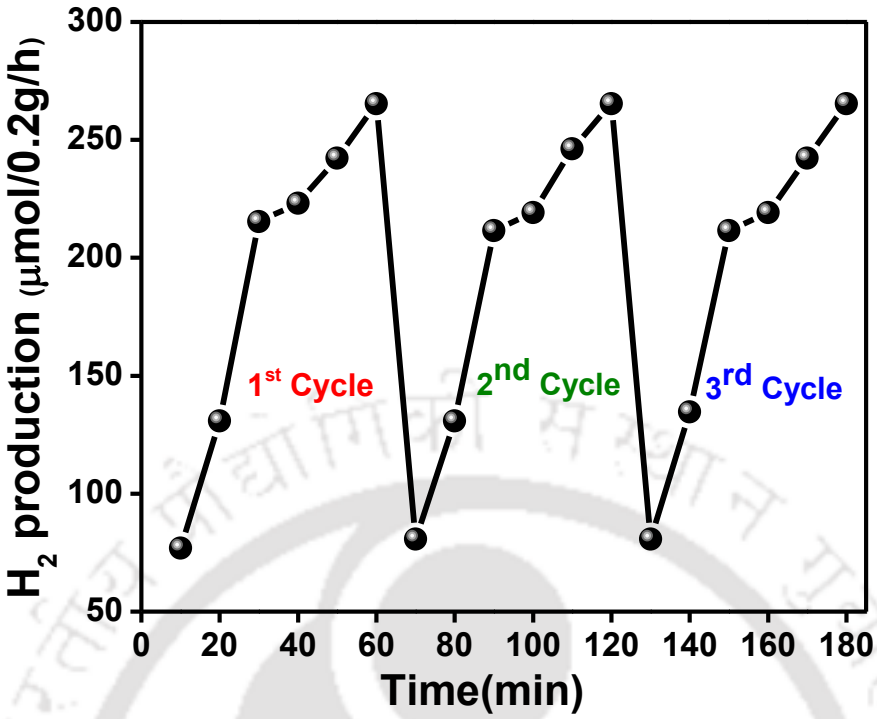

Figure 3.11: Amount of H_2 generated by CZTS–MoS_2 catalyst after repeated cycles.

3.3.10 Photocatalytic Dye Degradation Analysis

The catalysts also proved to be efficient in degradation of an industrial pollutant–dye. The photocatalytic dye degradation ability of the compounds were studied by taking Rhodamine B (RhB) (10^{-5} M) as a reference dye. The photodegradation of RhB dye was followed by measuring its concentration at absorbance value of 552 nm. The absorbance spectra of RhB dye was collected at a regular interval (10 min up to 1 h) during the degradation experiments, as shown in **Figure 3.12 (A)** and **Figure 3.12 (B)** using CZTS and CZTS–MoS_2, respectively. The concentration (C/C_0) versus time is plotted as shown in **Figure 3.12 (C)**. From **Figure 3.12 (C)**, it is clearly observed that RhB dye is degraded much faster by CZTS–MoS_2 than bare CZTS. ~ 97% degradation of RhB dye was achieved in case of CZTS–MoS_2 in about 40 min whereas it was only ~ 70% for bare CZTS. **Figure 3.12 (D)** shows the first order linear transform, $\ln(C/C_0) = -k_{app}t$ corresponding to the photo-degradation of RhB dye by CZTS and CZTS–MoS_2. Here, k_{app} is the apparent first order reaction rate constant which represents the rate of the reaction. From the first order linear fit in **Figure 3.12 (D)**, it is observed that CZTS–MoS_2 composite shows higher activity with an apparent rate constant almost twice (0.066 min^{-1}) than that of CZTS (0.032 min^{-1}).

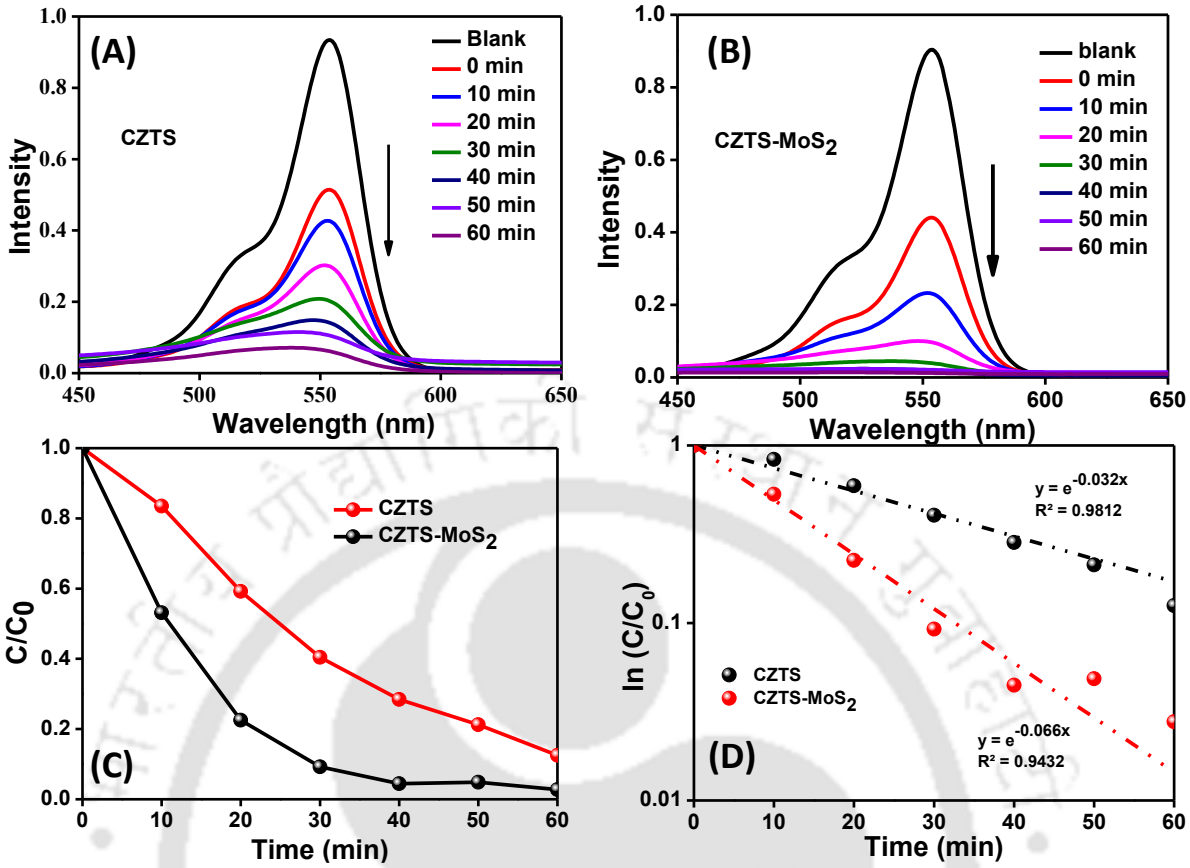

Figure 3.12: (A) UV-visible absorption spectra of RhB dye degradation with CZTS catalyst in 1 h at an interval of 10 min, (B) UV-visible absorption spectra of RhB dye degradation with CZTS–MoS_2 catalyst in 1 h at an interval of 10 min, (C) C/C_0 versus time (min) plot of photodegradation of RhB dye by CZTS and CZTS–MoS_2 and (D) apparent rate constant of RhB dye degardation in the presence of CZTS and CZTS–MoS_2.

3.3.11 Photocatalytic Dye Degradation Mechanism

The photocatalytic degradation of a dye generally takes place by the following mechanism.[35] When a catalyst is exposed to UV–visible light irradiation, electrons are promoted from the valence band to the conduction band producing an electron–hole pair. The e^- and h^+ can migrate to the catalyst surface, where they can undergo a redox reaction with other species present on the surface. This prevents the recombination of the $e^-$and h^+ generated in the first step. h^+_{VB} can react easily with surface bound H_2O to produce $OH^\bullet$ radicals, whereas, e^-_{CB} can react with O_2 to produce superoxide radical anion of oxygen, $O_2^{\bullet-}$. $OH^\bullet$radicals can combine to form H_2O_2. The H_2O_2 can further react with $O_2^{\bullet-}$ to produce $OH^\bullet$, which is responsible for the degradation of the organic dye.[35]

$$\text{Photocatalyst} + h\nu \longrightarrow h^+_{VB} + e^-_{CB} \quad \textbf{(1.6)}$$

$$e^-_{CB} + O_2 \longrightarrow O_2^{\bullet -} \quad \textbf{(1.7)}$$

$$h^+_{VB} + H_2O \longrightarrow OH^\bullet + H^+ \quad \textbf{(1.8)}$$

$$OH^\bullet + OH^\bullet \longrightarrow H_2O_2 \quad \textbf{(1.9)}$$

$$H_2O_2 + O_2^{\bullet -} \longrightarrow OH^\bullet + OH^- + O_2 \quad \textbf{(1.10)}$$

$$\text{Dye} + OH^\bullet \longrightarrow CO_2 + H_2O \quad \textbf{(1.11)}$$

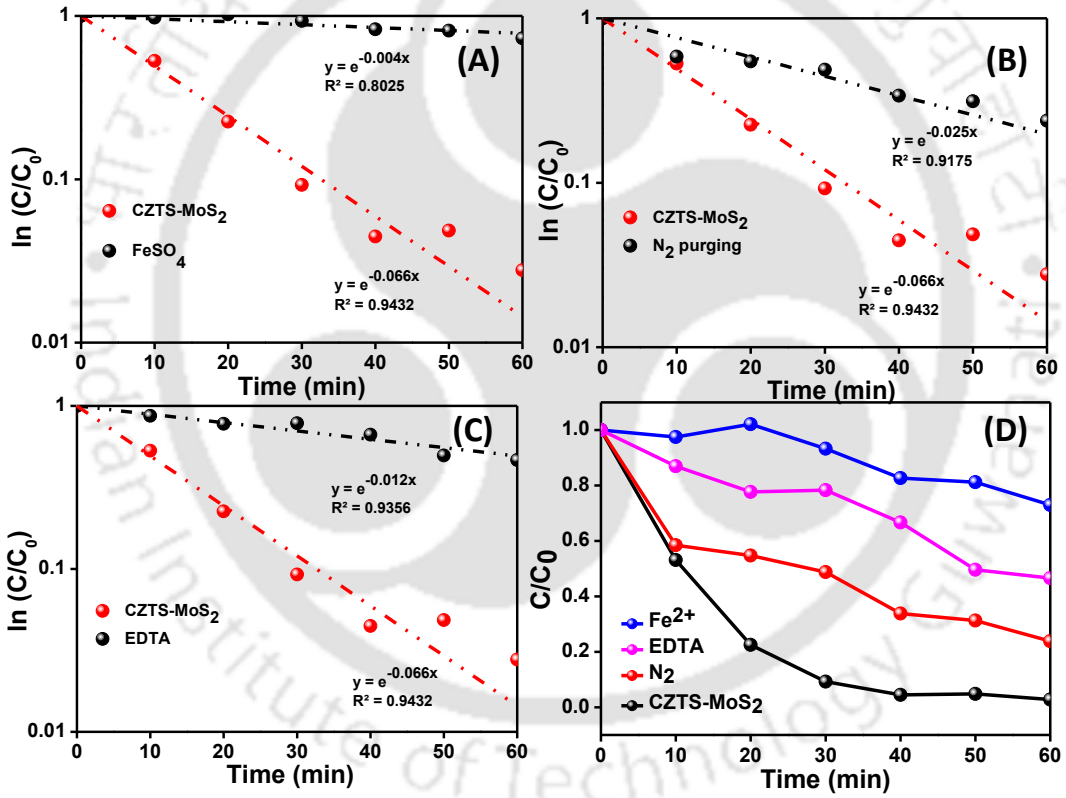

Figure 3.13: (A) Apparent rate constant of RhB dye degardation in the presence of CZTS–MoS_2 and Fe^{2+} ($OH^\bullet$ scavenger), (B) Apparent rate constant of RhB dye degardation in the presence of CZTS–MoS_2 and N_2 ($O_2^{\bullet -}$scavenger), (C) Apparent rate constant of RhB dye degardation in the presence of CZTS–MoS_2 and EDTA (hole scavenger) and (D) C/C_0 versus time (min) plot in the presence of different reactive species scavengers.

It is seen that hydroxyl radical ($OH^{\bullet}$) and superoxide anion radical ($O_2^{\bullet-}$) are mainly responsible for the degradation of the dye. Therefore in order to study the mechanism of dye degradation, various scavenger tests were performed wherein radical or hole trapping agents were added into the dye catalyst system and the rate of degradation was observed (**Figure 3.13**). $FeSO_4$, N_2 and ethylenediaminetetraacetic acid (EDTA) were used as $OH^{\bullet}$, $O_2^{\bullet-}$ and hole scavenger, respectively.[35-37]

Fe^{2+} salt was used as a $OH^{\bullet}$ trapping agent. Fe^{2+} undergoes the following reaction with $OH^{\bullet}$ present in the solution.

$$OH^{\bullet} + Fe^{2+} \longrightarrow OH^{-} + Fe^{3+}$$

This reaction has a very high rate constant ($k = 3.5 \times 10^8$ $M^{-1}s^{-1}$). In the presence of Fe^{2+}, $OH^{\bullet}$ is converted to OH^{-}, decreasing the $OH^{\bullet}$ concentration in the solution, leading to a decreased rate of dye degradation. SO_4^{2-} ions also causes a decrease in percentage degradation as they react with $OH^{\bullet}$ as,

$$SO_4^{2-} + OH^{\bullet} \longrightarrow SO_4^{\bullet-} + OH^{-}$$

Specificity of choosing $FeSO_4$ over other iron salts is that both cation and anion (Fe^{2+} and SO_4^{2-}) can act as the $OH^{\bullet}$ scavengers. The apparent rate constant (k_{app}) for RhB dye degradation in presence of $FeSO_4$ was less (0.004 min^{-1}) than that without the metal ion (0.066 min^{-1}) as can be seen in **Figure 3.13 (A)**.

Another important intermediate that plays an important role in the degradation process is superoxide radical anion ($O_2^{\bullet-}$) which is formed by the reduction of dissolved molecular oxygen in water. In order to prove its role, degradation experiment was carried out under continuous N_2 purging which is used to replace the dissolved oxygen from the system. The apparent rate constant (k_{app}) for degradation in deoxygenated water was less (0.025 min^{-1}) than that in normal oxygenated water (0.066 min^{-1}) as can be seen in **Figure 3.13 (B)**, proving the importance of dissolved oxygen in generating superoxide radical, which enhances the kinetics of degradation.

Further a degradation experiment was performed in the presence of EDTA which acts as a hole scavenger. The plot for apparent rate constant (k_{app}) for degradation showed a lower

rate constant (0.012 min^{-1})in presence of EDTA as compared to the rate constant in the absence of EDTA (0.066 min^{-1}) (**Figure 3.13 (D)**).

Although, each scavenger has its role to play in controlling the kinetics of dye degradation, it was observed that $OH^{\bullet}$ plays more prominent role, evident from the slower kinetic data in the presence of $OH^{\bullet}$ scavenger ($FeSO_4$). Hence, we propose that hydroxyl radical ($OH^{\bullet}$) could be the determining species in controlling the kinetics of the dye degradation.

3.4 CONCLUSION

In conclusion, quaternary CZTS and its composite with a co–catalyst viz. MoS_2 were prepared by a facile hydrothermal method. The enhanced photocatalytic ability of the composite was evaluated by its appreciable water reduction ability to evolve H_2 with AQY of 22.67%, and better efficiency in degradation of RhB dye as a reference pollutant, compared to bare CZTS. The faster photo degradation of RhB dye by CZTS–MoS_2 in comparison to CZTS is substantiated by kinetic studies. The various scavenger tests showed the major role of hydroxyl radical in the photo degradation of RhB dye.

3.5 REFERENCES

1. A. Kudo and Y. Miseki, *Chem. Soc. Rev.*, 2009, **38**, 253.
2. A. Shavel, J. Arbiol and A. Cabot, *J. Am. Chem. Soc.*, 2010, **132**, 4514.
3. S. Yang, Q. Yue, F. Wua, N. Huo, Z. Chen, J. Yang and J. Li, *J. Alloys Compd.*, 2014, **597**, 91.
4. P. Hu, S. S. Pramana, S. Cao, C. K. Ngaw, J. Lin, S. C. J. Loo and T. T. Y. Tan, *Adv. Mater.*, 2013, **25**, 2567.
5. D. Yokoyama, T. Minegishi, K. Maeda, M. Katayama, J. Kubota, A. Yamada, M. Konagai and K. Domen, *Electrochem. Commun.*, 2010, **12**, 851.
6. M. Tabata, K. Maeda, T. Ishihara, T. Minegishi, T. Takata and K. Domen, *J. Phys. Chem. C*, 2010, **114**, 11215.
7. J. Kim, T. Minegishi, J. Kobotaa and K. Domen, *Energy Environ. Sci.*, 2012, **5**, 6368.
8. H. Kumagai, T. Minegishi, Y. Moriya, J. Kubota and K. Domen, *J. Phys. Chem. C*, 2014, **118**, 16386.

9. Gunawan, W. Septina, S. Ikeda, T. Harada, T. Minegishi, K. Domen and M. Matsumuraa, *Chem. Commun.*, 2014, **50**, 8941.
10. I. Tsuji, H. Kato, H. Kobayashi and A. Kudo, *J. Phys. Chem. B*, 2005, **109**, 7323.
11. S. Ikeda, M. Nonogaki, W. Septina, G. Gunawan, T. Haradaa and M. Matsumuraa, *Catal. Sci. Technol.*, 2013, **3**, 1849.
12. M. Moriya, T. Minegishi, H. Kumagai, M. Katayama, J. Kubota and K. Domen, *J. Am. Chem. Soc.*, 2013, **135**, 3733.
13. J. Wang, P. Zhang, X. Song and L. Gao, *RSC Adv.*, 2014, **4**, 27805.
14. W. C. Liu, B. L. Guo, X. S. Wu, F. M. Zhang, C. L. Mak and K. H. Wong, *J. Mater. Chem. A*, 2013, **1**, 3182.
15. T. R. Knutson, P. J. Hanson, E. S. Aydil and R.L. Penn, *Chem. Commun.*, 2014, **50**, 5902.
16. J. W. Cho, A. Ismail, S. J. Park, W. Kim, S. Yoon and B. K. Min, *ACS Appl. Mater. Interfaces*, 2013, **5**, 416.
17. S. K. Saha, A. Guchhait and A. J. Pal, *Phys. Chem. Chem. Phys.*, 2012, **14**, 8090.
18. B. Shin, O. Gunawan, Y. Zhu, N. A. Bojarczuk, S. J. Chey and S. Guha, *Prog. Photovolt: Res. Appl.*, 2013, **21**, 72.
19. X. Yu, A. Shavel, X. An, Z. Luo, M. Ibanez and A. Cabot, *J. Am. Chem. Soc.*, 2014, **136** , 9236.
20. S. C. Riha, S. J. Fredrick, J. B. Sambur, Y. Liu, A. L. Prieto and B. A. Parkinson, *ACS Appl. Mater. Interfaces*, 2011, **3**, 58.
21. E. Ha, L. Y. S. Lee, J. Wang, F. Li, K. –Y. Wong and S. C. E. Tsang, *Adv. Mater.*, 2014, **26**, 3496.
22. D. Chen, Y. Zhao, Y. Chen, B. Wang, H. Chen, J. Zhou and Z. Liang, *ACS Appl. Mater. Interfaces*, 2015, **7**, 3224−3230.
23. S. Yang, J. Kang, Q. Yue, and K. Yao, *J. Phys. Chem. C*, 2014, **118**, 9203.
24. T. Jia, A. Kolpin, C. Ma, R. C. T. Chan, W. M. Kwok and S. C. E. Tsang, *Chem. Commun.*, 2014, **50**, 1185.
25. Y. L. Min, G. Q. He, Q. J. Xu and Y. C. Chen, *J. Mater. Chem. A*, 2014, **2**, 2578.
26. M. Shen, Z. Yan, L. Yang, P. Du, J. Zhang and B. Xiang, *Chem. Commun.*, 2014, **50**, 15447.

27. Y. Zhu, Q. Ling, Y. Liu, H. Wangb and Y. Zhu, *Phys. Chem. Chem. Phys.*, 2015, **17**, 933.
28. W. Wang, K. Zhang, Z. Qiao, L. Li, P. Liu and Y. Yang, *Ind. Eng. Chem. Res.*, 2014, **53**, 10301.
29. L. Wang, W. Wang and S. Sun, *J. Mater. Chem*., 2012, **22**, 6553.
30. S. Huang, W. Luo and Z. Zou, *J. Phys. D: Appl. Phys.*, 2013, **46,** 235108.
31. M. Z. Ansari and N. Khare, *J. Phys. D: Appl. Phys*., 2014, **47**, 185101.
32. P. A. Fernandes, P. M. P. Salom´e and A. F. Cunha, *J. Alloys Compd.*, 2011, **509**, 7600.
33. P. Tonndorf, R. Schmidt, P. Böttger, X. Zhang, J. Börner, A. Liebig, M. Albrecht, C. Kloc, O. Gordan, D. R. T. Zahn, S. Michaelis de Vasconcellos, and R. Bratschitsch, *Opt. Express*, 2013, **21**, 4908.
34. K. S. W. Sing, D. H. Everett, R. A. W. Haul, L. Moscou, R. A. Pierotti, J. Rouquerol and T. Siemieniewska, *Pure & Appl. Chem.*, 1985, **57**, 603.
35. M. A. Rauf and S. S. Ashraf, *Chem. Eng. J.*, 2009, **151**, 10.
36. Z. Khan, T. R. Chetia and M. Qureshi, *Nanoscale*, 2012, **4**, 3543.
37. G. Naresh and T. K. Mandal, *ACS Appl. Mater. Interfaces*, 2014, **6**, 21000.

Chapter 4

Hybrid of g-C_3N_4 and MoS_2 Integrated onto $Cd_{0.5}Zn_{0.5}S$: Rational Design with Efficient Charge Transfer for Enhanced Photocatalytic Activity

This chapter describes the design and synthesis of a noble-metal-free ternary hierarchical composite, $Cd_{0.5}Zn_{0.5}S$-g-C_3N_4-MoS_2. The heterostructure was studied for photocatalytic activity of water reduction and degradation of organic pollutant, Rhodamine B. The ternary composite resulted in ~197% ($Cd_{0.5}Zn_{0.5}S$–g-C_3N_4–MoS_2) increment in hydrogen evaluation activity compared to bare $Cd_{0.5}Zn_{0.5}S$ with an apparent quantum yield (AQY) of 38% at 420 nm. The significant increment of activity is attributed to the favourable charge transfer in the composite. A detailed analysis of the mechanism of interfacial charge transfer in the composite is carried out by several instrumental techniques.

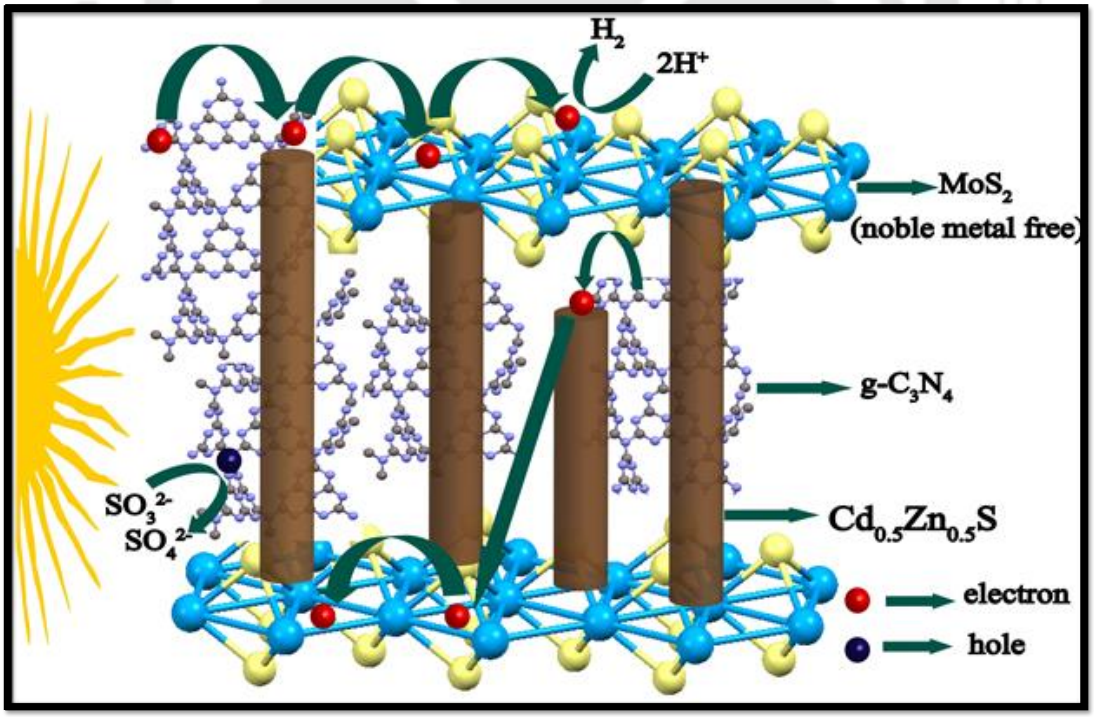

ACS Sustainable Chem. Eng., 2018, **6**, 6718.

4.1 INTRODUCTION

Among the several sulfide materials discovered for photocatalytic water reduction, CdS is quite promising, because of its strongly visible–light–absorbing direct bandgap ($E_g \approx$ 2.3 eV) and a conduction band capable of reducing protons to H_2.[1-5] Yet, it is limited due to rapid recombination of photogenerated charge carriers and photocorrosion.[6] ZnS, another widely used sulfide photocatalyst, is more stable than CdS but suffers from poor visible light absorption ($E_g \approx 3.6$ eV).[7] Consequently, there has been an attempt to combine both CdS and ZnS in order to design a stable and effective photocatalyst for H_2 evolution with visible light absorption. In this regard, a solid solution of ternary chalcogenide combining CdS and ZnS to form $Cd_xZn_{1-x}S$ is quite promising due to its tunable optical properties by varying the *x* value.[8] $Cd_{0.5}Zn_{0.5}S$ has been shown to be an efficient photocatalyst for H_2 evolution and has a suitable bandgap for visible light absorption ($E_g \approx 2.4$ eV) and conduction band edge for H_2 evolution.[9-11] However, bare $Cd_{0.5}Zn_{0.5}S$ still suffers from faster recombination of photogenerated electron–hole pairs and thus require an efficient extraction of the photogenerated electrons before recombination.[8]

Another very promising visible–light active photocatalyst is graphitic carbon nitride (g-C_3N_4), a metal free, two–dimensional conjugated layered polymer. It shows decent activity as a photocatalyst material due to its excellent stability, nontoxic nature, visible–light absorption ability ($E_g \approx 2.7$ eV), suitable band–edge positions for water splitting, and facile synthesis from amply available precursors like urea and melamine.[12-15] However, bare g-C_3N_4 too suffers from rapid recombination of photoinduced electron–hole pair and limited surface area.[16-18] Efforts to decrease the rates of recombination have included the development of heterogeneous systems by combining g-C_3N_4 with other visible–light active photocatalysts. These heterostructures are designed to facilitate charge separation and decrease the rate of charge recombination.[19-21] In a heterostructure with different components absorbing in different regions of the solar spectrum, can result in an enhanced light harvesting. Thus light harvesting ability can be promoted along with the efficient charge separation in a suitable hierarchical heterostructure in which the semiconductor has an appropriate band gap and band alignment.[22-24] A heterostructure of $Cd_{0.5}Zn_{0.5}S$ and g-C_3N_4, both absorbing in the visible region, have suitable band alignment for efficient charge separation. Several works have reported the synthesis and characterisation of binary composite, g-C_3N_4/$Cd_xZn_{1-x}S$, where

$Cd_xZn_{1-x}S$ is the electron acceptor to facilitate charge separation and slow charge recombination.[25-27]

The efficiency of a photocatalyst can be further enhanced by integration of a co–catalyst to facilitate charge extraction and provide active sites for the photocatalytic reaction.[28-32] The photocatalytic efficiency of $Cd_xZn_{1-x}S$ has been shown to increase with loading of co–catalysts like Pt,[33] Au,[34] bimetallic AuPd,[35] Pt-RuS_2,[36] and $CoPt_3$[37]. Molybdenum disulfide (MoS_2) is a two–dimensional layered material widely used as a H_2 evolution co–catalyst.[38, 39] It has been reported for enhanced photocatalytic activity on integration with $Cd_xZn_{1-x}S$.[40-42]

In this work, $Cd_{0.5}Zn_{0.5}S$–g-C_3N_4 was integrated with MoS_2 to form a ternary composite that exhibits better photocatalytic activity compared to the binary composite $Cd_{0.5}Zn_{0.5}S$–g-C_3N_4 as well as bare counterpart, $Cd_{0.5}Zn_{0.5}S$. We report the synthesis, characterisation, photocatalytic H_2 evolution efficiency and dye degradation ability of bare $Cd_{0.5}Zn_{0.5}S$, its binary composite with g-C_3N_4 ($Cd_{0.5}Zn_{0.5}S$–g-C_3N_4), and a ternary composite with MoS_2 ($Cd_{0.5}Zn_{0.5}S$–g-C_3N_4–MoS_2). The composites were prepared by ultrasonic mixing of specific weight percentage of each component with bare $Cd_{0.5}Zn_{0.5}S$. As prepared, $Cd_{0.5}Zn_{0.5}S$–g-C_3N_4–MoS_2 shows an enhanced photocatalytic H_2 activity compared to $Cd_{0.5}Zn_{0.5}S$–g-C_3N_4 and $Cd_{0.5}Zn_{0.5}S$. The enhanced efficiency is attributed to the superior interfacial contact between the components and synergistic transportation and separation of the photogenerated charge carriers, thereby slowing recombination, as well as increased rate of catalysis due to the presence of MoS_2 co–catalyst.

4.2 EXPERIMENTAL SECTION

4.2.1 Preparation of $Cd_{0.5}Zn_{0.5}S$

$Cd_{0.5}Zn_{0.5}S$ was prepared by a solvothermal method.[43] In a typical synthesis protocol, zinc acetate ($Zn(Ac)_2.H_2O$) (2.19 g, 10 mmol), cadmium acetate ($Cd(Ac)_2.2H_2O$) (2.665 g, 10 mmol) and thioacetamide (C_2H_5NS) (3.0052 g, 40 mmol) were added to ethylenediamine ($C_2H_4(NH_2)_2$) (60 mL) and were left to stir for 1 h. This solution was then heated in a 100 mL Teflon-lined stainless steel autoclave to 180 °C, held at 180 °C for 24 h, and then cooled down naturally to room temperature. The precipitate that formed was washed several times with

deionised water and ethanol in order to remove residual ions, followed by drying at 60 °C overnight. Control synthesis of pure ZnS and CdS were synthesised using only Zn^{2+} and Cd^{2+} precursors in an aqueous medium.

4.2.2 Preparation of MoS_2

Hexamine ($C_6H_{12}N_4$) (0.140 g, 1 mmol) was dissolved in deionised water (30 mL) followed by the addition of ammonium heptamolybdate ($(NH_4)_6Mo_7O_{24}.4H_2O$) (0.123 g, 0.1 mmol) under stirring. After complete dissolution, L-cysteine ($C_3H_7NO_2S$) (0.169 g, 1.4 mmol) was added and stirred for 30 min. The solution was then heated at 200 °C for 12 h in a 50 mL Teflon–lined stainless steel autoclave and then cooled naturally to room temperature. The precipitate was separated and washed several times with deionized water and ethanol, followed by drying at 60 °C overnight.

4.2.3 Preparation of g-C_3N_4

g-C_3N_4 was prepared by self–condensation of melamine at high temperature. Melamine (5 g) was heated at a rate of 10 °C/min to 520 °C in a muffle furnace, held for 6 h at 520 °C, and then cooled down naturally to room temperature. The obtained yellow powder was grounded and used for further characterisations.

4.2.4 Preparation of $Cd_{0.5}Zn_{0.5}S$–g-C_3N_4 and $Cd_{0.5}Zn_{0.5}S$–g-C_3N_4–MoS_2 Composites

$Cd_{0.5}Zn_{0.5}S$–*x*%g-C_3N_4 (*x* = 10, 20, 30, 40, 50) and $Cd_{0.5}Zn_{0.5}S$–g-C_3N_4–*x*%MoS_2 (*x* = 1, 3, 5, 7) composites were prepared by ultrasonication of the components in specific weight percentage for 1 h in ethanol (5 mL) to form a dispersion followed by drying at 60 °C overnight. Use of ultrasonication is expected to facilitate formation of intimate contacts between the individual components.

4.3 RESULTS AND DISCUSSION

4.3.1 Powder X–ray Diffraction (PXRD) Patterns

The powder X–ray diffraction (PXRD) patterns of g-C_3N_4, MoS_2, CdS, ZnS, $Cd_{0.5}Zn_{0.5}S$, $Cd_{0.5}Zn_{0.5}S$–30%g-C_3N_4 and $Cd_{0.5}Zn_{0.5}S$–30%g-C_3N_4–5%MoS_2 (represented as $Cd_{0.5}Zn_{0.5}$–g-C_3N_4 and $Cd_{0.5}Zn_{0.5}S$–g-C_3N_4–MoS_2 hereafter) are shown in **Figure 4.1**. PXRD

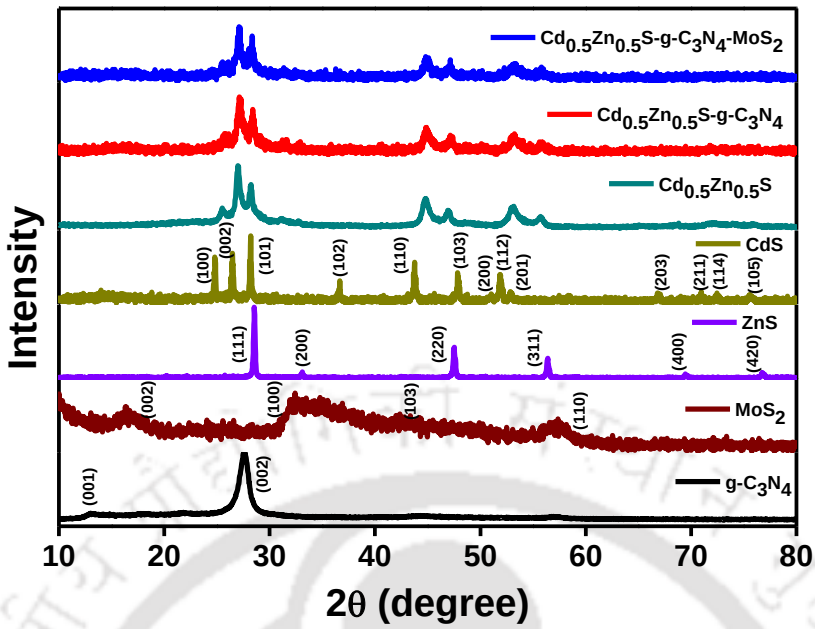

Figure 4.1: Powder X–ray diffraction pattern of $Cd_{0.5}Zn_{0.5}S$–g-C_3N_4–MoS_2, $Cd_{0.5}Zn_{0.5}S$–g-C_3N_4, $Cd_{0.5}Zn_{0.5}S$, bare CdS, ZnS, MoS_2 and g-C_3N_4.

pattern of g-C_3N_4 exhibited a characteristic major peak at 27.3° corresponding to the (002) crystal plane due to the stacking of conjugated aromatic system, while the low intensity peak at 13.2° corresponds to the (001) plane, indicative of a periodic arrangement of condensed tri–s–triazine units in the g-C_3N_4 sheets.[12] In the PXRD pattern of MoS_2, diffraction peaks appearing at 2θ = 16.7°, 33.4°, 43.5° and 57.4° correspond to (002), (100), (103), and (110) lattice planes of a hexagonal phase (JCPDS file No. 37-1592). The as–prepared MoS_2 is weakly crystalline, as proved by the broad (002) diffraction peak which indicates poor stacking and highly disordered packing of MoS_2 layers.[44] Bare ZnS shows diffraction at 2θ = 28.5°, 33.08°, 47.5°, 56.2°, 69.5°, 76.8° corresponding to (111), (200), (220), (311), (400), (420) planes of cubic phase ZnS (JCPDS file No. 05-0566). PXRD of CdS shows diffraction peaks at 2θ = 24.8°, 26.5°, 28.1°, 36.6°, 43.6°, 47.8°, 50.8°, 51.8°, 52.7°, 66.7°, 70.8°, 72.3°, 75.4° which are indexable to (100), (002), (101), (102), (110), (103), (200), (112), (201), (203), (211), (114), (105) planes of hexagonal phase CdS (JCPDS file No. 41-1049). The PXRD pattern of $Cd_{0.5}Zn_{0.5}S$ synthesised by a solvothermal method shows a shift in position of diffraction peaks compared to bare CdS. It can be inferred that the as-prepared sample is not just a physical mixture of CdS and ZnS but a solid solution of $Cd_xZn_{1-x}S$.[45] In the alloyed $Cd_xZn_{1-x}S$, Zn^{2+} (ionic radius (0.74 Å)) gets incorporated into the CdS lattice or may sit at interstitial sites leading to disorder in the crystal structure.[43] Moreover, the PXRD pattern of

$Cd_{0.5}Zn_{0.5}S$ and its composites exhibit lower crystallinity than bare CdS or ZnS which can be attributed to the disorder generated in the crystal structure as a result of incorporation of Zn^{2+} into the CdS lattice.[46, 47] In the composites $Cd_{0.5}Zn_{0.5}S$–g-C_3N_4 and $Cd_{0.5}Zn_{0.5}S$–g-C_3N_4–MoS_2 there is no apparent peaks of g-C_3N_4 and MoS_2, due to the low percentage of loading of the components. The single–layer structure of MoS_2 might also be attributed for the absence of MoS_2 diffraction peak in $Cd_{0.5}Zn_{0.5}S$–g-C_3N_4–MoS_2.[40] Moreover, the significant peaks of g-C_3N_4 and MoS_2 overlap with that of $Cd_{0.5}Zn_{0.5}S$ which supresses its occurrence in the PXRD measurements of these composites.

4.3.2 X-Ray Photoelectron Spectroscopy (XPS) Spectra

X-ray photoelectron spectroscopy (XPS) analyses were carried out in order to probe the local electronic environment of the prepared samples. All the peaks were calibrated with respect to C 1s at 284.7 eV. From the high-resolution core-level spectra of Cd 3d, Zn 2p and S 2p of $Cd_{0.5}Zn_{0.5}S$ (**Figure 4.2 (A)**, **Figure 4.2 (B)** and **Figure 4.2 (C)**, respectively), the peaks corresponding to Cd^{2+} $3d_{3/2}$, Cd^{2+} $3d_{5/2}$, Zn^{2+} $2p_{3/2}$, Zn^{2+} $2p_{1/2}$, S^{2-} $2p_{3/2}$ and S^{2-} $2p_{1/2}$ are observed at binding energies of 404.6, 411.32, 1020.98, 1044, 161.23 and 162.4 eV, respectively.[27, 48] The peaks at 162.1 and 163.6 eV in S 2p of MoS_2, correspond to the S $2p_{3/2}$ and S $2p_{1/2}$ of divalent sulfide (S^{2-}) of MoS_2 (**Figure 4.2 (D)**).[49] The asymmetric N 1s spectra of g-C_3N_4 has been fitted using the deconvolution method with three major Gaussian component peaks at 398.51, 399.26 and 400.65 eV, respectively (**Figure 4.2 (E)**). This provides strong evidence for the existence of the chemical bonding modes of nitrogen species corresponding to sp^2–bonded N (C–N=C), tertiary nitrogen N–$(C)_3$ groups, and amino groups (C–N–H), respectively in the g-C_3N_4 sheets.[50] In **Figure 4.2 (A)**, **Figure 4.2 (B)** and **Figure 4.2 (C)**, it is seen that in the composite $Cd_{0.5}Zn_{0.5}S$–g-C_3N_4–MoS_2, the Cd 3d, Zn 2p and S 2p are slightly shifted to higher binding energies (405.14 and 411.89 eV for Cd^{2+} $3d_{3/2}$ and Cd^{2+} $3d_{5/2}$; 1021.86 and 1044.93 eV for Zn^{2+} $2p_{3/2}$ and Zn^{2+} $2p_{1/2}$; 161.7 and 162.86 eV for S^{2-} $2p_{3/2}$ and S^{2-} $2p_{1/2}$, respectively) compared to that of $Cd_{0.5}Zn_{0.5}S$. Due to the favourable band

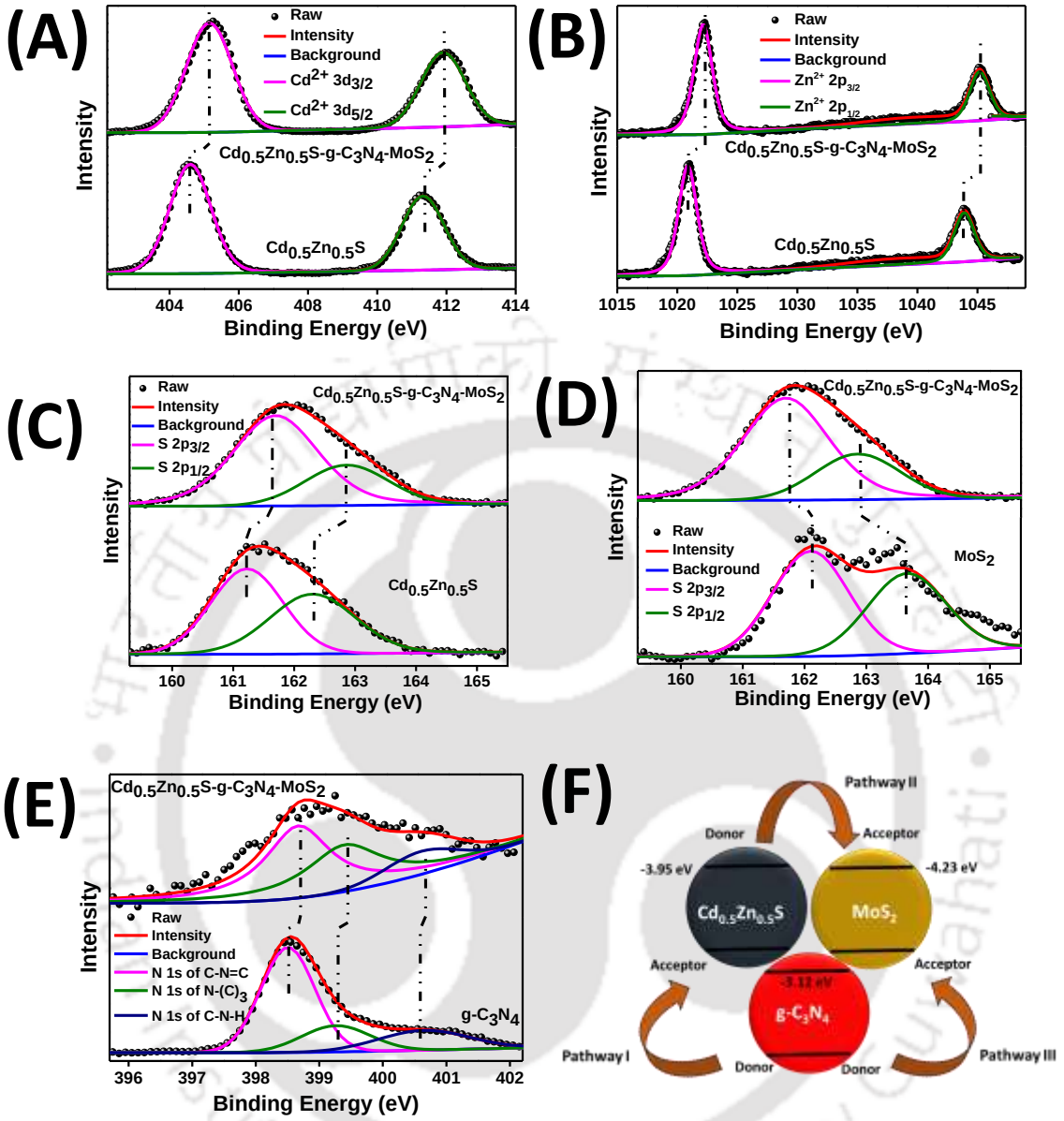

Figure 4.2: X-Ray photoelectron spectroscopy (XPS) spectra of (A) Cd 3d, (B) Zn 2p, (C, D) S 2p, (E) N 1s and (F) Schematic representation of the different possible charge transfer pathways in the composite $Cd_{0.5}Zn_{0.5}S$–g-C_3N_4–MoS_2.

alignments at the interfaces, there is a possibility of electronic interactions among g-C_3N_4, $Cd_{0.5}Zn_{0.5}S$ and MoS_2 leading to a change in the electron density on all the components in the composite. Based on the interfacial positions, electrons will transfer from $Cd_{0.5}Zn_{0.5}S$ (donor) to MoS_2 (acceptor) leading to a decreased electron density around the S 2p of $Cd_{0.5}Zn_{0.5}S$ and enhanced density distribution around S 2p of MoS_2 (Pathway II in **Figure 4.2 (F)**). Moreover, there is another possible charge–transfer pathway based on the band alignments where

$Cd_{0.5}Zn_{0.5}S$ can act as an acceptor of an electron from photo-excited g-C_3N_4 (Pathway I in **Figure 4.2 (F)**). On comparing the S 2p core level spectra of $Cd_{0.5}Zn_{0.5}S$–g-C_3N_4–MoS_2 with that of bare $Cd_{0.5}Zn_{0.5}S$, it is observed that S 2p of the composite is shifted towards higher binding energy (**Figure 4.2 (C)**) due to the reduction of S 2p electron density in $Cd_{0.5}Zn_{0.5}S$–g-C_3N_4–MoS_2 as compared to $Cd_{0.5}Zn_{0.5}S$.[51] This change in the binding energy of S 2p reflects that Pathway II is more competitive than Pathway I. Analysis of N 1s peak of g-C_3N_4 in $Cd_{0.5}Zn_{0.5}S$–g-C_3N_4–MoS_2 also shows a shift toward higher binding energy (398.56, 399.31 and 400.7 eV, respectively) compared to that of bare g-C_3N_4 (**Figure 4.2 (E)**). The shift is based on the favourable charge transfer from g-C_3N_4 to the other components of the composite, i.e. $Cd_{0.5}Zn_{0.5}S$ and MoS_2 (Pathway I and Pathway III in **Figure 4.2 (F)**, respectively), which leads to a reduction of the electron density of N 1s in the composite. The Mo 3d spectra of MoS_2 can be deconvoluted into four components corresponding to the binding energy of S 2s (226.4 eV), $3d_{5/2}$ and $3d_{3/2}$ of Mo (229.26 and 233.09 eV, respectively) and Mo^{6+} (236.5 eV) (**Figure 4.3**). The observance of Mo^{6+} may be due to atmospheric oxidation of MoS_2 during storage in laboratory conditions.[52]

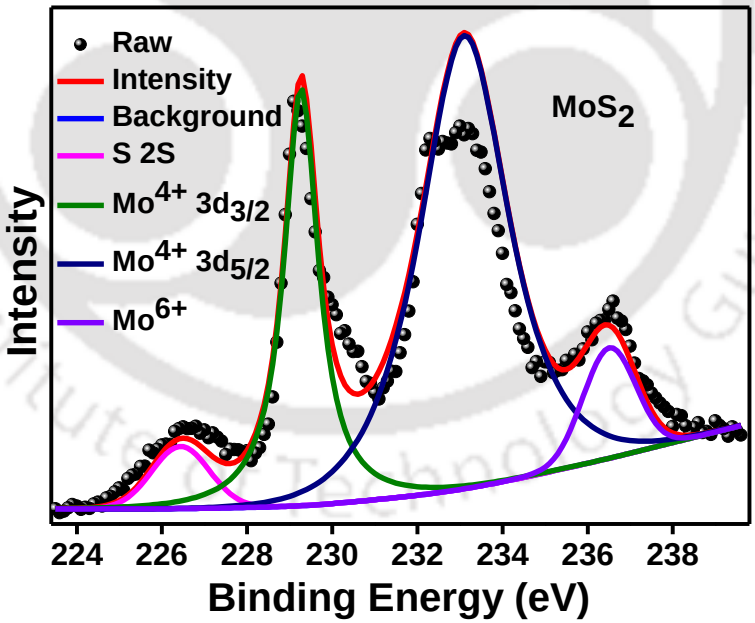

Figure 4.3: X-Ray photoelectron spectroscopy (XPS) spectra of Mo 3d of MoS_2.

Comparing the individual MoS_2 component to that of the composite, the S 2p of bare MoS_2 has a higher binding energy than the S 2p of $Cd_{0.5}Zn_{0.5}S$–g-C_3N_4–MoS_2 (**Figure 4.2 (D)**). In the composite, there is an increase in the electron density on the conduction band of MoS_2 than that of bare MoS_2, leading to the shift of S 2p to a lower binding energy in the

composite than MoS_2 (**Figure 4.2 (D)**). The shift in binding energy between the composite and bare components is likely due to charge transfer from $Cd_{0.5}Zn_{0.5}S$ and g-C_3N_4 to MoS_2 (Pathway II and Pathway III in **Figure 4.2 (F)**, respectively).

4.3.3 Ultraviolet-Visible Diffuse Reflectance Spectroscopy

Figure 4.4 (A) represents the ultraviolet–visible diffuse reflectance spectra of $Cd_{0.5}Zn_{0.5}S$, g-C_3N_4, MoS_2, ZnS, CdS and the composites $Cd_{0.5}Zn_{0.5}S$–g-C_3N_4 and $Cd_{0.5}Zn_{0.5}S$–g-C_3N_4–MoS_2. Bare ZnS absorbs in the ultraviolet spectral region (absorbance onset at ~ 350 nm) and CdS has an absorbance onset in the visible region at ~ 590 nm as observed from **Figure 4.4 (A)**. As expected, the absorption onset of $Cd_{0.5}Zn_{0.5}S$ occurs in between its constituents at ~ 520 nm. **Figure 4.4 (B)** depicts the Tauc plots of $Cd_{0.5}Zn_{0.5}S$–g-C_3N_4–MoS_2, $Cd_{0.5}Zn_{0.5}S$–g-C_3N_4, $Cd_{0.5}Zn_{0.5}S$, ZnS, CdS, g-C_3N_4 and MoS_2 (inset of **Figure 4.4 (B)**), which enables determination of the bandgap energy. Tauc plots is a plot of $(\alpha h\nu)^2$ versus the photon energy ($h\nu$), where α is the absorption coefficient. The bandgap values of $Cd_{0.5}Zn_{0.5}S$–g-C_3N_4–MoS_2, $Cd_{0.5}Zn_{0.5}S$–g-C_3N_4 and $Cd_{0.5}Zn_{0.5}S$ are estimated to be 2.41, 2.38, and 2.35 eV, respectively, which is intermediate of ZnS (3.6 eV) and CdS (2.25 eV). The band gap of g-C_3N_4 and MoS_2 are estimated to be 2.7 and 1.46 eV, respectively. The estimated band gaps are tabulated in **Table 4.1**.

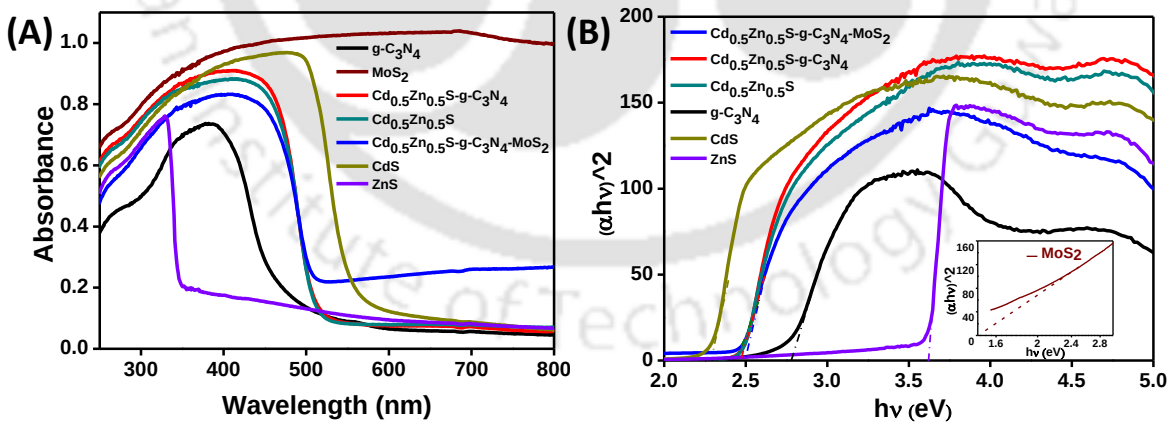

Figure 4.4: (A) Ultraviolet–visible diffuse reflectance spectra of $Cd_{0.5}Zn_{0.5}S$–g-C_3N_4–MoS_2, $Cd_{0.5}Zn_{0.5}S$–C_3N_4, $Cd_{0.5}Zn_{0.5}S$, g-C_3N_4, MoS_2, CdS and ZnS and (B) Tauc plot to estimate optical band gap values.

Electronic absorption spectra of all compositions $Cd_{0.5}Zn_{0.5}S$–x%g-C_3N_4 (x = 10, 20, 30, 40, 50) and $Cd_{0.5}Zn_{0.5}S$–g-C_3N_4–x%MoS_2 (x = 1, 3, 5, 7) are shown in **Figure 4.5 (A)** and

Figure 4.5 (B), respectively. From **Figure 4.5**, it is observed that the absorption onset of all the compounds are in the visible range of the spectra.

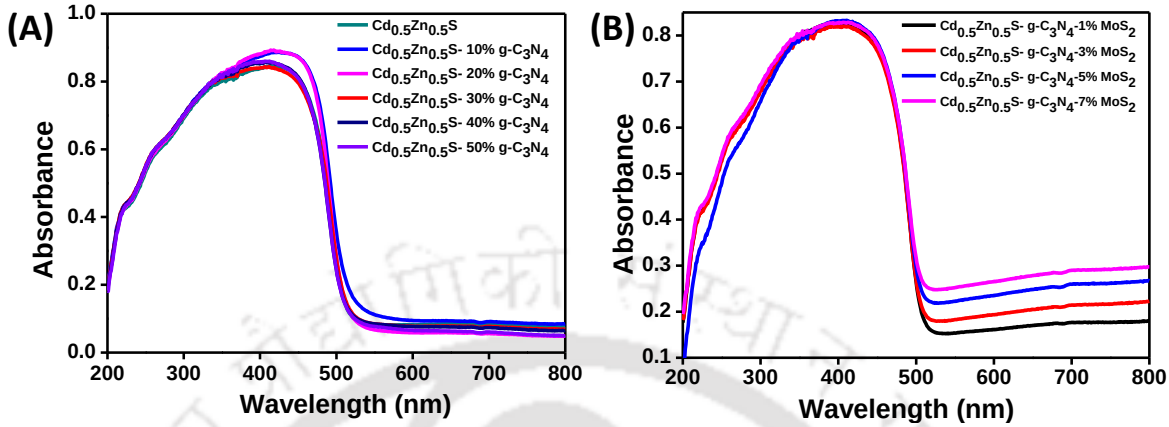

Figure 4.5: Ultraviolet–visible diffuse reflectance spectra of (A) $Cd_{0.5}Zn_{0.5}S$–*x*%g-C_3N_4 (*x* = 10, 20, 30, 40, 50) and (B) $Cd_{0.5}Zn_{0.5}S$–g-C_3N_4–*x*% MoS_2 (*x* = 1, 3, 5, 7).

Table 4.1: Estimated band gap values

Compound	Band gap (eV)
CdS	2.25
ZnS	3.6
g-C_3N_4	2.7
MoS_2	1.46
$Cd_{0.5}Zn_{0.5}S$	2.35
$Cd_{0.5}Zn_{0.5}S$–g-C_3N_4	2.38
$Cd_{0.5}Zn_{0.5}S$–g-C_3N_4–MoS_2	2.41

4.3.4 Field-Emission Scanning Electron Microscopy

Figure 4.6 and **Figure 4.7** show Field-Emission Scanning Electron Microscopy (FESEM) images of the as-prepared materials at different magnifications. $Cd_{0.5}Zn_{0.5}S$ exhibits nanorod like morphology with an average length of around 100 nm (**Figure 4.6 (A)** and **Figure 4.6 (B)**). The ethylenediamine used as solvent in the synthesis of $Cd_{0.5}Zn_{0.5}S$, is also a good bidentate coordinating agent with Cd^{2+} and Zn^{2+} to form $[Cd(EDA)_n]^{2+}$ and

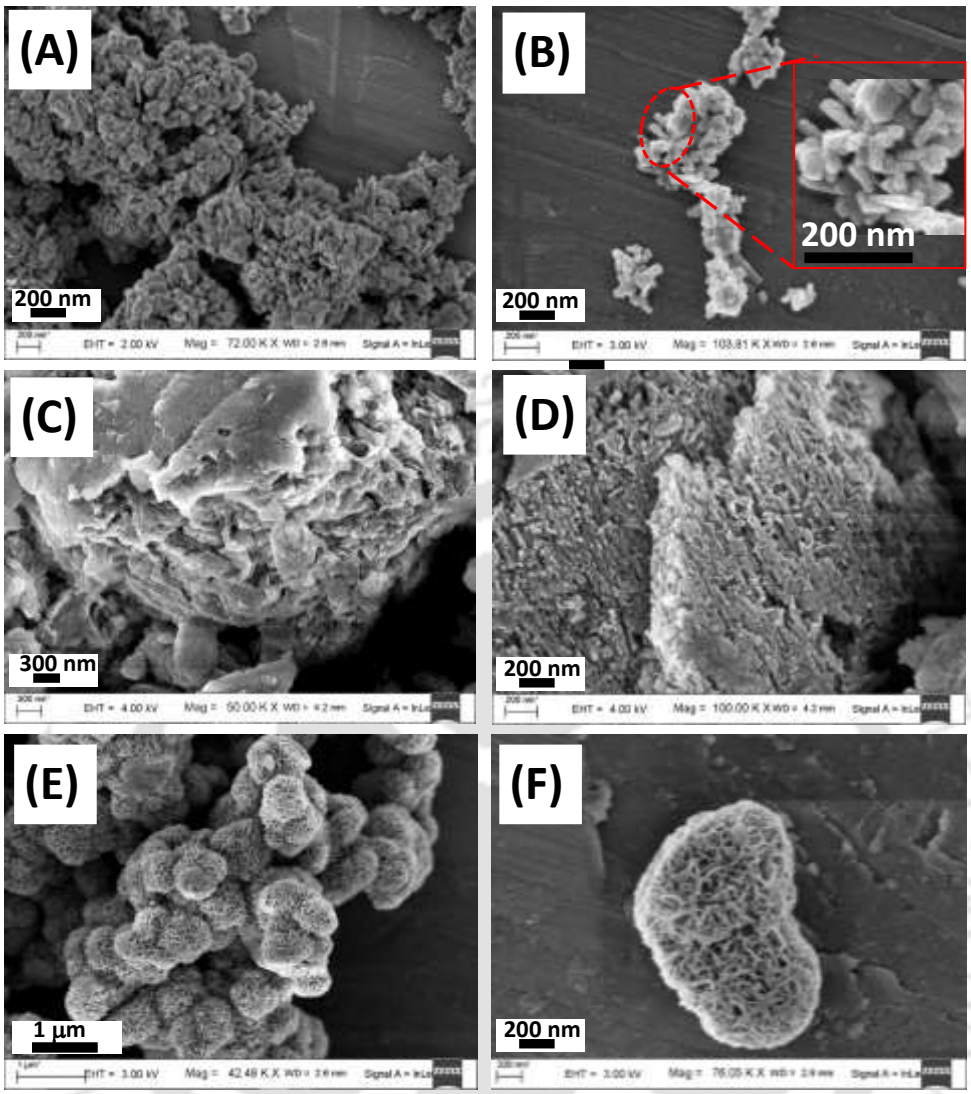

Figure 4.6: Field-emission scanning electron microscopy (FESEM) images of (A, B) $Cd_{0.5}Zn_{0.5}S$, (C, D) g-C_3N_4 and (E, F) MoS_2 at different magnifications

$[Zn(EDA)_n]^{2+}$ complexes.[53, 54] As the temperature increases, thioacetamide, used as sulfur source in $Cd_{0.5}Zn_{0.5}S$, decomposes gradually to release S^{2-}. Finally, $[Cd(EDA)_n]^{2+}$ and $[Zn(EDA)_n]^{2+}$ complexes react with S^{2-} and yield a $Cd_xZn_{1-x}S$ solid solution. Zn^{2+} strongly coordinates with EDA and therefore, with only Zn^{2+} ($x = 0$), ZnS-$(EDA)_{0.5}$ forms instead of ZnS.[55] The use of ethylene diamine as a solvent promotes the unidirectional growth of CdS along c-axis while it promotes the growth of ZnS in the a-b plane.[43] It is observed that for $x = 0.5$ in $Cd_xZn_{1-x}S$, the morphology is predominantly rod shaped though with a lower aspect ratio. FESEM images of g-C_3N_4 reveal its flake-like and porous in nature (**Figure 4.6 (C)** and **Figure 4.6 (D)**). MoS_2 consists of nanosheets as porous bunched structures that are ~ 500 nm

in diameter (**Figure 4.6 (E)** and **Figure 4.6 (F)**). MoS_2 has a large exposed surface area that can provide greater active sites for H_2 evolution during the catalytic process. This includes a larger fraction of edge sites which are indicated as active sites for H_2 evolution.[56]

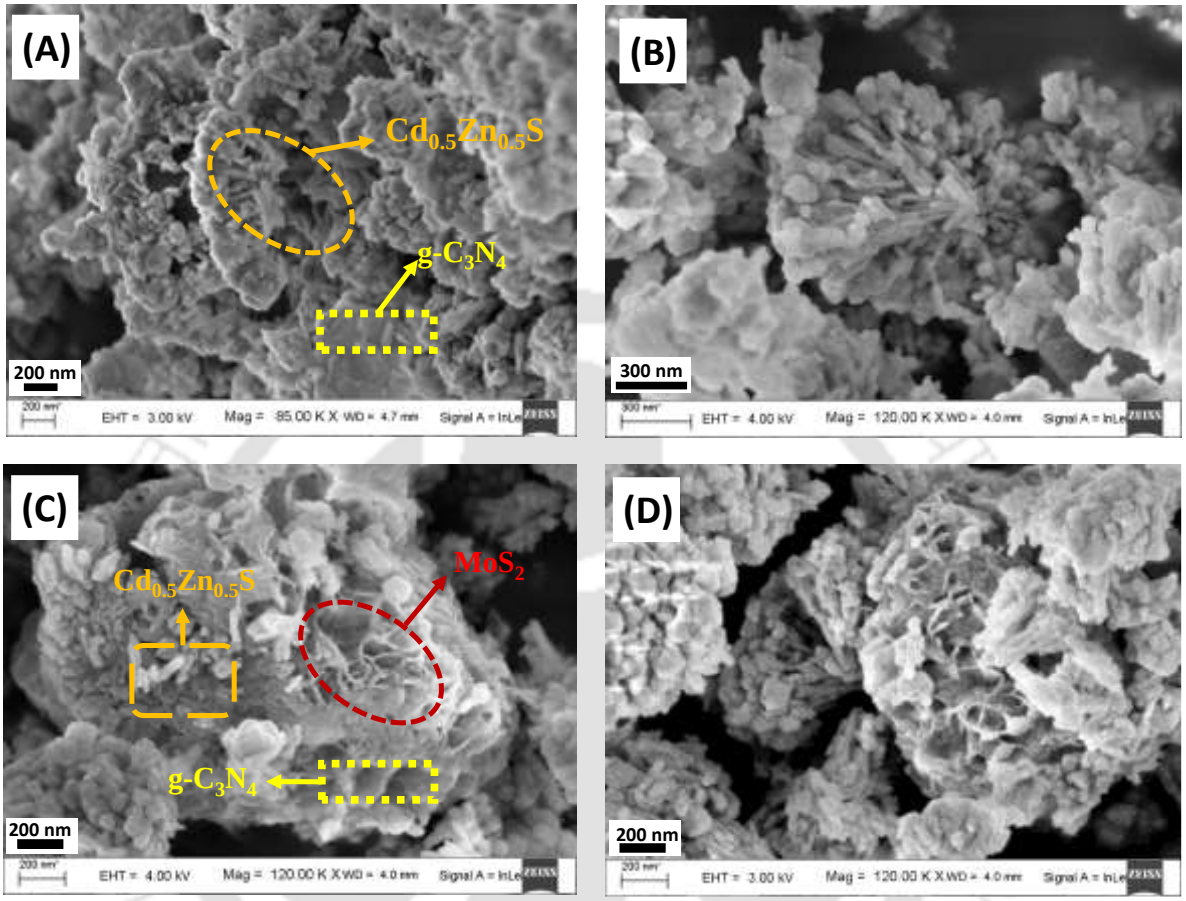

Figure 4.7: Field-emission scanning electron microscopy (FESEM) images of (A, B) $Cd_{0.5}Zn_{0.5}S$–g-C_3N_4 and (C, D) $Cd_{0.5}Zn_{0.5}S$–g-C_3N_4–MoS_2 at different magnifications.

The FESEM images of the composites are shown in **Figure 4.7**. The FESEM images of $Cd_{0.5}Zn_{0.5}S$–g-C_3N_4 in **Figure 4.7 (A)** and **Figure 4.7 (B)** show close contact among the components $Cd_{0.5}Zn_{0.5}S$ and g-C_3N_4. FESEM images of $Cd_{0.5}Zn_{0.5}S$–g-C_3N_4–MoS_2 in **Figure 4.7 (C)** and **Figure 4.7 (D)**, show the presence of all the individual components as marked in the images. It can be seen that all the components are present in a very close proximity, blending with each other thus this close contact should assist in better charge migration. Energy dispersive X-ray mapping analysis in the composite $Cd_{0.5}Zn_{0.5}S$–g-C_3N_4–MoS_2, indicates that all the elements are distributed homogeneously throughout the material in the scan area (**Figure 4.8**).

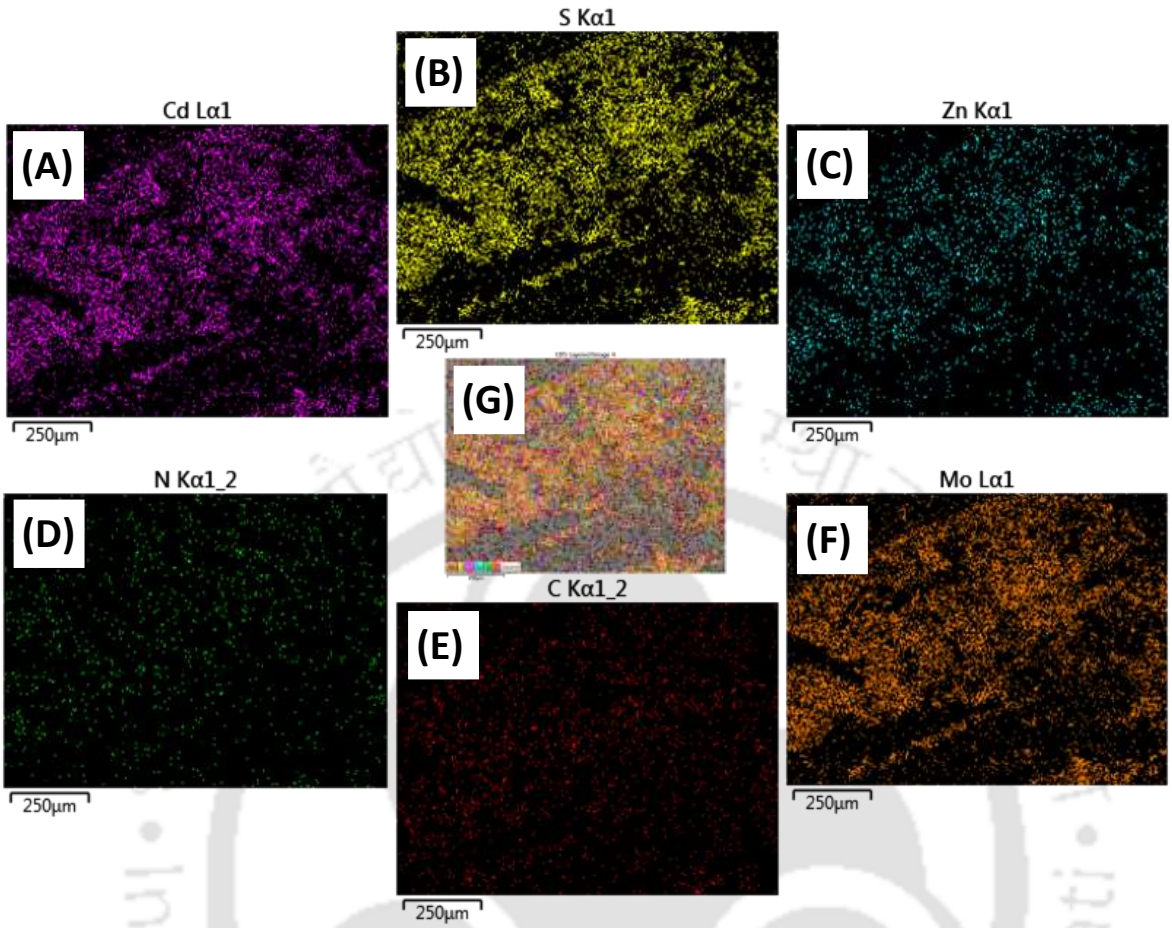

Figure 4.8: Energy-dispersive X-ray (EDX) mapping of $Cd_{0.5}Zn_{0.5}S$–g-C_3N_4–MoS_2 (G). (A), (B), (C), (D), (E) and (F) shows the homogenous elemental distribution of Cd, S, Zn, N, C and Mo, respectively in the area (G).

4.3.5 Transmission Electron Microscopy

Particle size and microstructural analysis of $Cd_{0.5}Zn_{0.5}S$–g-C_3N_4–MoS_2 was performed using Transmission Electron Microscopy (TEM) and High Resolution Transmission Electron Microscopy (HRTEM).

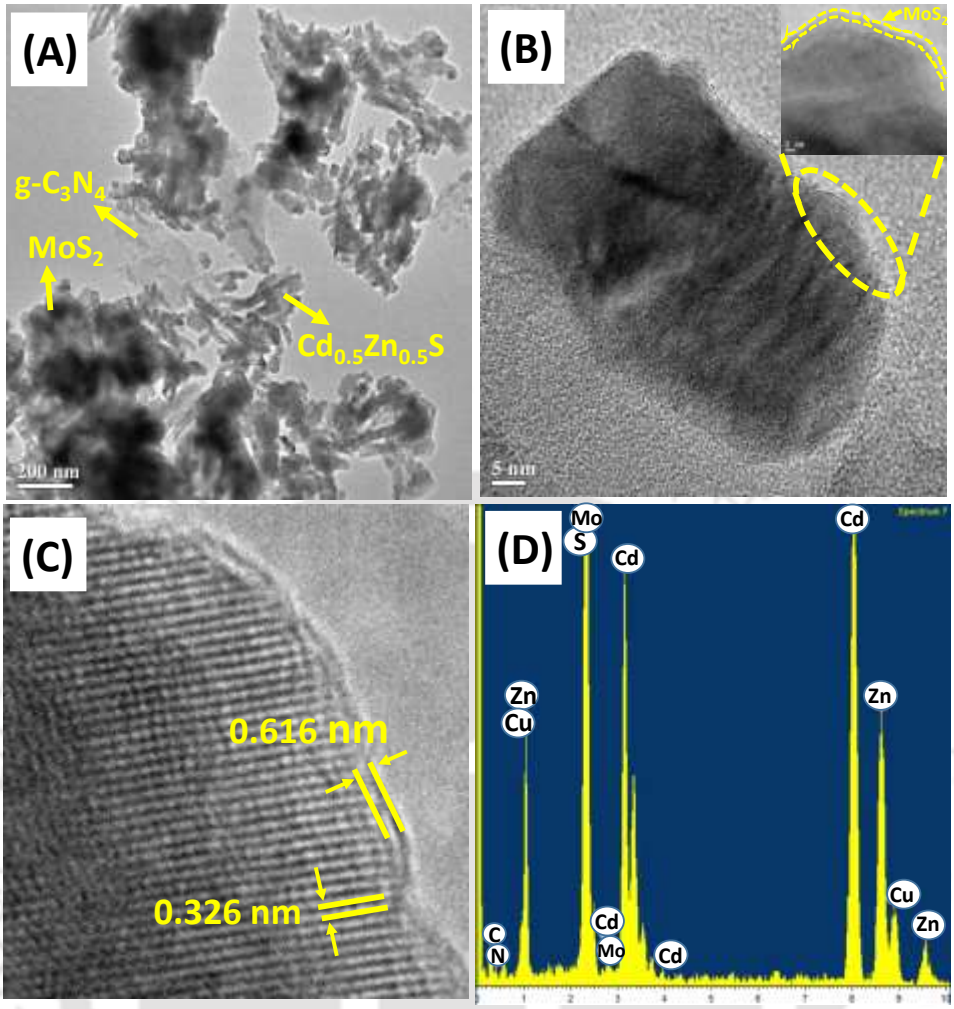

Figure 4.9: (A) Transmission electron microscopy (TEM) image of $Cd_{0.5}Zn_{0.5}S$–g-C_3N_4–MoS_2, (B) transmission electron microscopy (TEM) image of a part of $Cd_{0.5}Zn_{0.5}S$–g-C_3N_4–MoS_2 with magnified image of the highlighted portion in the inset of (B), (C) high resolution transmission electron microscopy (HRTEM) image showing the lattice fringes of $Cd_{0.5}Zn_{0.5}S$ and MoS_2 and (D) energy-dispersive X–ray (EDX) spectrum.

Consistent with FESEM images, $Cd_{0.5}Zn_{0.5}S$ was observed to be nanorod like shaped with a particle size of about 100 nm (**Figure 4.9 (A)**). g-C_3N_4 is observed as a two-dimensional nanosheet structure around the clusters of $Cd_{0.5}Zn_{0.5}S$ nanorods and MoS_2 clusters (**Figure 4.9 (A)**). A magnified image of a part of $Cd_{0.5}Zn_{0.5}S$–g-C_3N_4–MoS_2 is shown in **Figure 4.9 (B)**. The lattice fringes in the HRTEM image of $Cd_{0.5}Zn_{0.5}S$–g-C_3N_4–MoS_2 is shown in **Figure 4.9 (C)** with a d-spacing of ~ 0.32 nm which is assignable to the (101) lattice plane of hexagonal $Cd_{0.5}Zn_{0.5}S$.[57] Further, the lattice fringes with a d-spacing of ~ 0.62 nm corresponds to the (002) plane of hexagonal MoS_2.[28] Thus, **Figure 4.9 (C)** reveals the intimate

contact between $Cd_{0.5}Zn_{0.5}S$ and MoS_2, which is expected to facilitate improved charge separation, thus resulting in enhanced photocatalytic activity. The EDX spectrum (**Figure 4.9 (D)**) of the composite proves the existence of Cd, Zn, S, Mo, C and N elements (The Cu peak originates from the substrate).

4.3.6 Steady-State Photoluminescence Study

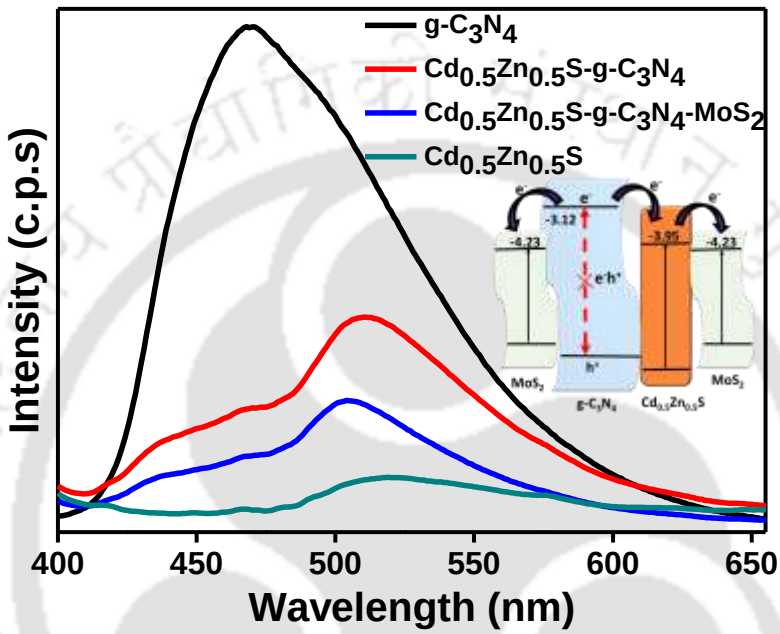

Figure 4.10: Steady–state photoluminescence (PL) spectra of $Cd_{0.5}Zn_{0.5}S$, $Cd_{0.5}Zn_{0.5}S$–g-C_3N_4, $Cd_{0.5}Zn_{0.5}S$–g-C_3N_4–MoS_2 and g-C_3N_4 at an excitation wavelength of 380 nm.

To gain insight into the excited-state electronic interaction among the components in the photocatalyst system, steady-state photoluminescence (PL) measurement was carried out. From the PL spectra in **Figure 4.10**, it is observed that, on excitation at 380 nm, g-C_3N_4, $Cd_{0.5}Zn_{0.5}S$–g-C_3N_4, $Cd_{0.5}Zn_{0.5}S$–g-C_3N_4–MoS_2 and $Cd_{0.5}Zn_{0.5}S$ emits at ~ 470 nm, ~ 510 nm, ~ 504 nm, and ~ 515 nm, respectively. Pure g-C_3N_4 has a very intense PL emission band centred at ~ 470 nm which is credited to the transition from the lone pair on the N atoms in g-C_3N_4 to its π* conduction band.[50] On introduction of $Cd_{0.5}Zn_{0.5}S$, the PL emission intensity of $Cd_{0.5}Zn_{0.5}S$–g-C_3N_4 decreases at 470 nm, likely due to charge transfer from g-C_3N_4 to $Cd_{0.5}Zn_{0.5}S$. PL from the composite is also observed at ~ 515 nm, and is consistent with emission from $Cd_{0.5}Zn_{0.5}S$. On addition of MoS_2 ($Cd_{0.5}Zn_{0.5}S$–g-C_3N_4–MoS_2), there is further quenching in the PL intensity compared to $Cd_{0.5}Zn_{0.5}S$–g-C_3N_4. Electrons from conduction band of $Cd_{0.5}Zn_{0.5}S$ and g-C_3N_4 might exhibit a faster migration to the MoS_2 sheets due to the

suitable conduction band positions. It leads to a reduction of electron density at both $Cd_{0.5}Zn_{0.5}S$ and g-C_3N_4 sites which minimizes the chances of recombination. A reasonable mechanism for photogenerated charge transfer processes that likely takes place in $Cd_{0.5}Zn_{0.5}S$–g-C_3N_4–MoS_2 is schematically shown in the inset of **Figure 4.10**.

4.3.7 Time-Resolved Photoluminescence Study

To further prove the synergistic effects of electron transfer between the materials in the composite, time-resolved photoluminescence (TRPL) spectroscopy was performed at an excitation wavelength of 375 nm and are shown in **Figure 4.11**. The TRPL decay patterns monitored at 470 nm are fitted with a tri-exponential function, which implies that multiple processes are responsible for the emission.

The average lifetime, ⟨τ⟩, was calculated using **Equation (4.1)**.[58]

$$< \tau >= \frac{\alpha_1 \tau_1^2 + \alpha_2 \tau_2^2 + \alpha_3 \tau_3^2}{\alpha_1 \tau_1 + \alpha_2 \tau_2 + \alpha_3 \tau_3} \qquad (\mathbf{4.1})$$

Table 4.2 summarizes the detailed spectroscopic results for g-C_3N_4, $Cd_{0.5}Zn_{0.5}S$-g-C_3N_4, and $Cd_{0.5}Zn_{0.5}S$-g-C_3N_4-MoS_2. From **Table 4.2**, it is observed that all the decay curves are well fitted with three components as assessed by the near unity value of χ^2. The shorter decay time is associated with radiative recombination of electron hole pairs while the higher value of decay time attributes to trap state emission. In all the three compounds, the population with short decay time (less than 4 ns) is dominant (~ 85%), which implies rapid electron hole pair recombination.[59] However, it is observed that the lifetime of all the components (τ_1, τ_2, τ_3) decrease gradually from g-C_3N_4 to $Cd_{0.5}Zn_{0.5}S$–g-C_3N_4 and $Cd_{0.5}Zn_{0.5}S$–g-C_3N_4–MoS_2. It is well known that a decrease in the lifetime (τ) value indicates more efficient separation of electrons and holes.[60-62] In order to be an efficient reduction catalyst, the lifetime of the photocatalyst is expected to be shorter in order to facilitate efficient charge transfer from the photocatalyst to co–catalyst surface.[63]

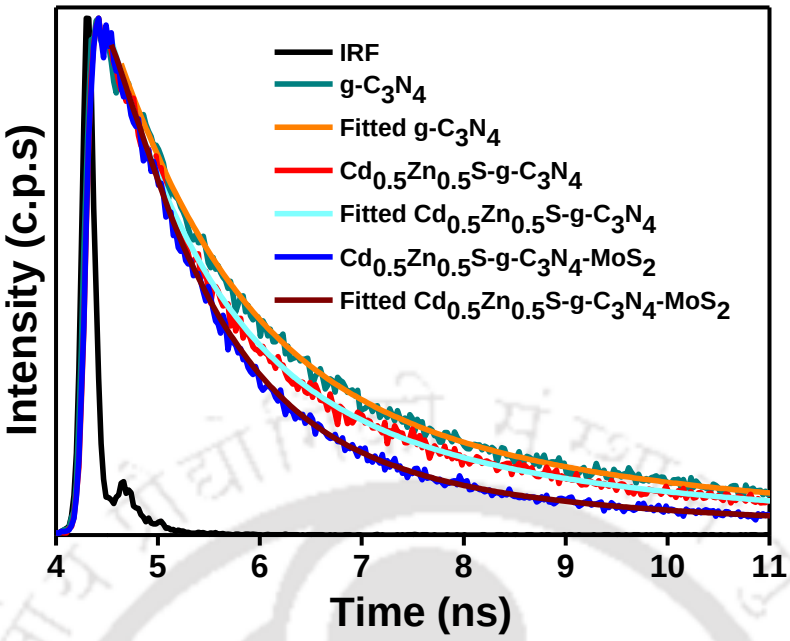

Figure 4.11: Time-resolved photoluminescence decay curves for $Cd_{0.5}Zn_{0.5}S$–g-C_3N_4–MoS_2, $Cd_{0.5}Zn_{0.5}S$–g-C_3N_4 and g-C_3N_4 (excitation wavelength = 375 nm and emission wavelength = 470 nm).

Table 4.2: Relative Percentage (α_1, α_2, α_3) (%), Excited-State Lifetime (τ_1, τ_2, τ_3), Average Exciton Lifetime $\langle\tau\rangle$ and Fitting Parameter (χ^2), for $Cd_{0.5}Zn_{0.5}S$–g-C_3N_4–MoS_2, $Cd_{0.5}Zn_{0.5}S$–g-C_3N_4 and g-C_3N_4

	α_1 (%)	α_2 (%)	α_3 (%)	τ_1 (ns)	τ_2 (ns)	τ_3(ns)	$\langle\tau\rangle$ (ns)	χ^2
g-C_3N_4	44.940	38.722	16.338	1.155	3.936	18.514	12.35	1.219
$Cd_{0.5}Zn_{0.5}S$–g-C_3N_4	47.351	37.645	15.003	0.995	3.499	16.215	10.54	1.264
$Cd_{0.5}Zn_{0.5}S$–g-C_3N_4–MoS_2	57.355	29.004	13.641	0.929	3.217	14.288	9.17	1.238

As materials are added to the composite, from the average lifetime value $\langle\tau\rangle$, calculated using **Equation (4.1)**, it is observed that the average lifetime is much shorter in $Cd_{0.5}Zn_{0.5}S$–g-C_3N_4–MoS_2 (9.17 ns) in comparison to $Cd_{0.5}Zn_{0.5}S$–g-C_3N_4 (10.54 ns) and g-

C_3N_4 (12.35 ns) which indicates an excited state electronic interaction and efficient charge separation or charge delocalisation in the composite occurs based on the bandgap energies and band alignments as shown in the inset to **Figure 4.10**.

4.3.8 Raman Spectral Analysis

To get a better insight into the microstructure of crystalline materials, Raman spectra of as-synthesized samples upon excited at 488 nm were taken. **Figure 4.12** represents the Raman spectra of $Cd_{0.5}Zn_{0.5}S$, $Cd_{0.5}Zn_{0.5}S$–g-C_3N_4 and $Cd_{0.5}Zn_{0.5}S$–g-C_3N_4–MoS_2. From the spectra it is seen that $Cd_{0.5}Zn_{0.5}S$ exhibits a 1–longitudinal optical (LO) phonon mode at 310 cm^{-1}.[65] It is observed that the 1–LO phonon peak shifts to higher wavenumbers in the composites $Cd_{0.5}Zn_{0.5}S$–g-C_3N_4 and $Cd_{0.5}Zn_{0.5}S$–g-C_3N_4–MoS_2. The shift of LO phonon Raman mode observed in the composites compared to $Cd_{0.5}Zn_{0.5}S$ may be attributed to the lattice strain that appeared at the composite system $Cd_{0.5}Zn_{0.5}S$–g-C_3N_4 and $Cd_{0.5}Zn_{0.5}S$–g-C_3N_4–MoS_2 due to the interaction among the components in the composite.[65]

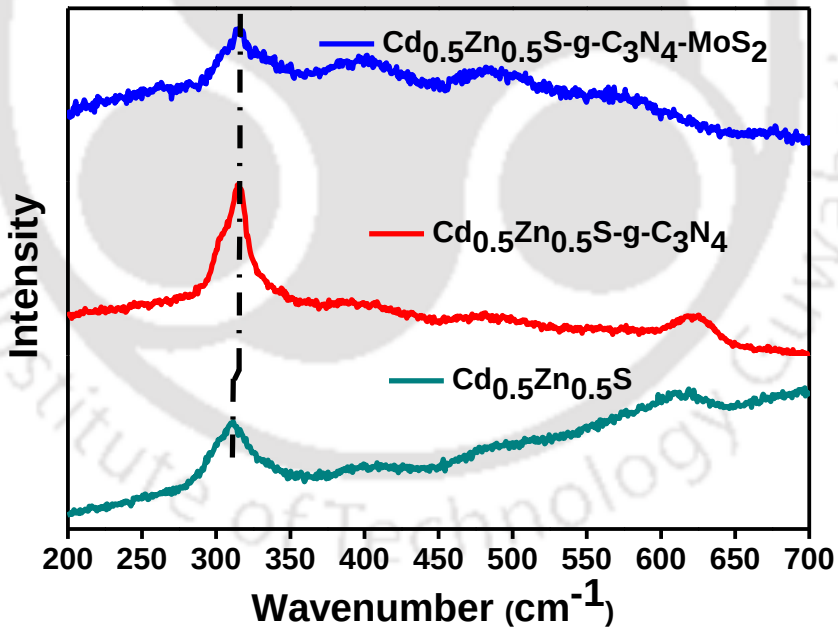

Figure 4.12: Raman spectral analysis for $Cd_{0.5}Zn_{0.5}S$, $Cd_{0.5}Zn_{0.5}S$–g-C_3N_4 and $Cd_{0.5}Zn_{0.5}S$–g-C_3N_4–MoS_2.

4.3.9 BET Surface Area Analysis

BET surface area analysis of $Cd_{0.5}Zn_{0.5}S$–g-C_3N_4–MoS_2 and $Cd_{0.5}Zn_{0.5}S$ are shown in **Figure 4.13 (A)**. $Cd_{0.5}Zn_{0.5}S$–g-C_3N_4–MoS_2 and $Cd_{0.5}Zn_{0.5}S$ show H3 hysteresis loops and exhibit type IV isotherms. Although Type–IV isotherms are typical for mesoporous materials, however, a distinct increase in adsorbate volume in the low P/P_0 region in type IV isotherms indicates the presence of micropores associated with mesopores.[66] As an inflection is observed in the isotherm of $Cd_{0.5}Zn_{0.5}S$–g-C_3N_4–MoS_2 and $Cd_{0.5}Zn_{0.5}S$ in logarithmic scale as shown in Figure **Figure 4.13 (B)**, it might infer the presence of both meso and micropores in the materials. Barrett–Joyner–Halenda (BJH) pore size distribution indicate the presence of micro to meso pores, with a higher distribution at ~ 0.6 nm and ~ 1.6 nm for $Cd_{0.5}Zn_{0.5}S$–g-C_3N_4–MoS_2 and $Cd_{0.5}Zn_{0.5}S$, respectively (inset to **Figure 4.13 (A)**). The observed BET surface area of $Cd_{0.5}Zn_{0.5}S$–g-C_3N_4–MoS_2 is ~ 16.7 m^2/g which is lower than bare $Cd_{0.5}Zn_{0.5}S$ (~ 19.1 m^2/g). The decrease of the surface area after incorporation of g-C_3N_4 and MoS_2 is consistent with loss of the small pores in $Cd_{0.5}Zn_{0.5}S$ as observed in the pore size distribution curve.

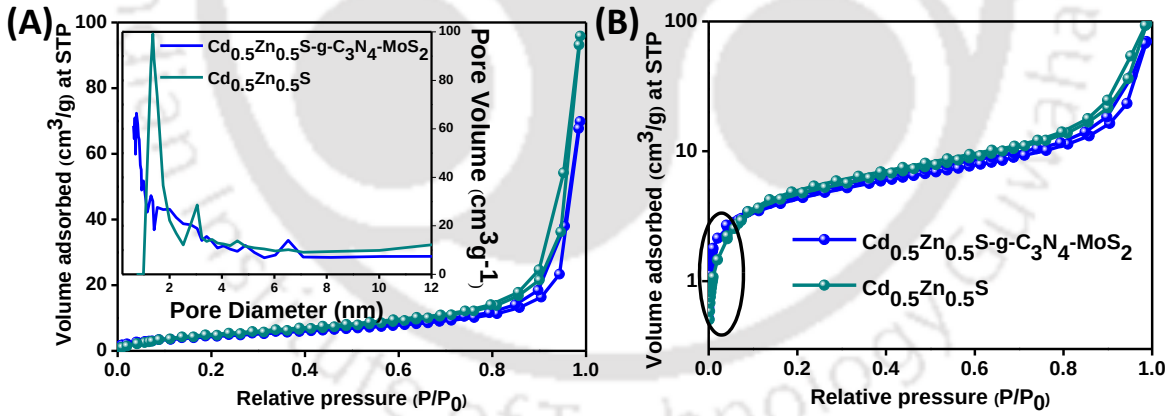

Figure 4.13: (A) Nitrogen adsorption–desorption isotherms and Barrett–Joyner–Halenda (BJH) pore size distribution plots (inset) for $Cd_{0.5}Zn_{0.5}S$–g-C_3N_4–MoS_2 and $Cd_{0.5}Zn_{0.5}S$ and (B) Points of inflection at very low P/P_0 in the isotherm plotted in logarithmic scale.

4.3.10 Photocatalytic Hydrogen Production Analysis

In order to evaluate the photocatalytic activity of the composite system, H_2 evolution was estimated in an aqueous solution containing sodium sulfite (0.1 M) and sodium sulfide

(0.1 M) as sacrificial reagent. Photocatalytic H_2 evolution by a metal sulfide semiconductor in the presence of sulfide and sulfite anions can be represented by **Equations 4.2–4.7**.[67]

$$\text{Photocatalyst} + h\nu \longrightarrow h^+_{VB} + e^-_{CB} \quad \textbf{(4.2)}$$

$$H_2O + 2e^-_{CB} \longrightarrow H_2 + 2OH^- \quad \textbf{(4.3)}$$

$$SO_3^{2-} + H_2O + 2h^+_{VB} \longrightarrow SO_4^{2-} + 2H^+ \quad \textbf{(4.4)}$$

$$2S^{2-} + 2h^+_{VB} \longrightarrow S_2^{2-} \quad \textbf{(4.5)}$$

$$S_2^{2-} + SO_3^{2-} \longrightarrow S_2O_3^{2-} + S^{2-} \quad \textbf{(4.6)}$$

$$SO_3^{2-} + S^{2-} \longrightarrow 2h^+_{VB} + S_2O_3^{2-} \quad \textbf{(4.7)}$$

The photoexcited electrons in the conduction band carries out the reduction of water to H_2. While the photogenerated holes in the valence band are consumed by SO_3^{2-} and S^{2-} and get converted into SO_4^{2-} and S_2^{2-}, respectively. The production of excess S_2^{2-} is supressed by its reaction with SO_3^{2-} to form $S_2O_3^{2-}$. Although an additional component, $S_2O_3^{2-}$, is formed in the reaction chamber, it does not compete for light absorption with the photocatalyst because it is colourless. The risk of formation of sulfur defects in $Cd_{0.5}Zn_{0.5}S$ is suppressed due to the presence of excess S^{2-} in the solution, which stabilizes the photocatalyst.[68]

To evaluate the H_2 production efficacy of the binary composite $Cd_{0.5}Zn_{0.5}S$–g-C_3N_4 in comparison to other binary combinations, we performed control experiment with $Cd_{0.5}Zn_{0.5}S$–5%MoS_2 and 30%g–C_3N_4–5%MoS_2 (both prepared by ultrasonication of the components in definite weight percentage and represented as $Cd_{0.5}Zn_{0.5}S$–MoS_2, and g-C_3N_4–MoS_2, respectively), and compared with $Cd_{0.5}Zn_{0.5}S$–g-C_3N_4 (**Figure 4.14**). It is seen that the binary composites $Cd_{0.5}Zn_{0.5}S$–MoS_2 and g-C_3N_4–MoS_2 produce H_2 at a rate of ~ 49 µmol/h/0.02g and ~ 20 µmol/h/0.02g, respectively which is lesser than $Cd_{0.5}Zn_{0.5}S$–g-C_3N_4 (~ 68 µmol/h/0.02g). Thus the binary composite of $Cd_{0.5}Zn_{0.5}S$–g-C_3N_4 was studied over the other binary composites, $Cd_{0.5}Zn_{0.5}S$–MoS_2, and g-C_3N_4–MoS_2.

The ternary composite $Cd_{0.5}Zn_{0.5}S$–g-C_3N_4–MoS_2 resulted in H_2 production from water at a rate of ~ 91 µmol/h/0.02g. The observed rate of H_2 production of $Cd_{0.5}Zn_{0.5}S$–g-C_3N_4 and $Cd_{0.5}Zn_{0.5}S$ are ~ 68 µmol/h/0.02g and ~ 30 µmol/h/0.02g, respectively (**Figure 4.15**).

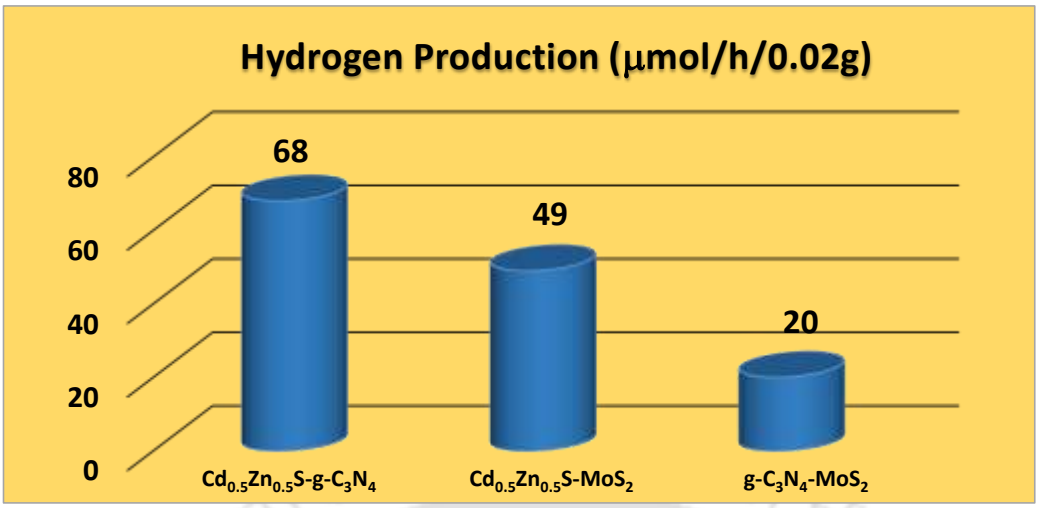

Figure 4.14: Rate of photocatalytic hydrogen evolution of $Cd_{0.5}Zn_{0.5}S$–g-C_3N_4, $Cd_{0.5}Zn_{0.5}S$–MoS_2 and g-C_3N_4–MoS_2. (Values rounded to the nearest integer)

The ternary system ($Cd_{0.5}Zn_{0.5}S$–g-C_3N_4–MoS_2) exhibited a significantly improved photocatalytic H_2 production activity compared to $Cd_{0.5}Zn_{0.5}S$–g-C_3N_4 and $Cd_{0.5}Zn_{0.5}S$. The observed trend in the rate of H_2 production can be understood by the enhanced charge separation in $Cd_{0.5}Zn_{0.5}S$–g-C_3N_4–MoS_2 owing to the electron transfers from g-C_3N_4 and $Cd_{0.5}Zn_{0.5}S$ to the H_2 evolution reaction sites of MoS_2 by virtue of its favorable band alignments.

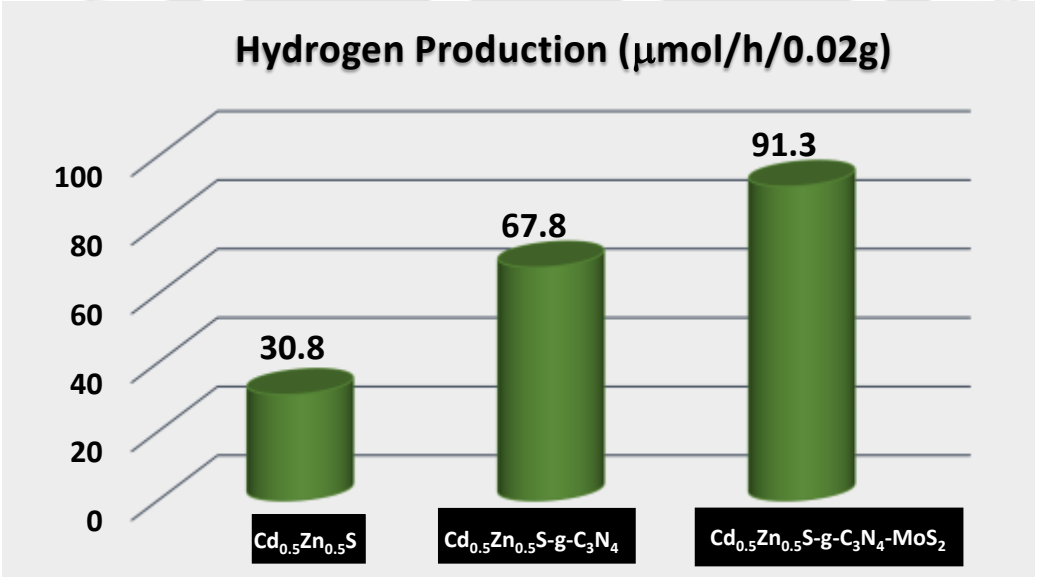

Figure 4.15: Rate of photocatalytic hydrogen evolution from $Cd_{0.5}Zn_{0.5}S$, $Cd_{0.5}Zn_{0.5}S$–g-C_3N_4, and $Cd_{0.5}Zn_{0.5}S$–g-C_3N_4–MoS_2.

The apparent quantum yield (AQY) of $Cd_{0.5}Zn_{0.5}S$–g-C_3N_4–MoS_2 was calculated at a specific wavelength of 420 nm as it lies in the maximum absorbance range of the photocatalyst and has been reported in several literature of similar system. The AQY of $Cd_{0.5}Zn_{0.5}S$–g-C_3N_4–MoS_2 was calculated to be ~ 38% at 420 nm. As the quantum efficiency is dependent on the light absorbance of the photocatalyst, it should vary in accordance with the absorbance spectra. In order to observe the effect of absorbance on the AQY, quantum efficiency was also calculated using a different band pass filter (480 nm). The AQY at 480 nm was calculated to be ~ 35%. Thus, it is seen that the quantum efficiencies goes almost in accordance with the absorbance of $Cd_{0.5}Zn_{0.5}S$–g-C_3N_4–MoS_2 as shown in **Figure 4.16**.

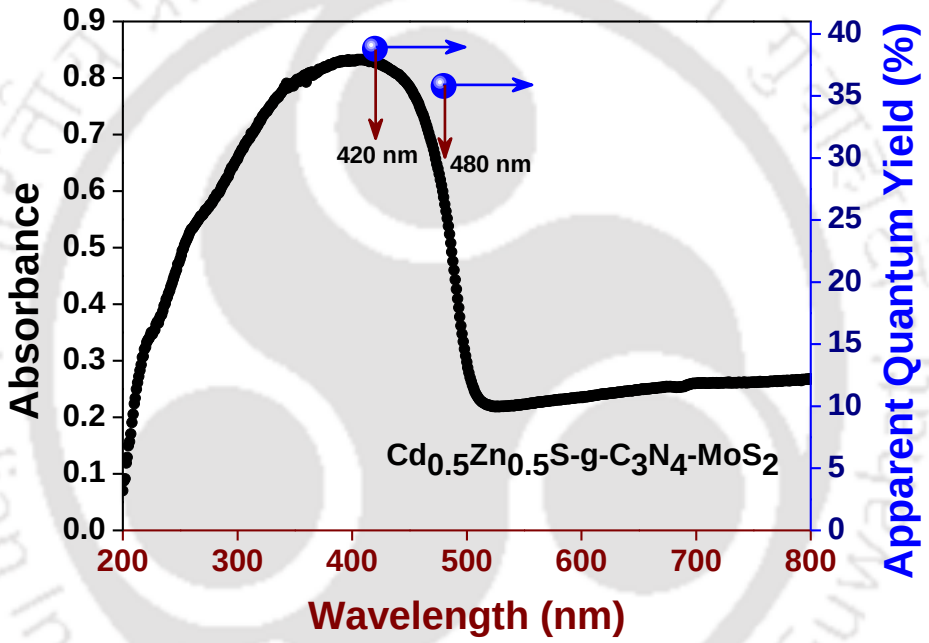

Figure 4.16: Wavelength-dependent apparent quantum yield (AQY %) for H_2 evolution of $Cd_{0.5}Zn_{0.5}S$–g-C_3N_4–MoS_2 measured at 420 nm and 480 nm.

The durability of the best performing catalyst, $Cd_{0.5}Zn_{0.5}S$–g-C_3N_4–MoS_2, is tested for three consecutive cycles. The durability of the catalyst is found to be moderate, as the amount of gas gradually decreases with repeated cycles as shown by the plot of irradiation time versus amount of gas evolved shown in **Figure 4.17**. This could be possibly due to the photocorrosion of sulfides present in all the components of our system, in due course of time. $Cd_{0.5}Zn_{0.5}S$ and the composites $Cd_{0.5}Zn_{0.5}S$–g-C_3N_4 and $Cd_{0.5}Zn_{0.5}S$–g-C_3N_4–MoS_2 showed high stability during photo irradiation. To establish the stability of the photocatalyst, the

catalysts were dispersed in 50 mL of aqueous solution of Na_2SO_3 (0.1 M) and Na_2S (0.1 M) and subjected to irradiation.

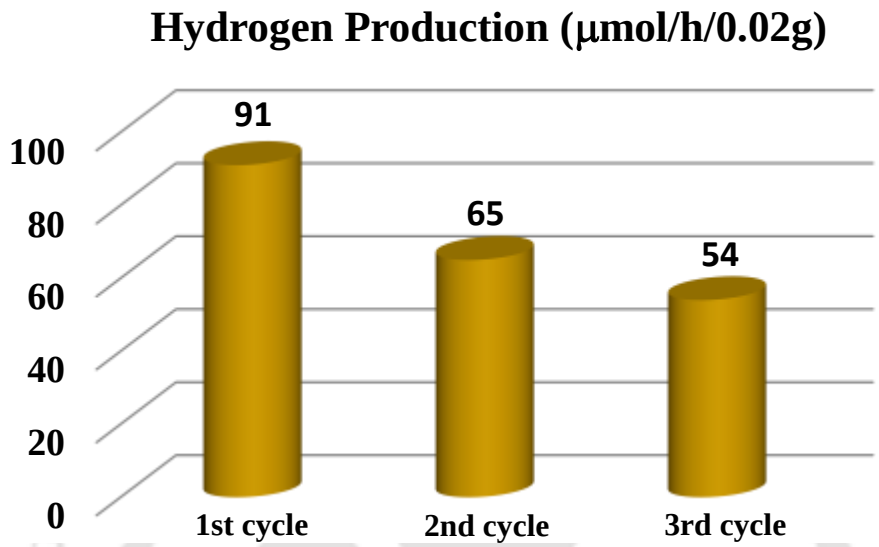

Figure 4.17: Rate of photocatalytic hydrogen evolution of $Cd_{0.5}Zn_{0.5}S$–g-C_3N_4–MoS_2 for three consecutive cycles.

PXRD of the recovered catalysts after 1h of light irradiation were recorded and this was repeated up to 2 h of irradiation. The PXRD of $Cd_{0.5}Zn_{0.5}S$, $Cd_{0.5}Zn_{0.5}S$–g-C_3N_4 and $Cd_{0.5}Zn_{0.5}S$–g-C_3N_4–MoS_2 recovered after 1 and 2 h of irradiation are shown in **Figure 4.18**. The PXRD patterns retain the crystalline phase as well as no impurity peaks are detected due to the photocatalytic treatment which proves the stability of the photocatalyst during light irradiation.

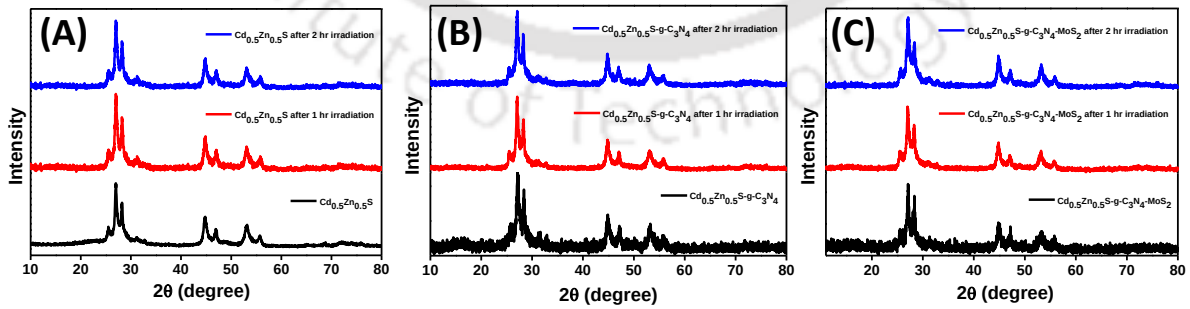

Figure 4.18: Powder X-ray diffraction of (A) $Cd_{0.5}Zn_{0.5}S$, (B) $Cd_{0.5}Zn_{0.5}S$–g-C_3N_4 and (C) $Cd_{0.5}Zn_{0.5}S$–g-C_3N_4–MoS_2 before irradiation and recorded after 1 and 2 h of irradiation.

In order to further confirm the separation efficiency, photocurrent–time measurements were carried out in an electro-chemical workstation (CHI 1120B) in a standard three-electrode configuration with a Pt wire as the counter electrode and Ag/AgCl as a reference electrode. 0.1 M Na_2SO_4 was used as the electrolyte. For the preparation of the working electrode, 10 mg finely ground sample was mixed with 25 µl Nafion solution and 200 µl ethanol to make a slurry by ultrasonication. The slurry was then drop casted over an area of 1 cm × 1 cm onto a FTO glass substrate and was dried at 50 °C for 8 h. The photocurrent-time measurement was carried out for $Cd_{0.5}Zn_{0.5}S$, $Cd_{0.5}Zn_{0.5}S$–g-C_3N_4 and $Cd_{0.5}Zn_{0.5}S$–g-C_3N_4–MoS_2 in a 20 s on-off light cycle as shown in **Figure 4.19**. The $Cd_{0.5}Zn_{0.5}S$–g-C_3N_4–MoS_2 composite exhibits a higher transient photocurrent density of 9.28 µA/cm^2 than $Cd_{0.5}Zn_{0.5}S$ with a photocurrent density of 2.52 µA/cm^2, which indicates that the separation efficiency of photogenerated charge carriers is significantly improved at the semiconductor electrolyte interface, thus extending the lifetime of the electron–hole pairs effectively.

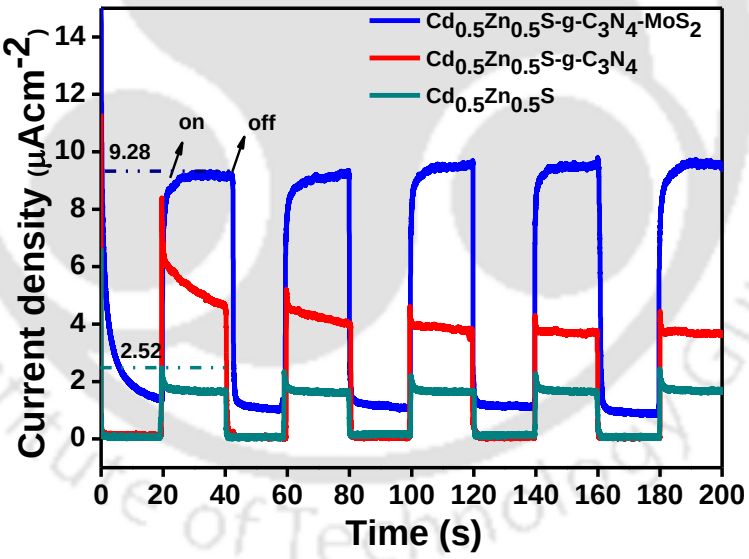

Figure 4.19: Photocurrent response of $Cd_{0.5}Zn_{0.5}S$, $Cd_{0.5}Zn_{0.5}S$–g-C_3N_4 and $Cd_{0.5}Zn_{0.5}S$–g-C_3N_4-MoS_2.

4.3.11 Photocatalytic Dye Degradation Analysis

Apart from efficient H_2 production, the as–synthesised composite also proved effective for degradation of organic pollutants frequently found in industrial waste water. We chose Rhodamine B as the model system to study degradation kinetics.

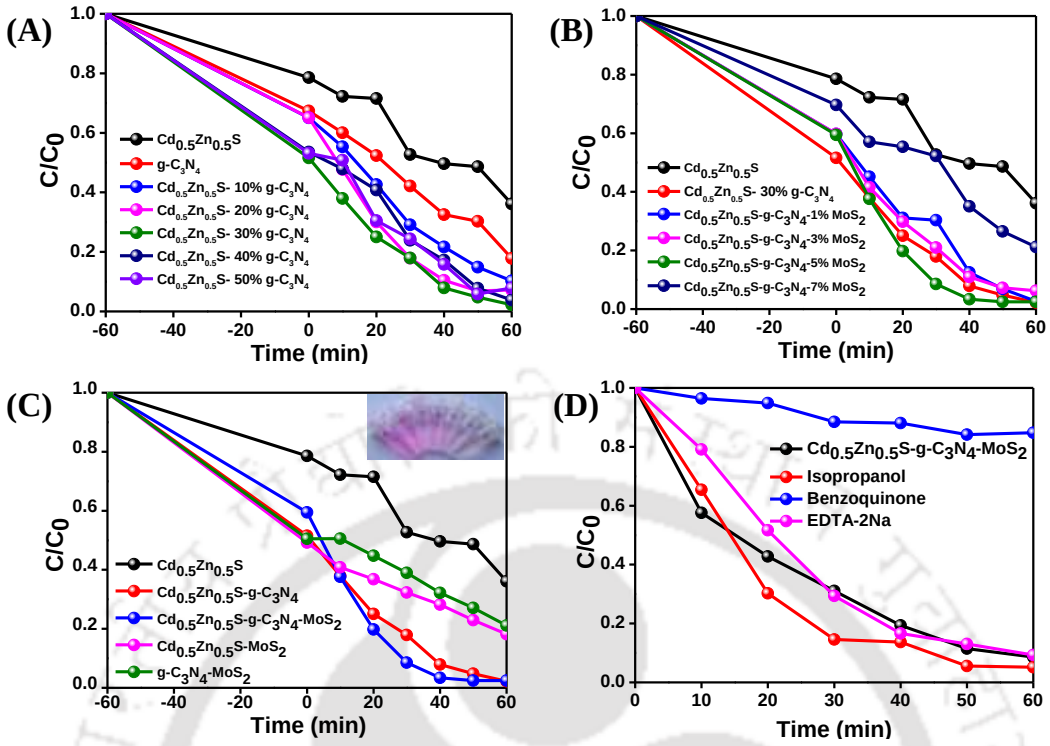

Figure 4.20: (A) C/C_0 versus time (min) plot of $Cd_{0.5}Zn_{0.5}S$, g-C_3N_4 and $Cd_{0.5}Zn_{0.5}S$–*x*%g-C_3N_4 (*x* = 10, 20, 30, 40, 50), (B) C/C_0 versus time (min) plot of $Cd_{0.5}Zn_{0.5}S$, g-C_3N_4 and $Cd_{0.5}Zn_{0.5}S$– 30%g-C_3N_4 and $Cd_{0.5}Zn_{0.5}S$–g-C_3N_4–*x*%MoS_2 (*x* = 1, 3, 5, 7), (C) Plot of C/C_0 as a function of time (min) for $Cd_{0.5}Zn_{0.5}S$, $Cd_{0.5}Zn_{0.5}S$–g-C_3N_4, and $Cd_{0.5}Zn_{0.5}S$–g-C_3N_4–MoS_2 and (D) Rate of degradation of Rhodamine B in the presence of different reactive species scavengers.

A degradation study for all composites with different weight percentage of g-C_3N_4 and MoS_2, $Cd_{0.5}Zn_{0.5}S$–*x*%g-C_3N_4 (*x* = 10, 20, 30, 40, 50) and $Cd_{0.5}Zn_{0.5}S$–30%g-C_3N_4–*x*%MoS_2 (*x* = 1, 3, 5, 7) are shown in **Figure 4.20 (A)** and **Figure 4.20 (B)**, respectively. From **Figure 4.20 (A)**, it is observed that $Cd_{0.5}Zn_{0.5}S$–30%g-C_3N_4 exhibits the maximum degradation rate among the $Cd_{0.5}Zn_{0.5}S$–*x*%g-C_3N_4 (*x* = 10, 20, 30, 40, 50) composites. Thus, $Cd_{0.5}Zn_{0.5}S$–30%g-C_3N_4–*x*%MoS_2 composites were further studied. The degradation efficiencies of $Cd_{0.5}Zn_{0.5}S$–g-C_3N_4–*x*%MoS_2 (*x* = 1, 3, 5, 7) are shown in **Figure 4.20 (B)**, where $Cd_{0.5}Zn_{0.5}S$–g-C_3N_4–5%MoS_2 shows the best performance in degradation of Rhodamine B. Normalised concentration (C/C_0) over time for $Cd_{0.5}Zn_{0.5}S$–g-C_3N_4–MoS_2, $Cd_{0.5}Zn_{0.5}S$–g-C_3N_4, and $Cd_{0.5}Zn_{0.5}S$ are compared with the other possible binary composition, $Cd_{0.5}Zn_{0.5}S$–MoS_2, and g-C_3N_4–MoS_2 (**Figure 4.20 (C)**), where $Cd_{0.5}Zn_{0.5}S$–g-C_3N_4–MoS_2 was found to be the most effective. By 30 min, the percent degradation is ~ 33%,

~ 65%, and ~ 86% for $Cd_{0.5}Zn_{0.5}S$, $Cd_{0.5}Zn_{0.5}S$–g-C_3N_4, and $Cd_{0.5}Zn_{0.5}S$–g-C_3N_4–MoS_2, respectively. Active species trapping experiments were conducted in order to determine the primary active species involved in the degradation process. As seen in **Figure 4.20 (D)**, a significant decrease in the rate was observed after the addition of benzoquinone (scavenger of $O_2^{\bullet-}$), demonstrating that $O_2^{\bullet-}$ is the main active species involved in the RhB photooxidation process. However, isopropanol (scavenger of $OH^{\bullet}$) and EDTA-2Na (scavenger of holes) had almost no effect on RhB degradation as the rate of degradation is not much varied with the introduction of these scavengers which proves that •OH and h^+ do not have a significant contribution in the photodegradation process.

Table 4.3: Average efficiency (%) of Photocatalytic dye degradation of all the as synthesized compounds

System	Average efficiency (%)
$Cd_{0.5}Zn_{0.5}S$	57.7
$Cd_{0.5}Zn_{0.5}S$–10%g-C_3N_4	87.32
$Cd_{0.5}Zn_{0.5}S$–20%g-C_3N_4	87.96
$Cd_{0.5}Zn_{0.5}S$–30%g-C_3N_4	93.77
$Cd_{0.5}Zn_{0.5}S$–40%g-C_3N_4	92.57
$Cd_{0.5}Zn_{0.5}S$–50%g-C_3N_4	90.43
$Cd_{0.5}Zn_{0.5}S$–g-C_3N_4–1% MoS_2	93.50
$Cd_{0.5}Zn_{0.5}S$–g-C_3N_4–3% MoS_2	90.49
$Cd_{0.5}Zn_{0.5}S$–g-C_3N_4–5% MoS_2	94.01
$Cd_{0.5}Zn_{0.5}S$–g-C_3N_4–7% MoS_2	76.01

In order to minimize the possibility of manual and experimental error at various steps, the dye degradation efficiency (%) of all the compositions along with the bare counterpart are calculated by carrying out duplicate set and considered the average efficiency (%). The results are tabulated in **Table 4.3**. A comparative study of dye degradation ability of different $Cd_xZn_{1-x}S$–based systems along with our materials, are presented in **Table 4.5**.

4.3.12 Determination of Band Structure and Charge Transfer Mechanism

To determine the conduction band minima of $Cd_{0.5}Zn_{0.5}S$, g-C_3N_4 and MoS_2, cyclic voltammetry scan was carried out for all the samples using CH1120B potentiostat. For cyclic voltammetry scan, $Cd_{0.5}Zn_{0.5}S$, g-C_3N_4 and MoS_2 were dispersed individually in ethanol and were spin coated on fluorine doped tin oxide (FTO) coated glass substrate which were used as working electrode in a three electrode configuration. Pt wire was used as counter electrode and Ag/AgCl as reference electrode with deoxygenated 0.1 M tetrabutylammonium hexafluorophosphate ($TBAPF_6$) in acetonitrile as electrolyte. The scan rate was fixed at 50 mV/s. The conduction band minimum (CBM) of the individual components, $Cd_{0.5}Zn_{0.5}S$, g-C_3N_4 and MoS_2, determined by cyclic voltammetry (CV) is shown in **Figure 4.21**.[69] The electron transfer mediated through conduction band edge and valence band edge positions, gives rise to cathodic (V_c) and anodic peaks (V_a), respectively in a cyclic voltammogram. The CBM was determined from the cathodic peak (E vs Ag/AgCl). The values (E vs vacuum) are obtained from the equation, $E_{LUMO} = -e\,[E_{red}^{onset} + 4.5]$. From the CV data, the cathodic peak positions of $Cd_{0.5}Zn_{0.5}S$, g-C_3N_4 and MoS_2 are observed at -0.55V, -1.38V and -0.27 V against an Ag/AgCl electrode, which corresponds to the CBM of the respective material. The CBM of the electrodes were estimated to be -3.95 eV, -3.12 eV and -4.23 eV, respectively against vacuum level. The band gap (E_g) of all the compounds are determined from Tauc Plot to be 2.35 eV, 2.7 eV and 1.5 eV for $Cd_{0.5}Zn_{0.5}S$, g-C_3N_4 and MoS_2, respectively. The valence band maximum is calculated using the relation, $E_{VB} = E_{CB} + E_g$, where E_{VB} is the valence band maximum, E_{CB} is the conduction band minimum and E_g is the bandgap energy of the material. Thus, the E_{VB} values for $Cd_{0.5}Zn_{0.5}S$, g-C_3N_4 and MoS_2 are calculated to be -6.3 eV, -5.82 eV and -5.73 eV, respectively (E vs vacuum).

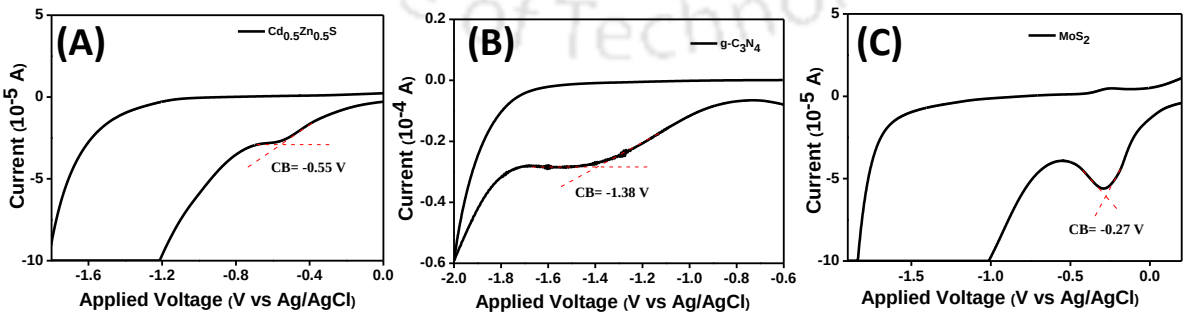

Figure 4.21: Cyclic voltammetry scan of (A) $Cd_{0.5}Zn_{0.5}S$, (B) g-C_3N_4 and (C) MoS_2.

Based on the calculated valence band maxima, conduction band minima and the band gap of the individual components, band structure of the composite is determined. The suitable band positions and possible charge transfer pathways between the components in the $Cd_{0.5}Zn_{0.5}S$–g-C_3N_4–MoS_2 composite is schematically shown in **Figure 4.22**. From the figure it is observed that the photogenerated electrons in g-C_3N_4 and $Cd_{0.5}Zn_{0.5}S$ find a facile transfer pathway to the co–catalytic sites of MoS_2, thus facilitating a better separation and prevention of recombination which is responsible for the observed high rate of photocatalytic activity in the composite.

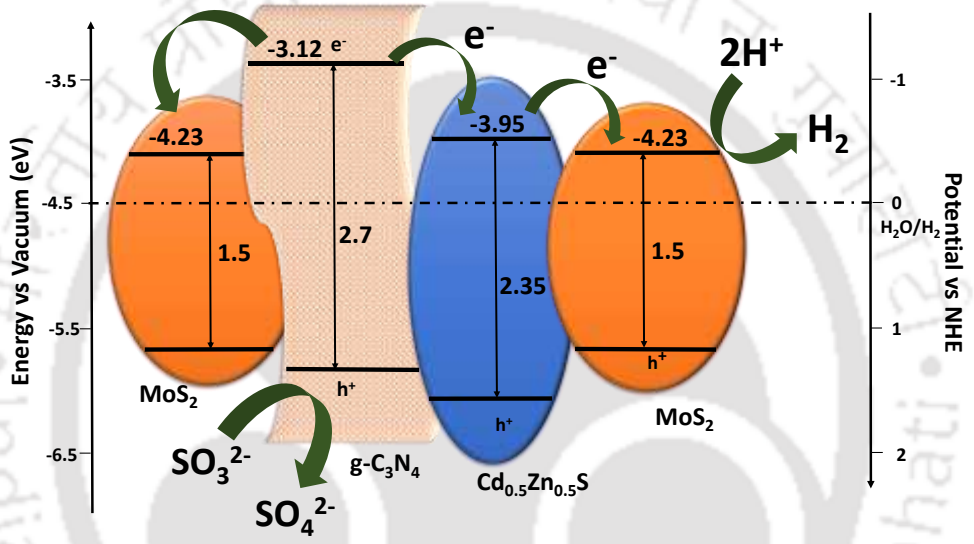

Figure 4.22: Band alignment and probable charge-transfer pathways among the components in $Cd_{0.5}Zn_{0.5}S$–g-C_3N_4–MoS_2 composite

Table 4.4: An overview of the present scenario of some $Cd_xZn_{1-x}S$ based systems and their binary composite with g-C_3N_4 or different co–catalyst in terms of rate of hydrogen production and Apparent Quantum Yield (AQY) along with the system discussed in the chapter

Sample	Apparent Quantum Yield (AQY) (%)	Rate of hydrogen production (mmol/h/g)	Reference
$Zn_{0.5}Cd_{0.5}S$	30.4 (at 420 nm)	1.097	43
$Zn_{0.5}Cd_{0.5}S$	9.6 (at 420 nm)	7.42	70

$Cd_{0.5}Zn_{0.5}S$	43 (at 425 nm)	1.79	9
$Cd_{0.2}Zn_{0.8}S$	16.2 (at 420 nm)	3.43	71
$Cd_{1-x}Zn_xS$ (x = 0.2)	10.23 (at 420 nm)	0.180 (amount of catalyst not disclosed)	45
$Zn_{0.5}Cd_{0.5}S$ porous nanosheets	-	1.67	72
$Cd_{0.57}Zn_{0.43}S$	-	1.76	73
$Cd_{0.5}Zn_{0.5}S$ 32 wt% @C_3N_4	46.65 (at 450 nm)	33.41	25
$Cd_{0.2}Zn_{0.8}S$/g-C_3N_4	-	0.208 (amount of catalyst not disclosed)	27
$Zn_{0.2}Cd_{0.8}S$/MoS_2 3%	-	0.42	41
MoS_2- $Cd_{0.5}Zn_{0.5}S$	1.34 (at 420 nm)	12.3	40
AuPd/ $Cd_{0.5}Zn_{0.5}S$	-	3.65	35
$Cd_{0.2}Zn_{0.8}S$ 1 wt% Pt on $Cd_{0.2}Zn_{0.8}S$	-	1.8 5	33
Pt-RuS_2-$Cd_{0.5}Zn_{0.5}S$	4 (under day light fluorescent lamp)	0.72	36
$Zn_{0.5}Cd_{0.5}S$@MoS_2/RGO	-	2.31	74
$Cd_{0.8}Zn_{0.2}S$/MoS_2/graphene	-	2.97	48
$Cd_{0.62}Zn_{0.16}S$	2.17 (under UV irradiation)	16.320	75
$Cd_{0.5}Zn_{0.5}S$/C_3N_4	37 (at 425 nm)	0.928 (amount of catalyst not disclosed)	26
$Cd_{0.44}Zn_{0.56}S$	-	2.640	76
$Cd_{0.5}Zn_{0.5}S$–g-C_3N_4–MoS_2	**38 (at 420 nm)**	**4.5 (under visible light irradiation)**	**This work**

Table 4.5: An overview of dye degradation ability of different $Cd_xZn_{1-x}S$ based systems along with our system

System	Initial concentration of dye solution	Dye Degradation efficiency	Reference
$Zn_{0.4}Cd_{0.6}S$	5 mg/L	98.7% RhB degradation in 180 min	77
$Zn_{0.28}Cd_{0.72}S$	6.1×10^{-5} mol/L	96% methyl orange degradation after 6 h of irradiation	78
$Cd_{0.2}Zn_{0.8}S$/g-C_3N_4 (20%)	10 mg /L	95.8% RhB degradation after 180 min irradiation	27
0.1C_3N_4/ $Zn_{0.8}Cd_{0.2}S$	2.0×10^{-5} mol/L	97.9% degradation of RhB within 90 min	79
$Zn_{0.8}Cd_{0.2}S$/ g-C_3N_4	10 mg/L	99.8% degradation of Methylene Blue in 180 min irradiation	80
$Cd_{0.5}Zn_{0.5}S$–g-C_3N_4–MoS_2	**10^{-5} mol/L**	**96% degradation of RhB in 60 min**	**This Work**

4.4 CONCLUSION

We have synthesized $Cd_{0.5}Zn_{0.5}S$, g-C_3N_4, and MoS_2 by simple synthetic procedures. By ultrasonicating these three components in definite weight percentage, we developed a noble-metal-free ternary composite $Cd_{0.5}Zn_{0.5}S$–g-C_3N_4–MoS_2. The photocatalytic efficiency of the ternary composite was studied by monitoring H_2 and dye degradation during illumination. Addition of g-C_3N_4 and both g-C_3N_4 and MoS_2 increase the rate of H_2 production (~ 68 μmol/h/0.02g and ~ 91 μmol/h/0.02g, respectively) compared to bare $Cd_{0.5}Zn_{0.5}S$ (~ 31 μmol/h/0.02g). The significant improvement of photocatalytic properties in the ternary composite can mainly be credited to the enhanced interfacial charge transfer of electrons in the composite system leading to a decrease in the photoinduced charge

recombination and hence an increased number of electrons available for reaction at the active sites. This conclusion was supported by extensive experimental techniques like electron microscopy images, photoluminescence data, XPS analysis etc.

4.5 REFERENCES

1. H. J. Yan, J. H. Yang, G. J. Ma, G. P. Wu, X. Zong, Z. B. Lei, J. Y. Shi and C. Li, *J. Catal*., 2009, **266**, 165.
2. W. Zhang, Y. B. Wang, Z. Wang, Z. Y. Zhong and R. Xu, *Chem. Commun*., 2010, **46**, 7631.
3. N. Bao, L. Shen, T. Takata and K. Domen, *Chem. Mater*., 2008, **20**, 110.
4. B. Girginer, G. Galli, E. Chiellini and N. Bicak, *Int. J. Hydrogen Energy*, 2009, **34**, 1176.
5. D. Jing and L. Guo, *J. Phys. Chem. B*, 2006, **110**, 11139.
6. K. P. Acharya, R. S. Khnayzer, T. O'Connor, G. Diederich, M. Kirsanova, A. Klinkova, D. Roth, E. Kinder, M. Imboden and M. Zamkov, *Nano Lett*., 2011, **11**, 2919.
7. L. Huang, X. Wang, J. Yang, G. Liu, J. Han and C. Li, *J. Phys. Chem. C*, 2013, **117**, 11584.
8. Y. Chen and L. Guo, *J. Mater. Chem.*, 2012, **22**, 7507.
9. M. Liu, L. Wang, G. Lu, X. Yao and L. Guo, *Energy Environ. Sci*., 2011, **4**, 1372.
10. Z. Zhang, K. Liu, Z. Feng, Y. Bao and B. Dong, *Sci. Rep*., 2016, **6**, 19221.
11. S. W. Cao, X. F. Liu, Y. P. Yuan, Z. Y. Zhang, J. Fang, S. C. J. Loo, J. Barber, T. C. Sumb and C. Xue, *Phys. Chem. Chem. Phys.*, 2013, **15**, 18363.
12. J. Liu, Y. Liu, N. Liu, Y. Han, X. Zhang, H. Huang, Y. Lifshitz, S. T. Lee, J. Zhong and Z. Kang, *Science*, 2015, **347**, 970.
13. S. Cao and J. Yu, *J. Phys. Chem. Lett*., 2014, **5**, 2101.
14. Y.-P. Yuan, L.-S. Yin, S.-W. Cao, L.-N. Gu, G.-S. Xu, P. Du, H. Chai, Y.-S. Liao and C. Xue, *Green Chem.*, 2014, **16**, 4663.
15. S. Cao, J. Low, J. Yu and M. Jaroniec, *Adv. Mater.*, 2015, **27**, 2150.
16. C. S. Pan and Y. F. Zhu, *Catal. Sci. Technol.*, 2015, **5**, 3071.
17. X. Chen, S. Shen, L. Guo and S. S. Mao, *Chem. Rev.*, 2010, **110**, 6503.

18. W. Tian, Q. Shen, N. Li and J. Zhou, *RSC Adv*., 2016, **6**, 25568.
19. Y. Hou, Z. H. Wen, S. M. Cui, X. R. Guo and J. H. Chen, *Adv. Mater.*, 2013, **25**, 6291.
20. Q. Li, N. Zhang, Y. Yang, G. Z. Wang and D. H. L. Ng, *Langmuir*, 2014, **30**, 8965.
21. K. Katsumata, R. Motoyoshi, N. Matsushita and K. Okada, *J. Hazard. Mater.*, 2013, **260**, 475.
22. G. Gogoi, S. Arora, N. Vinothkumar, M. De and M. Qureshi, *RSC Adv.*, 2015, **5**, 40475.
23. S. N. Zu, Z. Y. Wang, B. Liu, X. P. Fan and G. D. Qian, *J. Alloys Compd.*, 2009, **476**, 689.
24. X. H. Zhang, D. W. Jing, M. C. Liu and L. J. Guo, *Catal. Commun.*, 2008, **9**, 1720.
25. L. Yao, D. Wei, Y. Ni, D. Yan and C. Hu, *Nano Energy*, 2016, **26**, 248.
26. X. Wang, J. Chen, X. Guan and L. Guo, *Int. J. Hydrogen Energy*, 2015, **40**, 7546.
27. H. Liu, Z. T. Jin, and Z. Z. Xu, *Dalton Trans.*, 2015, **44**, 14368.
28. X. Zong, H. Yan, G. Wu, G. Ma, F. Wen, L. Wang and C. Li, *J. Am. Chem. Soc.*, 2008, **130**, 7176.
29. K. Maeda, K. Teramura, N. Saito, Y. Inoue and K. Domen, *J. Catal.*, 2006, **243**, 303.
30. K. Teramura, K. Maeda, T. Saito, T. Takata, N. Saito, Y. Inoue and K. Domen, *J. Phys. Chem. B*, 2006, **110**, 4500.
31. M. Liu, W. You, Z. Lei, G. Zhou, G. Yang, G. Wu, G. Ma, G. Luan, T. Takata, M. Hara, K. Domen and C. Li, *Chem. Commun.*, 2004, **19**, 2192.
32. K. Maeda, K. Teramura, D. Lu, T. Takata, N. Saito, Y. Inoue and K. Domen, *Nature*, 2006, **440**, 295.
33. J. Wang, B. Li, J. Z. Chen, L. Li, J. H. Zhao and Z. P. Zhu, *J. Alloys Compd.*, 2013, **578**, 571.
34. X. Ma, Q. Jiang, W. Guo, M. Zheng, W. Xu, F. Maa and B. Hou, *RSC Adv.*, 2016, **6**, 28263.
35. L. Wu, J. Gong, L. Ge, C. Han, S. Fang, Y. Xin, Y. Li and Y. Lu, *Int. J. Hydrogen Energy*, 2016, **41**, 14704.

36. A. P. Gaikwad, D. Tyagi, C. A. Betty and R. Sasikala, *Appl. Catal. A*, 2016, **517**, 91.
37. H. Wang, Y. Li, D.; Shu, X. Chen, X. Liu, X. Wang, J. Zhang and H. Wang, *Int. J. Energy Res*., 2016, **40**, 1280.
38. F. A. Frame and F. E. Osterloh, *J. Phys. Chem. C*, 2010, **114**, 10628.
39. Y.-F. Zhao, Z.-Y. Yang, Y.-X. Zhang, L. Jing, X. Guo, Z. Ke, P. Hu, G. Wang, Y.-M. Yan and K.-N. Sun, *J. Phys. Chem. C*, 2014, **118**, 14238.
40. S. Zhao, J. Huang, Q. Huo, X. Zhou and W. Tu, *J. Mater. Chem. A*, 2016, **4**, 193.
41. M. Nguyen, P. D. Tran, S. S. Pramana, R. L. Lee, S. K. Batabyal, N. Mathews, L. H. Wong and M. Graetzel, *Nanoscale*, 2013, **5**, 1479.
42. H. Du, H. –L. Guo, Y.-N. Liu, X. Xie, K. Liang, X. Zhou, X. Wang and A.-W. Xu, *ACS Appl. Mater. Interface*, 2016, **8**, 4023.
43. Y. Wang, J. Wu, J. Zheng and R. Xu, *Catal. Sci. Technol.*, 2011, **1**, 940.
44. Y. Tian, X. Zhao, L. Shen, F. Meng, L. Tang, Y. Deng and Z. Wang, *Materials Letters*, 2006, **60**, 527.
45. K. Zhang, D. Jing, C. Xing and L. Guo., *Int. J. Hydrogen Energy*, 2007, **32**, 4685.
46. J. D. Bryan, D. A. Schwartz and D. R. Gamelin, *J. Nanosci. Nanotechnol.*, 2005, **5**, 1472.
47. G. Q. Ren, Z. Lin, C. Wang, W. Z. Liu, J. Zhang, F. Huang and J. K. Liang, *Nanotechnology*, 2007, **18**, 35705.
48. R. Du, Y. Zhang, B. Li, X. Yu, H. Liu, X. An and J. Qu, *Phys. Chem. Chem. Phys*., 2016, **18**, 16208.
49. L. Yang, X. Wang, Y. Liu, Z. Yu, R. Li and J. Qiu, *Catal. Sci. Technol.*, 2017, **7**, 693.
50. Y. Zhang, Q. Pan, G. Chai, M. Liang, G. Dong, Q. Zhang and J. Qiu, *Sci. Rep.*, 2013, **3**, 1943.
51. H. Li, K. Yu, C. Li, Z. Tang, B. Guo, X. Lei, H. Fu and Z. Zhu, *Sci. Rep.*, 2015, **5**, 18730.
52. V. O. Koroteev, L. G. Bulusheva, A. V. Okotrub, N. F. Yudanov and D. V. Vyalikh, *Phys. Status Solidi B*, 2011, **248**, 2740.

53. S. Sperinck, T. Becker, K. Wright and W. R. Richmond, *J. Inclusion Phenom. Macrocyclic Chem.*, 2009, **65**, 89.
54. S. H. Yu, Y. S. Wu, J. Yang, Z. H. Han, Y. Xie, Y. T. Qian and X. M. Liu, *Chem. Mater.*, 1998, **10**, 2309.
55. L. Karimi, S. Zohoori and M. E. Yazdanshenas, *J. Saudi Chem. Soc.*, 2014, **18**, 581.
56. T. F. Jaramillo, K. P. Jørgensen, J. Bonde, J. H. Nielsen, S. Horch and I. Chorkendorff, *Science*, 2007, **317**, 100.
57. Q. Li, H. Meng, J. G. Yu, W. Xiao, Y. Q. Zheng and J. Wang, *Chem. Eur. J.*, 2014, **20**, 1176.
58. A. Kongkanand, K. Tvrdy, K. Takechi, M. Kuno and P. V. Kamat, *J. Am. Chem. Soc.*, 2008, **130**, 4007.
59. P. Niu, G. Liu and H. M. Cheng, *J. Phys. Chem. C*, 2012, **116**, 11013.
60. C. Liu, Y. Zhang, F. Dong, A. H. Reshak, L. Ye, N. Pinna, C. Zeng, T. Zhang and H. Huang, *Appl. Catal., B*, 2017, **203**, 465.
61. H. W. Huang, K. Xiao, N. Tian, F. Dong, T. R. Zhang, X. Du and Y. H. Zhang, *J. Mater. Chem. A*, 2017, **5**, 17452.
62. N. Tian, Y. H. Zhang, X. W. Li, K. Xiao, X. Du, F. Dong, G. I. N. Waterhouse, T. R. Zhang and H. W. Huang, *Nano Energy*, 2017, **38**, 72.
63. C. Y. Liu, H. W. Huang, L. Q. Ye, S. X. Yu, N. Tian, X. Du, T. R. Zhang and Y. H. Zhang, *Nano Energy*, 2017, **41**, 738.
64. S. Sahoo, S. Dhara, V. Sivasubramanian, S. Kalavathi and A. K. Arora, *J. Raman Spectrosc.*, 2009, **40**, 1050.
65. P. Jing, J. Zheng, M. Ikezawa, X. Liu, S. Lv, X. Kong, J. Zhao and Y. Masumoto, *J. Phys. Chem. C*, 2009, **113**, 13545.
66. S. Storck, H. Bretinger and W. F. Maier, *Appl. Catal., A*, 1998, **174**, 137.
67. B. Chai, T. Peng, P. Zeng, X. Zhang and X. Liu, *J. Phys. Chem. C*, 2011, **115**, 6149.
68. L. Hao, H. Huang, Y. Guo and Y. Zhang, *ACS Sustainable Chem. Eng.*, 2018, **6**, 1848.
69. S. Ji, T. Shi, X. Qiu, J. Zhang, G. Xu, C. Chen, Z. Jiang and C. Ye, *Sci. Rep.*, 2013, **3**, 2733.

70. Q. Li, H. Meng, P. Zhou, Y. Zheng, J. Wang, J. Yu and J. Gong, *ACS Catal.*, 2013, **3**, 882.
71. Y. Zhou, Y. Wang, T. Wen, S. Zhang, B. Chang, Y. Guo and B. Yang, *J. Colloid Interface Sci.*, 2016, **467**, 97.
72. Y. Yu, J. Zhang, X. Wu, W. Zhao and B. Zhang, *Angew. Chem. Int. Ed.*, 2012, **5**, 897.
73. H. Zhou, Q. Liu, W. Liu, J. Ge, M. Lan, C. Wang, J. Geng and P. Wang, *Chem. Asian J.*, 2014, **9**, 811.
74. S. N. Guo, Y. L. Min, J. C. Fan and Q. J. Xu, *ACS Appl. Mater. Interfaces*, 2016, **8**, 2928.
75. C. Xing, Y. Zhang, W. Yan and L. Guo, *Int. J. Hydrogen Energy*, 2006, **31**, 2018.
76. L. Wang, W. Wang, M. Shang, W. Yin, S. Sun and L. Zhang, *Int. J. Hydrogen Energy*, 2010, **35**, 19.
77. J. Zhi-fang, W. Fu-min and X. Feng, *Trans. Nonferrous Met. Soc. China*., 2011, **21**, 1767.
78. W. J. Li, D. Z. Li, W. J. Zhang, Y. Hu, Y. H. He and X. Z. Fu, *J. Phys. Chem. C*, 2010, **114**, 2154.
79. X. Cui, Y. F. Zheng, H. Y. Yin and X. C. Song, *Phys. Chem. Chem. Phys*., 2015, **17**, 29354.
80. D. Li, Z. Wu, C. Xing, D. Jiang, M. Chen, W. Shi and S. Yuan, *J. Mol. Catal. A: Chem*., 2014, **395**, 261.

Chapter 5

A Direct Z-scheme Strategy Utilizing $ZnIn_2S_4$ and Hierarchical VS_2 Microflowers for Superior Photoelectrochemical Water Oxidation

This chapter explains the design of a model system utilizing $ZnIn_2S_4$ and hierarchical VS_2 for a Z-scheme pathway, without an electron mediator, for efficient charge separation. An impressive ~ 18-fold increase in the photocurrent value has been observed in $ZnIn_2S_4$-VS_2 over its bare counterpart. A detailed investigation of the charge carrier dynamics leading to enhanced activity in the composite is carried out.

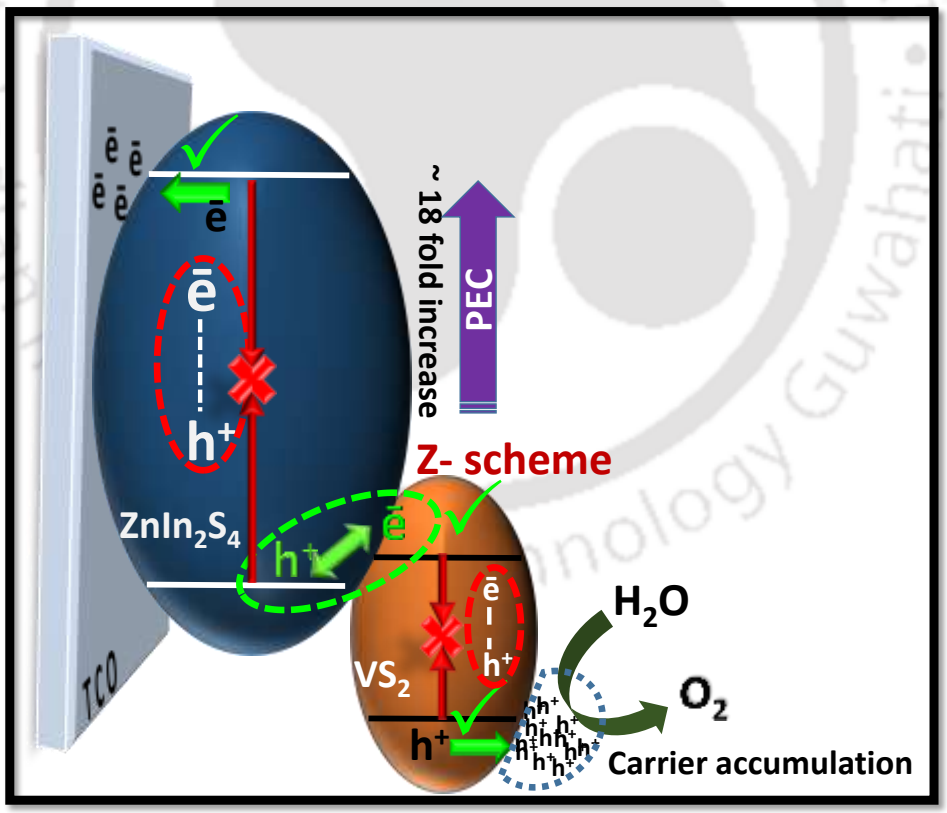

Chem. – Asian J., 2019, DOI: 10.1002/asia.201900545

5.1 INTRODUCTION

Among the various semiconductors studied as photoelectrode material, an important and promising ternary chalcogenide semiconductor belonging to the IIB–IIIA–VIA group of sulfide material is hexagonal $ZnIn_2S_4$ with 2D layered structure.[1] It has attracted attention as a photocatalyst due to its photostability, low toxicity, narrow bandgap, efficient optical absorption of solar energy in the visible light, categorising it as an exotic, eco–friendly and visible light driven photocatalyst for clean energy conversion.[2, 3] However, despite of its favourable physical properties, it exhibits poor photocatalytic performance owing to the low separation efficiency of photogenerated charge carriers.[4] Since its first report as photocatalyst by Lei et al in 2003,[1] it has been widely studied especially in heterojunction photocatalysts as synergistic components to enhance the photocatalytic efficiency for H_2 production along with various combinations.[5, 6] A heterojunction strategy that has appealed considerable attention is Z–scheme principled composite system.[7, 8] The prime advantage of Z–scheme over widely studied type II heterojunction is that apart from the improved separation of photogenerated charge carriers, electron in more negative conduction band (CB) and hole in more positive valence band (VB) potentials endow the photogenerated electrons and holes with strong reduction and oxidation ability.[9, 10] Z–scheme photocatalytic system encompasses two individual photocatalysts and a shuttle redox mediator or electron mediator, such as graphene or noble metals Au, Ag, etc. [7, 11-13] However, direct Z–scheme photocatalysts (the third generation of Z–scheme photocatalytic systems) need neither liquid electron mediators nor expensive noble metal electron mediators.[14] Thus direct Z–scheme emerges as a promising heterojunction system with components of favourable band positions forming intimate interface between them.

Vanadium disulfide (VS_2) has recently been widely studied as an emerging electrocatalyst material for hydrogen evolution reaction (HER) because of its catalytic activity on both the edge as well as basal plane.[15, 16] Because of good conductivity and abundant active sites, layered VS_2 also has a great potential in the HER.[17] Very few studies have reported VS_2 as composite (e.g. with MoS_2,[17] C_3N_4 etc[18]) for superior activity in H_2 evolution activity. Based on the calculated energy level alignment of VS_2, it serves as a favourable candidate to form Z–scheme heterostructure with $ZnIn_2S_4$. We have synthesised $ZnIn_2S_4$–VS_2 for the first time anticipating a direct Z–scheme composite without any electron

mediator. Because of the well proximity of alignment of the valence band position of $ZnIn_2S_4$ to that of the conduction band of VS_2, there is a favourable recombination of photogenerated electron–hole at the interface, leaving behind photogenerated electrons in the conduction band of $ZnIn_2S_4$ whereas holes are left behind at the valence band of VS_2 with a higher oxidation potential for efficient water oxidation reaction. The effect of lesser recombination in $ZnIn_2S_4$ in the composite owing to the favourable Z–scheme with VS_2 and higher oxidation potential at VS_2 surface is reflected in the increased photocurrent density in the composite as compared to bare $ZnIn_2S_4$.

5.2 EXPERIMENTAL SECTION

5.2.1 Preparation of $ZnIn_2S_4$

$ZnIn_2S_4$ was prepared following a previously reported method.[19] In a typical synthesis, $ZnCl_2$ (0.136 g, 1 mmol), $InCl_3$ (0.442 g, 2 mmol) and thioacetamide (C_2H_5NS) (0.300 g, 4 mmol) were dissolved in 70 mL of deionised water and transferred to a 100 mL Teflon lined autoclave and heated at 120 °C for 12 h. After cooled to room temperature, the product was washed with deionised water and ethanol several times and then dried at 60 °C for overnight.

5.2.2 Preparation of VS_2

In a typical synthesis procedure of VS_2, sodium orthovanadate ($Na_3VO_4 \cdot 2H_2O$) (1.103g, 6 mmol) and thioacetamide (C_2H_5NS) (2.404g, 32 mmol) were dissolved in 50 mL of water and kept for stirring for 1 h. The reaction mixture was then transferred to a stainless steel autoclave and hydrothermally treated at 160 °C for 24 h.[16]

5.2.3 Preparation of $ZnIn_2S_4$–VS_2

For $ZnIn_2S_4$–VS_2, calculated amount of as–synthesised $ZnIn_2S_4$ and VS_2 were measured and the components were well dispersed in 5 mL ethanol by sonication for 60 min. The well dispersed composite was then dried at 60°C overnight.

5.3 RESULTS AND DISCUSSION

5.3.1 Powder X-ray Diffraction (PXRD) Patterns

The crystal structure and phase purity of the as-synthesized compounds were determined by PXRD. **Figure 5.1** shows the powder X-ray diffraction patterns for $ZnIn_2S_4$, VS_2 and $ZnIn_2S_4$–VS_2. From **Figure 5.1**, it is observed that $ZnIn_2S_4$ shows peaks of 2θ values at 21.5°, 27.6°, 30.4°, 39.8°, 47.2°, 52.4° and 55.6°, which correspond to the (006), (102), (104), (108), (110), (116) and (022) crystallographic planes of hexagonal $ZnIn_2S_4$ (JCPDS file No. 065-2023).[20] The as–synthesized VS_2 nanosheets shows a PXRD pattern with several diffraction peaks at 2θ = 15.4°, 32.1°, 35.7°, 45.2°, 57.2°, 58.3° and 59.6° which are assigned to (001), (100), (011), (012), (110), (103) and (111) planes, respectively, consistent with the JCPDS file No. 89-1640, confirming the formation of a pure hexagonal VS_2 phase without any other impurities.[16] The PXRD pattern of the binary composite $ZnIn_2S_4$–VS_2 match well with $ZnIn_2S_4$ along with the (001) and (110) diffraction patterns of VS_2 which proves the presence of VS_2 and $ZnIn_2S_4$ in the composite. There is no distinct shift observed in the diffraction peak positions which signifies that there is no phase change of the components in the composite.

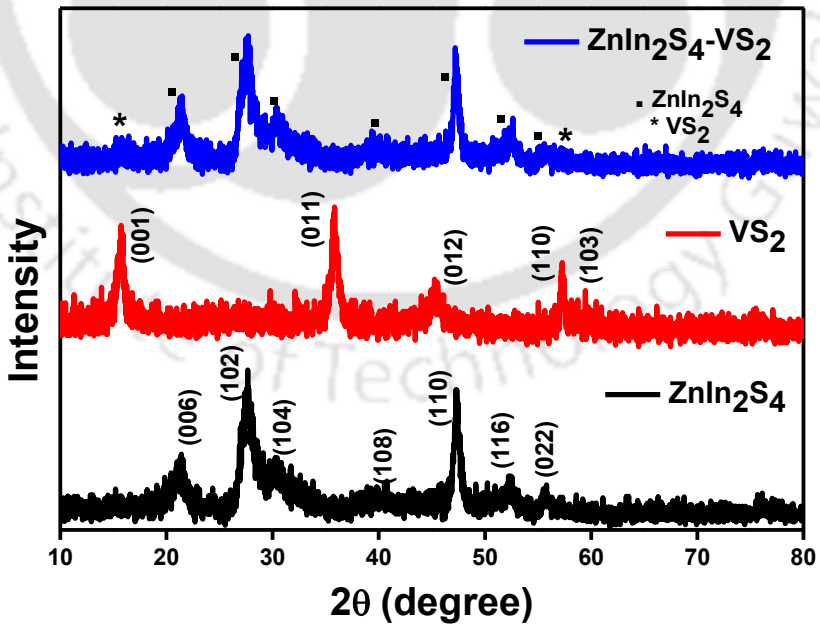

Figure 5.1: Powder X-ray diffraction pattern for as-synthesized $ZnIn_2S_4$, VS_2 and $ZnIn_2S_4$-VS_2.

5.3.2 Material Morphology and Elemental Analysis

Figure 5.2 (A, B) shows the morphological analysis of $ZnIn_2S_4$. It is seen to be constituted of flower like morphology composed of nanosheets with diameter ~ 3µm. VS_2 possesses flower like morphology with dimensions of ~ 1-3 µm with petals composed of nanosheets that are uniformly stacked in a definite pattern as shown in **Figure 5.2 (C, D)**. **Figure 5.2 (E, F)** shows the morphological features of $ZnIn_2S_4$–VS_2. Some portions in **Figure 5.2 (E, F)**, expected to be ruptured VS_2, are highlighted with dotted circles

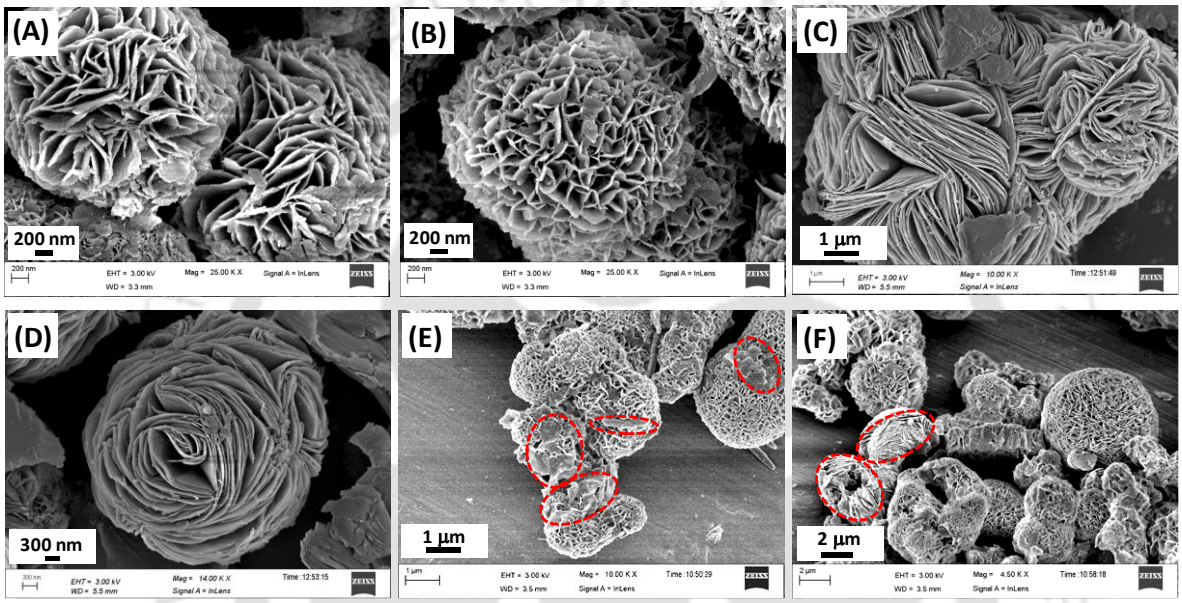

Figure 5.2: Field-emission scanning electron microscopy images of (A, B) $ZnIn_2S_4$, (C, D) VS_2 and (E, F) $ZnIn_2S_4$–VS_2. Anticipated VS_2 in $ZnIn_2S_4$–VS_2 is encircled in red dotted circles in (E, F).

FESEM images of VS_2 after sonication for 60 min are shown in **Figure 5.3 (A, B)**. It proves that the structure of VS_2 is dissociated during the sonication process which leads to uneven structures, thus leading to more surface area for interaction between the components. To further affirm the claim, FESEM of bare $ZnIn_2S_4$ sonicated for 60 min are shown in **Figure 5.3 (C, D)** which clarifies that the clear flower like morphology of $ZnIn_2S_4$ remains intact even after sonication. Thus from **Figure 5.2 (E, F)** we can envisage the irregular morphology in the composite to be VS_2 (encircled in red dots) which helps in better physical interaction among the components in the composite.

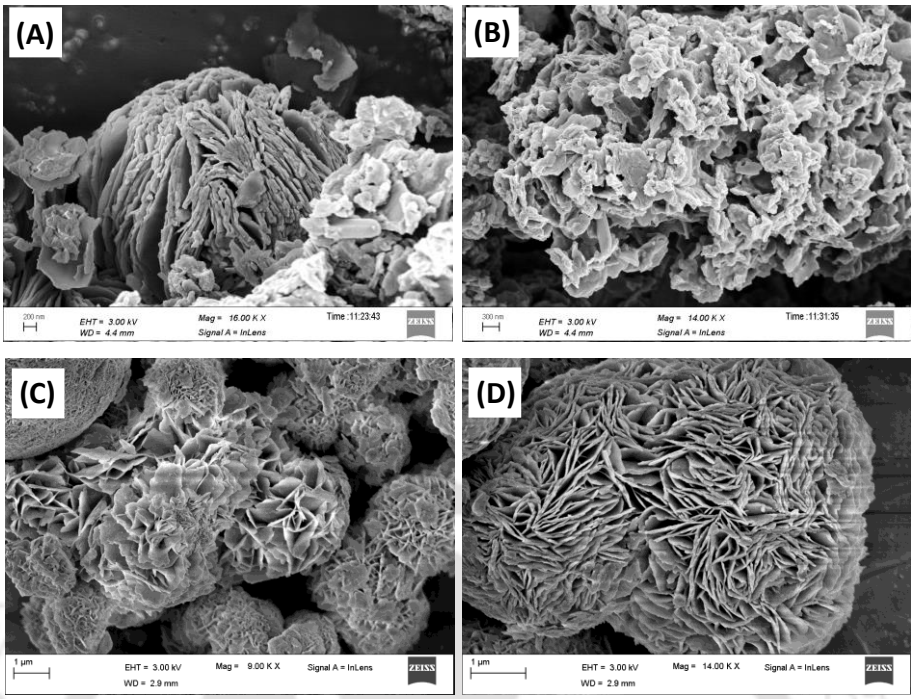

Figure 5.3: Field-emission scanning electron microscopy (FESEM) images of (A, B) VS_2 and (C, D) $ZnIn_2S_4$ after sonication for 60 min.

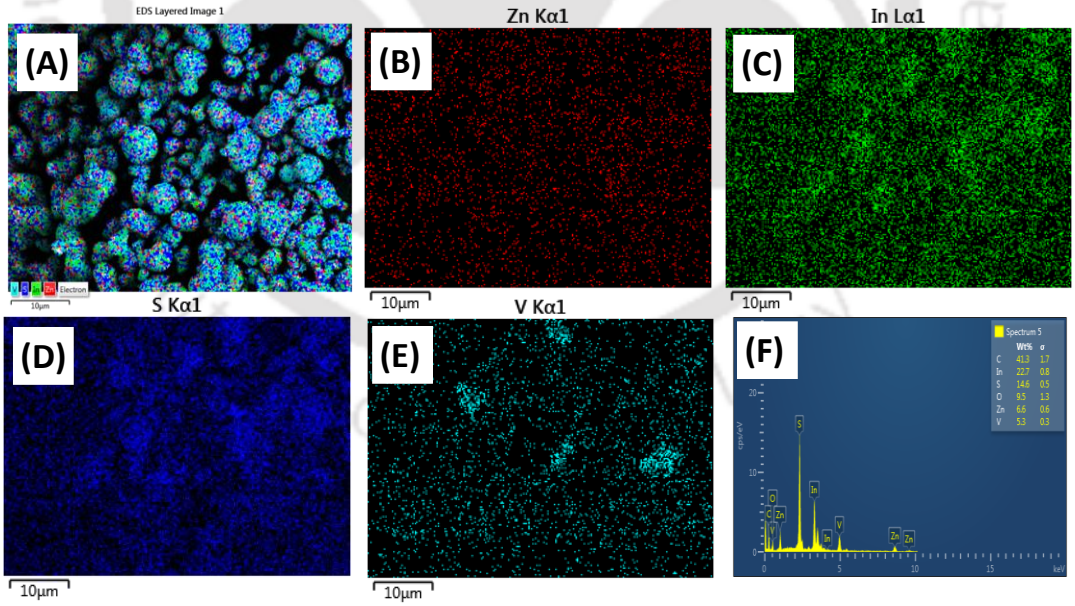

Figure 5.4: (A) Energy-dispersive X-ray (EDX) mapping of $ZnIn_2S_4$–VS_2. Homogeneous elemental distribution of (B) Zn, (C) In, (D) S and (E) V respectively in the area in (A) and (F) Energy-dispersive X–ray spectrum of $ZnIn_2S_4$–VS_2

5.3.3 Ultraviolet-Visible Diffuse Reflectance Spectra and Band Gap Calculation

In order to understand the absorbance profile of the synthesised compounds, the UV-visible diffuse reflectance spectra of $ZnIn_2S_4$, VS_2 and the binary composite $ZnIn_2S_4$–VS_2 are taken and represented in **Figure 5.5 (A)**. It is seen that VS_2 absorbs well in the whole visible region. Both the compounds $ZnIn_2S_4$ and $ZnIn_2S_4$–VS_2 absorb in the visible region with a slight red shift of the absorbance wavelength in $ZnIn_2S_4$ –VS_2. However, upon combination with VS_2, the composite $ZnIn_2S_4$–VS_2, displays an effect of enhanced optical absorption in the higher wavelength region ($\lambda > \sim 500$ nm). The steep absorption around 400–500 nm in $ZnIn_2S_4$ and $ZnIn_2S_4$–VS_2 can be attributed to a band transition.[21] Band gaps are determined by Tauc plot from the intersection of the extrapolated linear portion with the X–axis as shown in **Figure 5.5 (B)**.

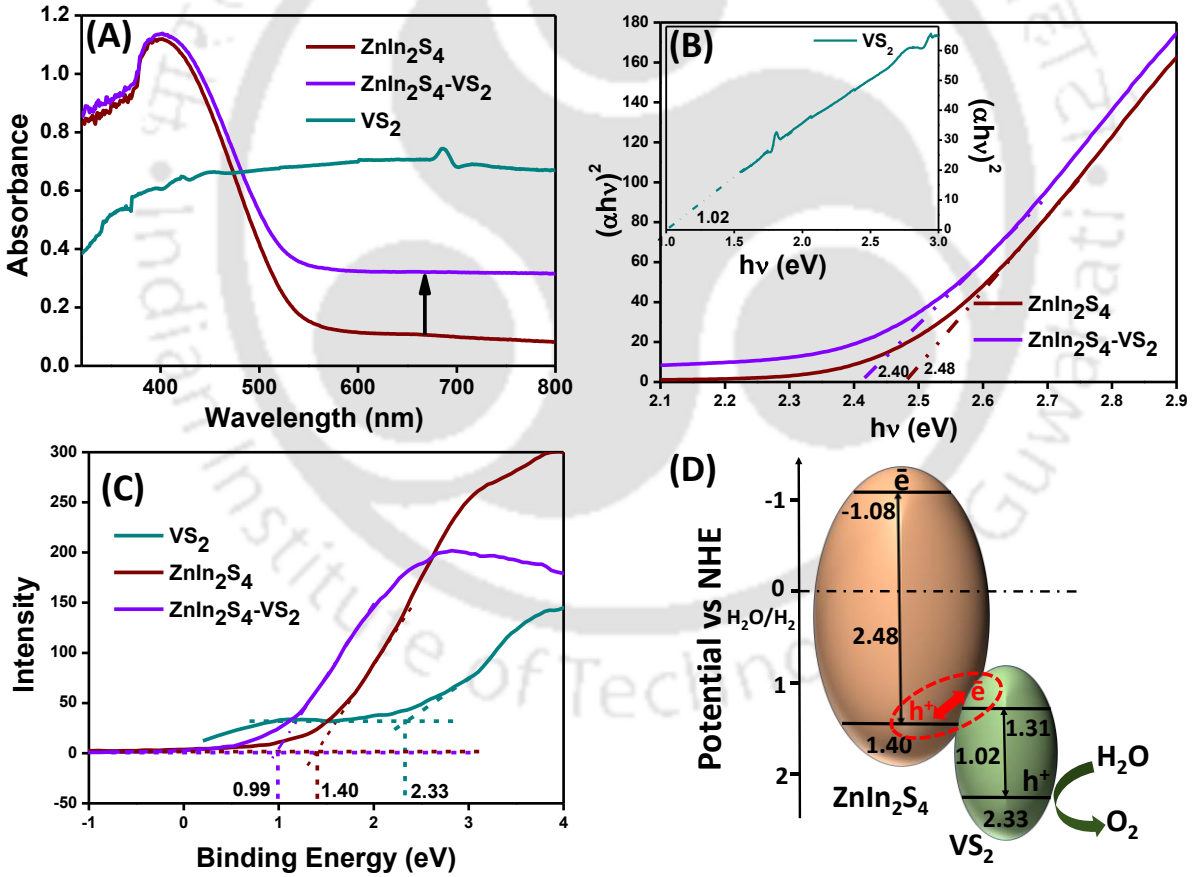

Figure 5.5: (A) Ultraviolet–visible diffuse reflectance spectra of $ZnIn_2S_4$, VS_2 and $ZnIn_2S_4$–VS_2, (B) Tauc plot of $ZnIn_2S_4$ and $ZnIn_2S_4$ –VS_2. Inset is the Tauc plot of VS_2, (C) XPS valence band spectra of $ZnIn_2S_4$, VS_2 and $ZnIn_2S_4$–VS_2 (D) band structure of proposed Z–scheme of $ZnIn_2S_4$–VS_2.

The band gap of $ZnIn_2S_4$, VS_2 and $ZnIn_2S_4$–VS_2 are calculated to be 2.48, 1.02, and 2.40 eV, respectively. In addition, the valence band position of $ZnIn_2S_4$, $ZnIn_2S_4$–VS_2 and VS_2 are determined from the XPS valence band spectra as shown in **Figure 5.5 (C)**. The valence band position of $ZnIn_2S_4$, $ZnIn_2S_4$–VS_2 and VS_2 are determined to be 1.40, 0.99, and 2.33 eV, respectively. Based on the above calculations, the band energy diagram of $ZnIn_2S_4$–VS_2 is schematically shown in **Figure 5.5 (D)**. From the energy band diagram, it is seen that the conduction band of VS_2 and valence band of $ZnIn_2S_4$ are favourably aligned for electron hole recombination at the heterojunction leaving behind electrons in the conduction band of $ZnIn_2S_4$ and holes in the valence band of VS_2 favouring a Z–scheme of electron transfer pathway.

5.3.4 Fourier Transformed Infra-Red (FT-IR) and Raman Spectra Analysis

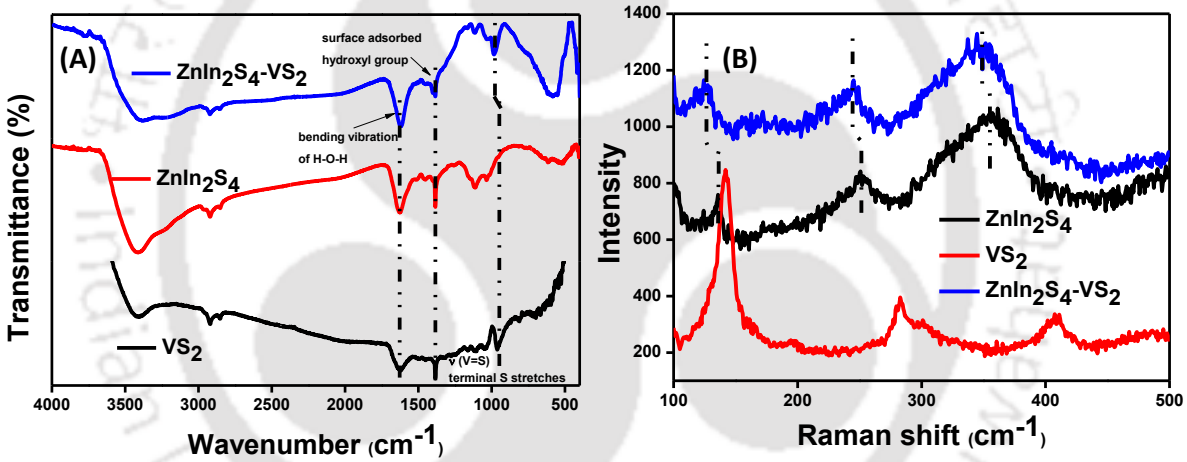

Figure 5.6: (A) Fourier transformed infra-red spectra and (B) Raman spectra of $ZnIn_2S_4$, VS_2 and $ZnIn_2S_4$–VS_2

FT-IR spectra of $ZnIn_2S_4$, VS_2 and $ZnIn_2S_4$–VS_2 are shown in **Figure 5.6 (A)**. The broad band centred at ~ 3420 cm^{-1} can be attributed to the O–H stretching vibration of the adsorbed H_2O from the atmosphere.[22] The band at ~ 1620 cm^{-1} in all the samples corresponds to O–H bending vibrations of adsorbed water molecules while the one at ~ 1390 cm^{-1} is due to hydroxyl groups.[23] Peaks observed between 400 and 700 cm^{-1} are assigned to metal–sulfur bond.[24] The peaks at ~ 2921 and ~ 2852 cm^{-1} in all the samples occur from the C–H stretching modes.[25, 26] In the FT-IR spectrum of VS_2, apart from the peaks mentioned above corresponding to adsorbed moisture and metal–sulfur bonds, a peak featured at ~ 984 cm^{-1} is observed assigned to the υ(V=S) terminal S stretches which confirms the presence of V^{4+}

oxidation state in VS_2 further confirmed by XPS.[27] The V=S peak is also observed in $ZnIn_2S_4$ –VS_2 which is shifted towards higher energy compared to VS_2, which could be indicative of the interaction of $ZnIn_2S_4$ and VS_2 via the terminal S of VS_2. This observation is further observed in XPS analysis as discussed later.

Raman spectroscopy is a widely used useful tool to characterise the structural bonding nature in compounds. Raman spectral studies were carried out for $ZnIn_2S_4$, VS_2 and $ZnIn_2S_4$–VS_2 as shown in **Figure 5.6 (B)**. In $ZnIn_2S_4$, characteristic Raman peaks observed at around 244 and 343 cm^{-1} are typical molecular vibration of $ZnIn_2S_4$ assigned to the longitudinal optical mode, LO_1 and LO_2 respectively.[28] The band featured at ~ 123 cm^{-1} proves the layered structure of hexagonal $ZnIn_2S_4$.[29] In the Raman spectra of VS_2, characteristic peaks at ~ 278 and 404 cm^{-1} are due to the in-plane and out-of-plane A_{1g} vibration modes. In the Raman spectra of VS_2, the observed peaks at ~ 140, ~ 192, ~ 278, ~ 404 cm^{-1} correspond to the rocking and stretching vibrations of V–S bonds or their combination.[30] The characteristic peaks at ~ 278 and ~ 404 cm^{-1} are due to the in-plane E_{2g}^1 and out-of-plane A_{1g} vibration modes. The A_{1g} mode is due to the out-of-plane vibration of only the S atoms in opposite directions while the in-plane mode formed from opposite vibration of the two S atoms with respect to the V atom.[31] In the composite $ZnIn_2S_4$–VS_2, a clear red shift of the Raman peaks of $ZnIn_2S_4$ is observed which implies interaction among the components in the composite, $ZnIn_2S_4$–VS_2.[32]

5.3.5 X-ray Photoelectron Spectroscopy (XPS) Spectra

In order to understand the composition of $ZnIn_2S_4$, VS_2, and $ZnIn_2S_4$–VS_2 and comprehend the bonding state of each element in composite as well as the bare counterparts, XPS analysis is carried out. Peaks are calibrated with respect to C 1s at 284.7 eV. The high-resolution XPS spectra of Zn 2p and In 3d are shown in **Figure 5.7 (A)** and **Figure 5.7 (B)**, respectively. The XPS signals of Zn 2p of $ZnIn_2S_4$ are observed at binding energies (B. E.) 1022.18 eV (Zn $2p_{3/2}$) and 1045.24 eV (Zn $2p_{1/2}$), which are in good agreement with literature.[33] The Zn 2p core level spectra of $ZnIn_2S_4$–VS_2 also shows the presence of signals at B. E. of 1021.54 and 1044.54 eV corresponding to Zn $2p_{3/2}$ and Zn $2p_{1/2}$ respectively. Two shake-up satellite features for Zn 2p of $ZnIn_2S_4$ (1025.27 and 1048.38 eV) and $ZnIn_2S_4$–VS_2 (1023.66 and 1046.51 eV) are observed in the spectrum (**Figure 5.7 (A)**). The B. E. of In 3d of $ZnIn_2S_4$ appear at 445.34 eV (In $3d_{5/2}$) and 452.5 eV (In $3d_{3/2}$), while that for $ZnIn_2S_4$–VS_2 is observed at B. E. values 444.78 and 452.29 eV corresponding to In $3d_{5/2}$ and In $3d_{3/2}$,

respectively.[34] In $3d_{5/2}$ core level spectra is further deconvoluted to two components at B. E. 447.68 and 454.86 eV (for $ZnIn_2S_4$) and 446.54 and 453.6 eV (for $ZnIn_2S_4$–VS_2) (**Figure 5.7 (B)**).

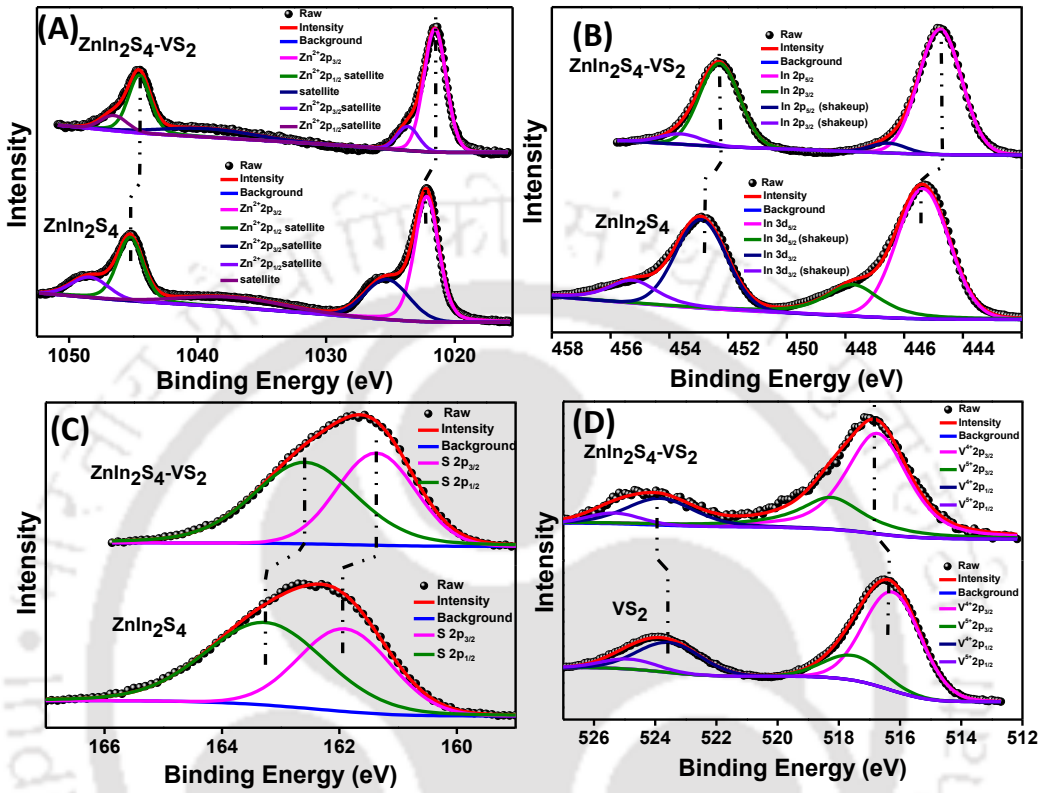

Figure 5.7: X-ray photoelectron spectroscopy (XPS) spectra of (A) Zn 2p, (B) In 3d, (C) S 2p and (D) V 2p.

The peak fitting analysis of S 2p of $ZnIn_2S_4$ and $ZnIn_2S_4$–VS_2 confirms the presence of S^{2-} with two peaks located at binding energy (B. E.) 162.17 and 163.7 eV for $ZnIn_2S_4$ and at 161.53 and 162.9 eV eV for $ZnIn_2S_4$–VS_2 which can be assigned to S $2p_{3/2}$ and S $2p_{1/2}$, respectively (**Figure 5.7 (C)**). The peak at B. E. ~ 163 eV can be attributed to metal–sulfur bond.[35, 36] Apart from the S $2p_{3/2}$ and S $2p_{1/2}$ peaks observed at 162.7 and 164.1 eV, respectively for VS_2, a distinct peak at 168.19 eV is observed in S 2p spectra of VS_2 that can be assigned to sulfate (S(VI)) which indicates that the surface of the VS_2 is oxidised when exposed to air (**Figure 5.8 (A)**).[37] However, on forming composite $ZnIn_2S_4$–VS_2, the surface oxidised sulfur is not observed and the fraction of metal–sulfur bond increases from 0.23 in VS_2 to 0.4 in the composite due to the interaction of Zn and In with VS_2 through the exposed S edges thus increasing the number of metal-S bonds in the composite. V 2p peaks appear

asymmetrically in VS_2 as well as $ZnIn_2S_4$–VS_2 indicating more than one oxidation state of vanadium ions. Deconvolution of the V 2p core level spectra revealed the presence of mixed valent V species at the surface of the prepared materials. The V 2p signals of VS_2 at 516.24 and 523.54 eV (**Figure 5.7 (D)**) are attributed to V $2p_{3/2}$ and V $2p_{1/2}$, implying the existence of V^{4+}. Owing to a strong affinity of vanadium towards oxygen, it undergoes fast oxidation under atmospheric condition which is confirmed by the observance of the other V 2p peaks at 517.54 eV ($2p_{3/2}$) and 524.84 eV ($2p_{1/2}$) which belong to V^{5+} (V_2O_5).[36] Similarly V 2p signals of $ZnIn_2S_4$–VS_2 shows two peaks at 516.57 and 523.66 eV which are associated with V^{4+} $2p_{3/2}$ and V^{4+} $2p_{1/2}$ while the two weak peaks at 518.06 and 525.14 eV are ascribed to V^{5+} $2p_{3/2}$ and V^{5+} $2p_{1/2}$ respectively.[36, 38]As observed from **Figure 5.7 (A)**, **Figure 5.7 (B)** and **Figure 5.7 (C)**, respectively, the B. E. of Zn 2p, In 3d and S 2p for $ZnIn_2S_4$–VS_2 are slightly shifted to lower energy as compared to bare $ZnIn_2S_4$. Such energy shift towards lower energy in the composite could be explained by the presence of higher electron density on $ZnIn_2S_4$ in the composite due to lesser electron hole recombination by virtue of the proposed Z–scheme of electron transfer in $ZnIn_2S_4$ –VS_2. The electron transfer mechanism is further supported by the shift in B. E. of V 2p towards higher energy in $ZnIn_2S_4$–VS_2 as compared to VS_2 (**Figure 5.7 (D)**). The lesser electron density at the conduction band of VS_2 because of the favourable electron–hole recombination at the conduction band of VS_2 and valence band of $ZnIn_2S_4$, results in a decrease in the electron density available at VS_2 in $ZnIn_2S_4$–VS_2 compared to bare VS_2. This results in a higher B. E. of the XPS peak of V 2p in $ZnIn_2S_4$–VS_2 compared to VS_2.

As the presence of oxidised V (V_2O_5) is confirmed from the V 2p core level XPS spectra, O 1s XPS analysis for VS_2 and the composite $ZnIn_2S_4$–VS_2 are carried out (**Figure 5.8 (B)**). The fitting analysis of O 1s peak confirms the presence of O^{2-} with three peaks originating from distinct oxygen environments. The peak located at ~ 529 eV corresponds to O^{2-} in metal oxide indicating the presence of V–O, suggesting that V is inevitably partially oxidised to V_2O_5 in the hydrothermal process,[18] whereas the peaks positioned at ~ 531, and ~ 532 eV corresponds to other forms of oxygen such as O–H, and surface adsorbed moisture respectively indicating the presence of vanadium oxide (**Figure 5.8 (B)**) .[36, 39]

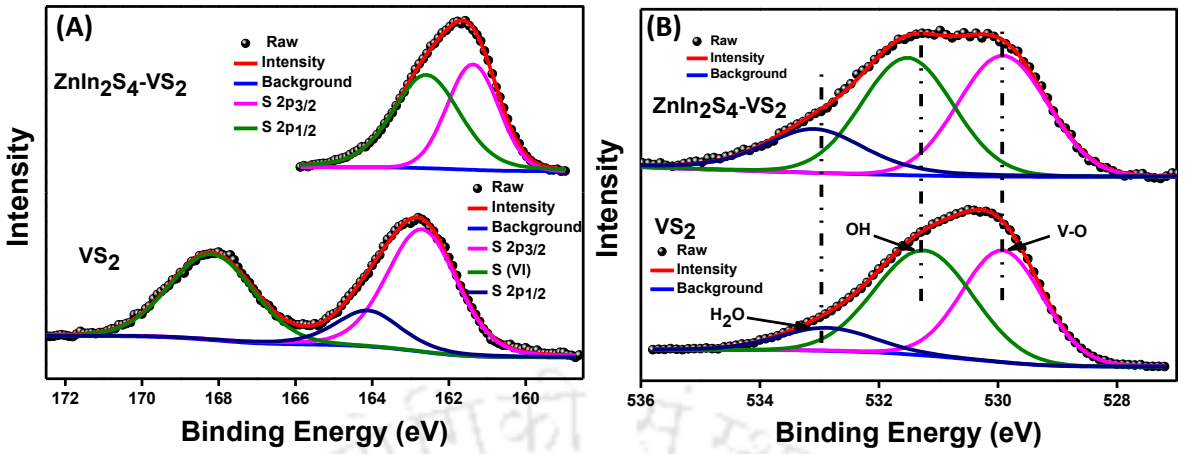

Figure 5.8: X-ray photoelectron spectroscopy (XPS) spectra of (A) S 2p and (B) O 1s of $ZnIn_2S_4$–VS_2 and VS_2.

5.3.6 Determination of Charge Transfer Mechanism

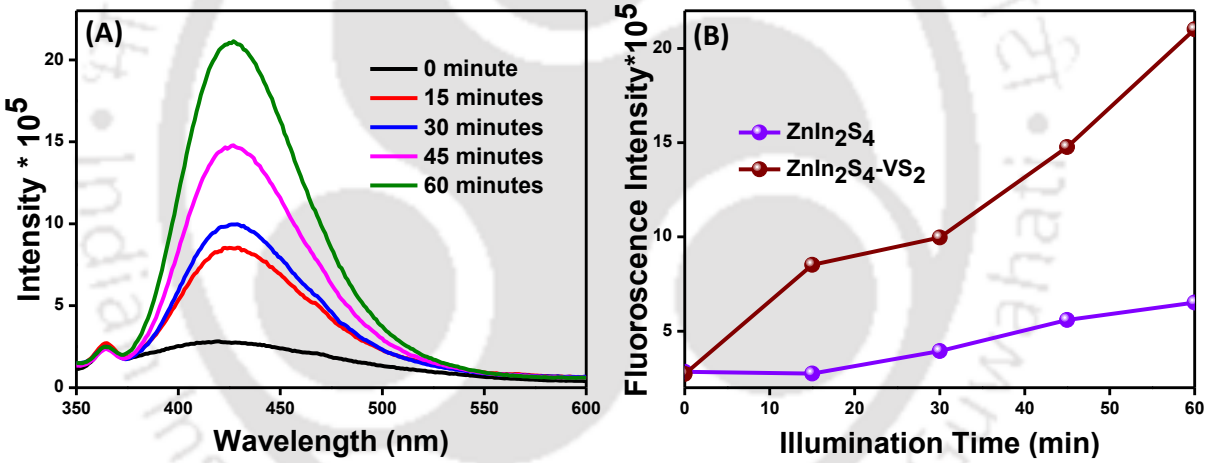

Figure 5.9: (A) Change in photoluminescence with irradiation time for $ZnIn_2S_4$–VS_2 dispersed in terephthalic acid and (B) fluorescence intensity at 426 nm versus irradiation time for $ZnIn_2S_4$ and $ZnIn_2S_4$–VS_2.

For better understanding the charge transfer mechanism, the rate of formation of ·OH in bare $ZnIn_2S_4$ as well as $ZnIn_2S_4$–VS_2 under light illumination is measured by using terephthalic acid as a probe molecule in a photoluminescence technique. Terephthalic acid, which is otherwise a very poor fluorescent molecule could react with ·OH to form 2-hydroxyterephthalic acid, a highly fluorescent molecule. The potential of $OH^-/OH^\bullet$ is reported to be about 2.3 V (vs NHE).[40] As the valence band potential of VS_2 is more positive (~ 2.4 V vs NHE) than the $OH^-/OH^\bullet$ potential (2.3 V vs NHE), the holes in the valence band

of VS_2 can react with OH^- to generate $OH^\bullet$. The holes on the valence band of $ZnIn_2S_4$ however are not capable of the oxidation due to its more negative reduction potential (~ 1.40 V vs NHE) than OH^-/ $OH^\bullet$. The formation of hydroxyl radicals ($OH^\bullet$) on the surface of $ZnIn_2S_4$ and $ZnIn_2S_4$–VS_2 were detected using photoluminescence method using terephthalic acid as a probe molecule. In a typical experiment, 10 mg photocatalyst is added into 20 mL mixed solution consisting of $5x10^{-4}$ M terephthalic acid and $2x10^{-3}$ M NaOH. Under UV–visible light irradiation, the PL emission spectra of 2–hydroxyterephthalic acid generated are measured every 15 min using the excited wavelength of 325 nm. The change in PL spectra observed with irradiation time for $ZnIn_2S_4$–VS_2 dispersed in terephthalic acid are shown in **Figure 5.9 (A)** while the fluorescence intensity at 426 nm versus irradiation time of $ZnIn_2S_4$ and $ZnIn_2S_4$–VS_2 is shown in **Figure 5.9 (B)**. It is seen that the fluorescent intensity of $ZnIn_2S_4$–VS_2 dispersed in terephthalic acid is drastically increased compared to that of $ZnIn_2S_4$. This provides a clear evidence that sufficient number of holes are available in valence band of VS_2 in $ZnIn_2S_4$–VS_2 for oxidation of OH^- to $OH^\bullet$. This experiment further rules out the formation of a type–II heterostructure where holes accumulate at the valence band of $ZnIn_2S_4$ which is thermodynamically unfavourable to generate $OH^\bullet$which is contrary to the experimental findings from the PL experiment using terephthalic acid probe.

5.3.7 Steady State and Time Resolved Photoluminescence

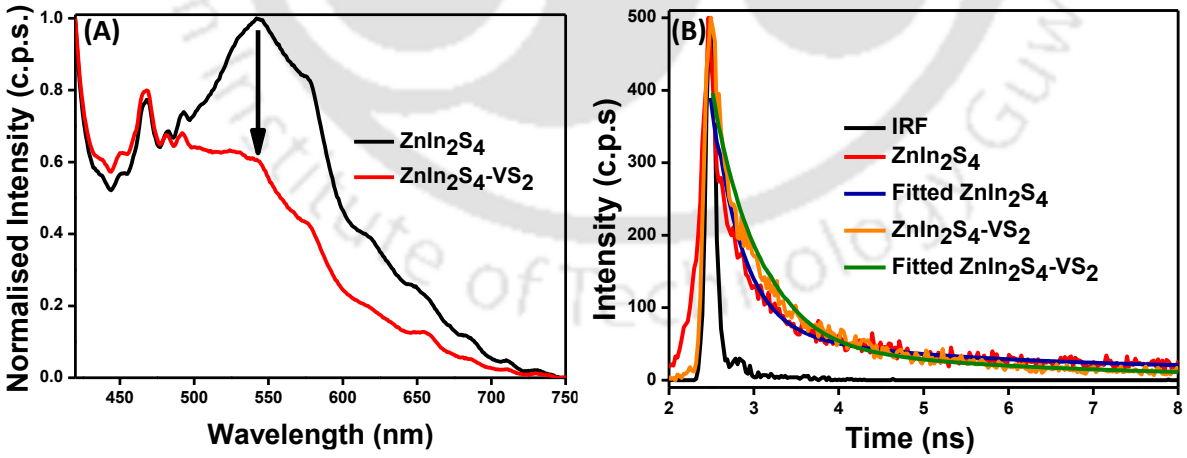

Figure 5.10: (A) Steady-state photoluminescence spectra of $ZnIn_2S_4$ and $ZnIn_2S_4$-VS_2 (excitation at 420 nm) and (B) Time-resolved photoluminescence spectra of $ZnIn_2S_4$ and $ZnIn_2S_4$–VS_2 (Excitation at 405 nm, Emission at 550 nm)

In order to access the charge transfer and separation behavior steady–state photoluminescence (PL) (**Figure 5.10 (A)**) and time-resolved photoluminescence experiments (TRPL) (**Figure 5.10 (B)**) were carried out. Room temperature steady-state PL analyses were carried out to investigate the excited state charge transfer processes in $ZnIn_2S_4$-VS_2. The PL spectra of $ZnIn_2S_4$ shows a strong emission at ~ 545 nm upon excitation at 420 nm (**Figure 5.10 (A)**) indicating an intense charge recombination occurring in the photocatalyst. On introduction of VS_2, the PL intensity quenches drastically in $ZnIn_2S_4$–VS_2 implying a reduced possibility of photogenerated electron hole pair recombination in the composite $ZnIn_2S_4$–VS_2 compared to $ZnIn_2S_4$. Lesser electron hole recombination in $ZnIn_2S_4$–VS_2 is due to the availability of more number of photogenerated electrons in the conduction band of $ZnIn_2S_4$ as the photogenerated holes in the valence band of $ZnIn_2S_4$ undergo efficient recombination with the electrons in the conduction band of VS_2 as proposed in the Z–scheme electron transfer pathway.

Charge carrier dynamics of $ZnIn_2S_4$ and $ZnIn_2S_4$–VS_2 were probed by time-resolved photoluminescence (TRPL) spectroscopy. The synergistic effects of energy transfer between the components is determined by TRPL spectroscopy at an excitation wavelength of 405 nm and emission monitored at 550 nm are shown in **Figure 5.10 (B)**. The average lifetime, $\langle\tau\rangle$, was calculated using the following equation:

$$< \tau >= \frac{\alpha_1 \tau_1^2 + \alpha_2 \tau_2^2}{\alpha_1 \tau_1 + \alpha_2 \tau_2}$$

Various parameters like fitting parameter (χ^2), intensity (α_1, α_2), excited-state lifetime (τ_1, τ_2), and average exciton lifetime ($\langle\tau\rangle_{ns}$) of $ZnIn_2S_4$ and $ZnIn_2S_4$–VS_2 are tabulated in **Table 5.1**. The average emission lifetime of $ZnIn_2S_4$–VS_2 (~ 1.31 ns) is much shorter than that of $ZnIn_2S_4$ (~ 2.45 ns). Due to the favourable electron hole recombination at $ZnIn_2S_4$ and VS_2 junction, photogenerated electrons are available at the conduction band of $ZnIn_2S_4$ for a longer time thus leading to an enhanced electron lifetime in the composite compared to $ZnIn_2S_4$.[41]

Table 5.1: Tabulation of Fitting Parameter (χ^2), Intensity (α_1, α_2) (%), Excited-State Lifetime (τ_1, τ_2), and Average Exciton Lifetime ($\langle\tau\rangle$ (ns)) of $ZnIn_2S_4$ and $ZnIn_2S_4$–VS_2

	χ^2	α_1 (%)	α_2 (%)	τ_1 (ns)	τ_2 (ns)	$<\tau>$ (ns)
$ZnIn_2S_4$	1.105	91.246	8.754	0.348	2.640	1.31
$ZnIn_2S_4$-VS_2	1.156	69.304	30.696	0.470	3.125	2.45

5.3.8 Electrochemical Characterisations for Water Oxidation

The water oxidation ability of the photoanodes were determined by photoelectrochemical characterisations. **Figure 5.11 (A)** shows the photocurrent density of $ZnIn_2S_4$ and $ZnIn_2S_4$–VS_2 with applied potential ranging from 0 to 1.5 V (vs Ag/AgCl) under dark and light conditions (J–V curve). It is observed that $ZnIn_2S_4$–VS_2 (~ 56 μA cm^{-2}) shows a dramatic improvement of ~ 18 fold in photocurrent value compared to $ZnIn_2S_4$ (~ 3 μA cm^{-2}) measured at 1.23 V vs RHE under 1 Sun illumination. This significant upsurge of photocurrent in $ZnIn_2S_4$–VS_2 implies an increased charge carrier availability in the composite which is an evidence of reduced recombination of electron hole pair at $ZnIn_2S_4$ in the composite by virtue of the proposed Z–scheme electron transfer pathway. Chronoamperometric current vs time (I–t) curve with chopped illumination at an interval of 10 seconds is shown in **Figure 5.11 (B)**. An increased photocurrent density of $ZnIn_2S_4$–VS_2 as compared to $ZnIn_2S_4$ in consistency with the I–V measurements is observed. The photo response of $ZnIn_2S_4$–VS_2 is considerably increased as compared to $ZnIn_2S_4$. However, from the chopped photocurrent measurements (**Figure 5.11 (B)**, **Figure 5.12 (A)**), although a considerably high increment in photocurrent is observed for $ZnIn_2S_4$–VS_2, it is noteworthy to observe a relatively slower photo current response in $ZnIn_2S_4$–VS_2 composite than $ZnIn_2S_4$. This can be explained by the fact that the additional charge on the surface states accumulates the minority carriers due to reduced recombination by virtue of the effective Z–scheme proposed.[42] Such an additional charging requires slow kinetics of charge transfer through the surface states.[43] It can further be supported by the increased charge storage resulted in increased capacitance by the surface states in the composite as explained from the fitted parameters of Nyquist plot (**Table 5.2**). The stored charge leads to a slow and continuous release of electrons from the composite resulting in a relatively slower response. The slow

kinetics of charge transfer from the semiconductor interface implies that the photogenerated current is added to the dark current which explains the dark current observed in $ZnIn_2S_4$–VS_2 in **Figure 5.11 (A)** and **Figure 5.11 (B)**, thus resulting in effective utilisation and storage of solar energy.[43]

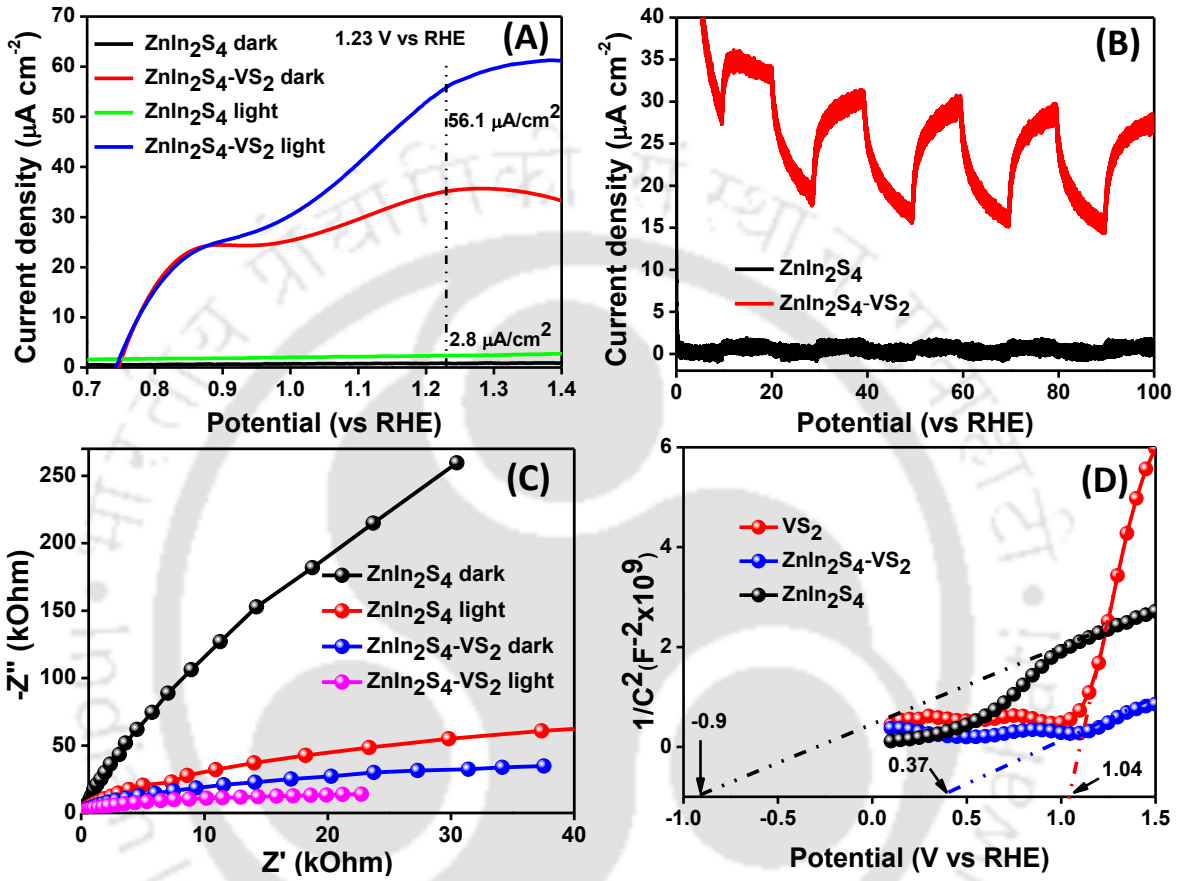

Figure 5.11: (A) J–V curves of $ZnIn_2S_4$ and $ZnIn_2S_4$–VS_2 under dark and illumination, (B) Current density vs time plots of $ZnIn_2S_4$ and $ZnIn_2S_4$–VS_2. Light turned on and off at an interval of 10 seconds, (C) Nyquist plots of $ZnIn_2S_4$ and $ZnIn_2S_4$–VS_2 under dark and light conditions and (D) Mott–Schottky plots of $ZnIn_2S_4$, VS_2 and $ZnIn_2S_4$–VS_2 measured at a frequency of 1 KHz under dark condition. The electrolyte used is 0.5 M Na_2SO_4.

The intrinsic electronic charge transport properties in the bulk and interface of the photoelectrodes under dark and light illumination were studied by electrochemical impedance spectroscopy (EIS). Nyquists plots of $ZnIn_2S_4$ and $ZnIn_2S_4$–VS_2 under dark and illumination are shown in **Figure 5.11 (C)**. The arc observed is smaller under light illumination than under dark for both $ZnIn_2S_4$ and $ZnIn_2S_4$–VS_2. It is due to the better charge transfer efficiency under light illumination as there is increased number of photogenerated charge carriers available

under light illumination. Further, the smaller arc radius of $ZnIn_2S_4$–VS_2 compared to $ZnIn_2S_4$ under both dark and 1 Sun illumination conditions indicates a better charge transfer efficiency in the composite. In order to correlate changes in the Nyquist plots with the dynamics of charge transport through the bulk of the photoanode and the surface interface with the aqueous electroyte, the EIS data is fitted in an equivalent model as shown in **Figure 5.12 (B)**. The parameters obtained from the fitted plots for $ZnIn_2S_4$ and $ZnIn_2S_4$–VS_2 under dark and under illumination at 0.7 V vs Ag/AgCl are tabulated in **Table 5.2**. Detailed insight into the fitted parameters provide with a comprehension of the charge transfer processes at the photoanodes and the reason of increased photocurrent density of the composite $ZnIn_2S_4$–VS_2. The general equivalent circuit (EC) used to interpret the impedance spectroscopic data is shown in **Figure 5.12 (B)**. Various components in the EC consists of the series resistance (R_s), capacitance of the bulk (C_{bulk}), charge transfer resistance of the bulk ($R_{ct,bulk}$), charge transfer resistance of the surface states ($R_{ct,trap}$) and capacitance of the surface states (C_{trap}). The parameters obtained from fitted Nyquist plots for $ZnIn_2S_4$ and $ZnIn_2S_4$–VS_2 under dark and under illumination at 0.7V vs Ag/AgCl are tabulated in **Table 5.2**.

Table 5.2: Tabulation of fitted parameters of Nyquist plot at 0.7 V vs Ag/AgCl under dark and 1 sun illumination condition

	R_s (Ω)	**C_{bulk} (F)**	**$R_{ct,\ bulk}$ (Ω)**	**$R_{ct\ trap}$ (Ω)**	**C_{trap}(F)**
$ZnIn_2S_4$ dark	32.65	3.77×10^{-6}	3615	1.67×10^{6}	1.54×10^{-6}
$ZnIn_2S_4$ light	31.36	4.21×10^{-6}	6124	1.32×10^{5}	2.37×10^{-6}
$ZnIn_2S_4$–VS_2 dark	30.46	2.67×10^{-6}	381.1	2.52×10^{4}	3.69×10^{-6}
$ZnIn_2S_4$–VS_2 light	30.59	2.72×10^{-6}	402.7	1.86×10^{4}	3.66×10^{-6}

It is observed from **Table 5.2** that charge transfer resistance at the bulk ($R_{ct,\ bulk}$) in the composite $ZnIn_2S_4$–VS_2 (381.1 Ω and 402.7 Ω for dark and light respectively) is much lesser than $ZnIn_2S_4$ (3615 and 6124 Ω for dark and light, respectively). A similar trend is also observed in the charge transfer resistance of the surface states ($R_{ct,trap}$) which is much lesser in the composite $ZnIn_2S_4$–VS_2 (2.52×10^4 and 1.86×10^4 Ω for dark and light, respectively)

than in bare $ZnIn_2S_4$ (1.67 x10^6 and 1.32 x10^5 Ω for dark and light, respectively). The decrease in charge transfer resistance in the composite implies a favourable movement of charge carriers both in bulk and at the surface states. Moreover, the capacitance of the surface states is increased in $ZnIn_2S_4$–VS_2 (3.69 and 3.66 µF for dark and light, respectively) compared to $ZnIn_2S_4$ (1.54 and 2.37 µF for dark and light, respectively). Thus the increased activity of the composite $ZnIn_2S_4$–VS_2 could be attributed to the increase in capacitance of the surface state in the composite and a reduced charge transfer resistance favouring increased collection of hole at the electrode surface favouring an enhanced water oxidation.

Mott–Schottky curves to determine the flat band potential and donor density is shown in **Figure 5.11 (D)**. A positive slope of Mott Schottky curves implies n type conductivity of the materials. The donor density is calculated to be 2.01x10^{22}, 2.1x10^{21} and 1.87x10^{22} cm^{-3} for $ZnIn_2S_4$, VS_2 and $ZnIn_2S_4$–VS_2, respectively. The increase in donor density of $ZnIn_2S_4$–VS_2 compared to VS_2 proves that there is increased number of holes on the surface in $ZnIn_2S_4$–VS_2 than in bare VS_2 owing to the Z–scheme charge transfers favoring water oxidation. However, the minimal increase in charge carrier density in $ZnIn_2S_4$ compared to $ZnIn_2S_4$–VS_2 could be corroborated to the increase in bulk capacitance (C_{bulk}) in $ZnIn_2S_4$ (3.77 µF) compared to $ZnIn_2S_4$–VS_2 (2.67 µF). The much higher charge transfer resistance ($R_{ct,\ bulk}$) prevents in favourable collection of the photogenerated charge carriers resulting in increased recombination which ultimately leads to an observation of decreased photocurrent density in $ZnIn_2S_4$. There is an accumulation of minority carriers in the surface state owing to the proposed Z–scheme which is also proved by the increased capacitance of surface states in $ZnIn_2S_4$–VS_2 compared to $ZnIn_2S_4$. The flat band potential (E_{fb}) is approximately determined by extrapolation of the linear Mott-Schottky plot (**Figure 5.11 (D)**). The additional charge at the surface state produces an increase of the voltage in the dipole layer, which results in an apparent anodic displacement of flat band potential of $ZnIn_2S_4$–VS_2 (0.37 V) compared to $ZnIn_2S_4$ (-0.9 V) as observed from **Figure 5.11 (D)**. [43]

The J–V curve under continuous chopping of light at an interval of 2 sec is shown in **Figure 5.12 (A)**. The light response is considerably increased in $ZnIn_2S_4$–VS_2 compared to $ZnIn_2S_4$ which is attributed to the photo responsive behavior of $ZnIn_2S_4$ which is considerably increased in the composite owing to the reduced recombination and increased flux of electron transfer in the composite.

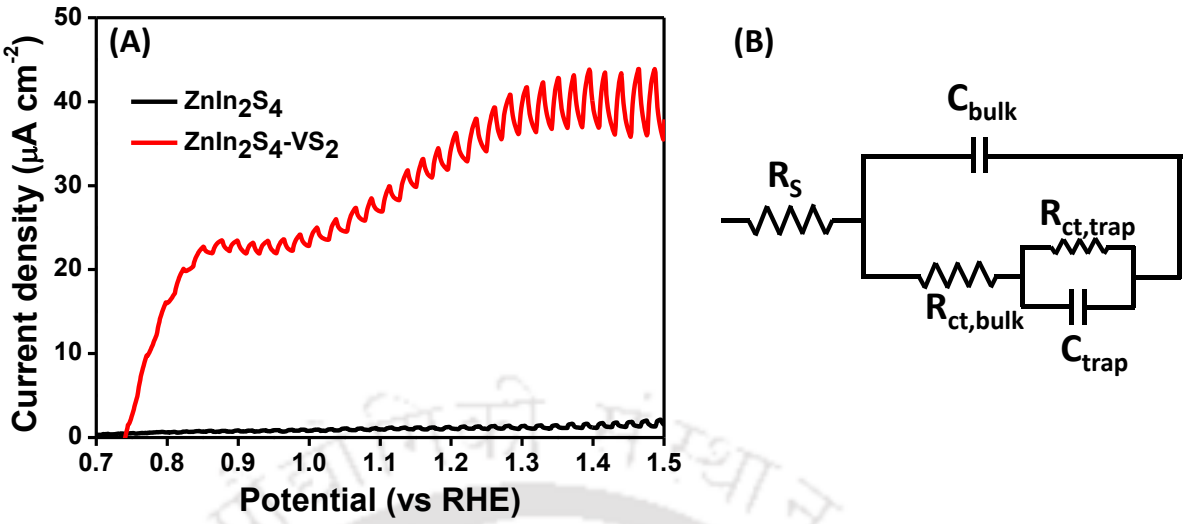

Figure 5.12: (A) J-V curve under continuous chopping of light at an interval of 2 sec for $ZnIn_2S_4$ and $ZnIn_2S_4$–VS_2 and (B) Equivalent circuit model used to fit the Nyquist plots.

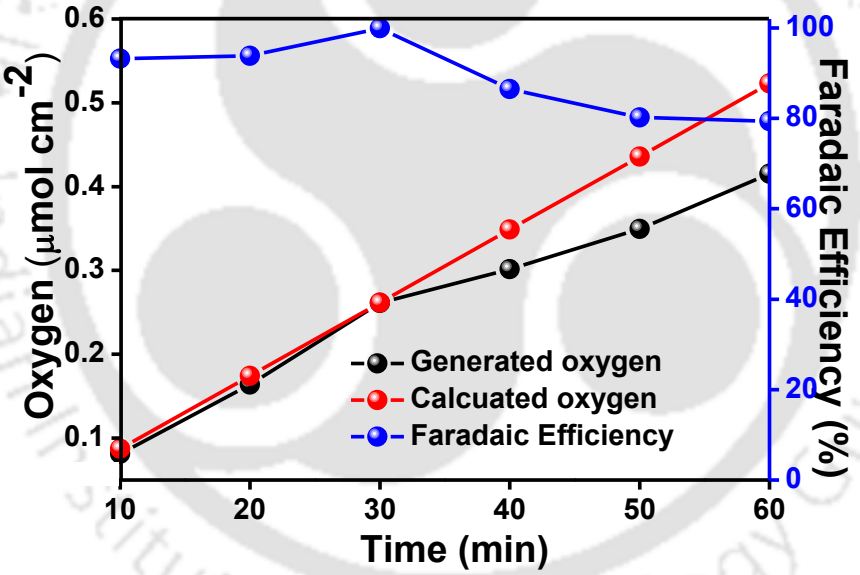

Figure 5.13: Calculated and measured oxygen generated and the corresponding Faradaic efficiency (%) at 10 min interval over a period of 60 min for $ZnIn_2S_4$–VS_2 photoanode under 1 sun illumination. The electrolyte used for the measurement of oxygen evolution is 0.5 M Na_2SO_4.

In order to confirm that the generated photocurrent is due to water oxidation and not due to the undesired side reactions or photocorrosion of the electrode, Faradaic efficiency of $ZnIn_2S_4$-VS_2 photoanode was measured as shown in **Figure 5.13**. Faradaic efficiency upto

99% was obtained with an average of 89% indicating that most of the photogenerated charge carriers were consumed for water oxidation.

Table 5.3: Literature Survey of different $ZnIn_2S_4$ based systems utilized for photocurrent measurements using Na_2SO_4 electrolyte

System	Electrolyte	Photocurrent density ($\mu A\ cm^{-2}$)	Reference
MoS_2/Cu- $ZnIn_2S_4$	0.5 M Na_2SO_4	~ 2.78 (~ 9 times improvement)	44
MoS_2/ $ZnIn_2S_4$	0.4 M Na_2SO_4	~ 0.6 (~ 10 times improvement)	2
$ZnIn_2S_4$–g-C_3N_4	0.5 M Na_2SO_4	~ 0.35 (~ 1.7 times improvement)	45
2D/2D g-C_3N_4 @ $ZnIn_2S_4$	1 M Na_2SO_4	~ 1.5 (~ 3 times improvement)	46
Carbon dots on $ZnIn_2S_4$ microspheres	0.5 M Na_2SO_4	~ 0.13 (~ 1.6 times improvement)	47
$ZnIn_2S_4$/TiO_2	0.5 M Na_2SO_4	~ 800 (~ 4 times improvement)	48
$ZnIn_2S_4$/UiO-66	1 M Na_2SO_4	~ 4.5 (~ 2.5 times improvement)	49
MoS_2/ $ZnIn_2S_4$	0.2M Na_2SO_4	~ 8.43 (~ 1.4 times improvement)	50
MoS_2/ $ZnIn_2S_4$	0.1M Na_2SO_4	~ 10 (~ 1.3 times improvement)	51
MoS_2-graphene/ $ZnIn_2S_4$	0.4 M Na_2SO_4	~ 6.98 (~ 4 times improvement)	52
RGO on $ZnIn_2S_4$	0.4 M Na_2SO_4	~ 18 (~ 18 times improvement)	53
$ZnIn_2S_4$-VS_2	**0.5 M Na_2SO_4**	**~ 3 ($ZnIn_2S_4$) ~ 56 ($ZnIn_2S_4$-VS_2) (18 times improvement)**	**This work**

5.4 CONCLUSION

In conclusion, we have synthesised $ZnIn_2S_4$–VS_2 composite for the first time and proposed it for a direct Z–scheme mechanism. A better charge separation in the composite results in extraordinary increment in photocurrent density of ~ 18 fold compared to bare

counterpart, $ZnIn_2S_4$. The significant improvement of photoelectrochemical property was further corroborated by the increased charge transfer efficiency and enhanced charge collection at the photoelectrode surface in $ZnIn_2S_4$–VS_2 from EIS experiments. This work opens up scope of designing new Z–scheme composite and understanding the charge carrier dynamics in photoelectrode contributing to enhanced photoelectrochemical efficiency.

5.5 REFERENCES

1. Z. Lei, W. You, M. Liu, G. Zhou, T. Takata, M. Hara, K. Domen and C. Li, *Chem. Commun.*, 2003, **0**, 2142.
2. W. Li, Z. Lin and G. Yang, *Nanoscale*, 2017, **9**, 18290.
3. W. Yang, L. Zhang, J. Xie, X. Zhang, Q. Liu, T. Yao, S. Wei, Q. Zhang and Y. Xie, *Angew. Chem. Int. Ed*., 2016, **55**, 6716.
4. L. Yuan, M. –Q. Yang and Y. –J. Xu, *J. Mater. Chem. A*, 2014, **2**, 14401.
5. Q. Liu, H. Lu, Z. Shi, F. Wu, J. Guo, K. Deng and L. Li, *ACS Appl. Mater. Interfaces*, 2014, **6**, 17200.
6. M. A. Mahadik, P. S. Shinde, M. Cho and J. S. Jang, *J. Mater. Chem. A*, 2015, **3**, 23597.
7. F. Shi, L. Shi, M. Chen and D. Jiang, *Chem. Commun.*, 2015, **51**, 17144.
8. W. –K. Jo and T. S. Natarajan, *J. Colloid Interface Sci*., 2016, **482**, 58.
9. N. Tian, H. Huang, Y. He, Y. Guo, T. Zhang and Y. Zhang, *Dalton Trans*., 2015, **44**, 4297.
10. G. Yang, D. Chen, H. Ding, J. Feng, J. Z. Zhang, Y. Zhu, S. Hamid and D. W. Bahnemann, *Appl. Catal., B*, 2017, **219**, 611.
11. Y. Bai, T. Chen, P. Wang, L. Wang, L. Ye, X. Shi and X. Bai, *Sol. Energy Mater. Sol. Cells*, 2016, **157**, 406.
12. D. Lu, H. Wang, X. Zhao, K. K. Kondamareddy, J. Ding, C. Li and P. Fang, *ACS Sustainable Chem. Eng.*, 2017, **5**, 1436.
13. C. Zeng, Y. Hu, T. Zhang, F. Dong, Y. Zhang and H. Huang, *J. Mater. Chem. A*, 2018, **6**, 16932.
14. J. Low, C. Jiang, B. Cheng, S. Wageh, A. A. Al- Ghamdi and J. Yu, *Small Methods*, 2017, **1**, 1700080.

15. Y. Qu, H. Pan, C. T. Kwok and Z. Wang, *Phys. Chem. Chem. Phys.*, 2015, **17**, 24820.
16. Y. Qu, M. Shao, Y. Shao, M. Yang, J. Xu, C. T. Kwok, X. Shi, Z. Lu and H. Pan, *J. Mater. Chem. A*, 2017, **5**, 15080.
17. X. Chen, K. Yu, Y. Shen, Y. Feng and Z. Zhu, *ACS Appl. Mater. Interfaces*, 2017, **9**, 42139.
18. M. Shao, Y. Shao, S. Ding, J. Wang, J. Xu, Y. Qu, X. Zhong, X. Chen, W. F. Ip, N. Wang, B. Xu, X. Shi, X. Wang and H. Pan, *Appl. Catal., B*, 2018, **237**, 295.
19. Y. Chen, S. Hu, W. Liu, X. Chen, L. Wu, X. Wang, P. Liu and Z. Li, *Dalton Trans.*, 2011, **40**, 2607.
20. B. Chai, T. Peng, P. Zeng, X. Zhang and X. Liu, *J. Phys. Chem. C*, 2011, **115**, 6149.
21. X. Shi, M. Fujitsuka and T. Majima, *Appl. Catal., B*, 2018, **235**, 9.
22. H. Li, L. Liu, Z. Wang, X. Zheng, S. Meng, S. Chen and X. Fu, *RSC Adv.*, 2018, **8**, 11489.
23. B. Gao, L. Liu, J. Liu and F. Yang, *Applied Catal. B,* 2013, **129**, 89.
24. C. V. Reddy, J. Shim and M. Cho, *J. Phys. Chem. Solids*, 2017, **103**, 209.
25. R. Karthikeyan, D. Thangaraju, N. Prakash and Y. Hayakawa, *CrystEngComm.*, 2015, **17**, 5431.
26. R. S. Ganesh, S. K. Sharma, E. Durgadevi, M. Navaneethan, H. S. Binitha, S. Ponnusamy, C. Muthamizhchelvan, Y. Hayakawa and D. Y. Kim, *Superlattices Microstruct.*, 2017, **104**, 247.
27. W. Fang, H. Zhao, Y. Xie, J. Fang, J. Xu and Z. Chen, *ACS Appl. Mater. Interfaces*, 2015, **7**, 13044.
28. Y. Xie, Y. Liu, H. Cui, W. Zhao, C. Yang and F. Huang, *J. Power Sources*, 2014, **265**, 62.
29. S. Shen, L. Zhao, X. Guan and L. Guo, *J. Phys. Chem. Solids*, 2012, **73**, 79.
30. P. He, M. Yan, G. Zhang, R. Sun, L. Chen, Q. An and L. Mai, *Adv. Energy Mater.,* 2017, **7**, 1601920.
31. T. M. Masikhwa, F. Barzegar, J. K. Dangbegnon, A. Bello, M. J. Madito, D. Momodu and N. Manyala, *RSC Adv.*, 2016, **6**, 38990.

32. D. Yoo, J. Kim, S. H. Lee, W. Cho, H. H. Choi, F. S. Kim and J. H. Kim, *J. Mater. Chem. A*, 2015, **3**, 6526.
33. K. G. Chandrappa and T. V. Venkatesha, *Nano-Micro Lett.*, 2012, **4**, 14.
34. J. Hou, C. Yang, H. Cheng, Z. Wang, S. Jiao and H. Zhu, *Phys. Chem. Chem. Phys.*, 2013, **15**, 15660.
35. J. Zhang, C. Zhang, Z. Wang, J. Zhu, Z. Wen, X. Zhao, X. Zhang, J. Xu and Z. Lu, *Small*, 2018, **14**, 1703098.
36. Y. Wang, Z. Sofer, J. Luxa and M. Pumera, *Adv. Mater. Interfaces*, 2016, **3**, 1600433.
37. H. Liang, H. Shi, D. Zhang, F. Ming, R. Wang, J. Zhuo and Z. Wang, *Chem. Mater.*, 2016, **28**, 5587.
38. Y. Wang, L. Liu, C. Meng, Y. Zhou, Z. Gao, X. Li, X. Cao, L. Xu and W. Zhu, *Sci. Rep.*, 2016, 33092.
39. H. Shi, H. Liang, F. Ming and Z. Wang, *Angew. Chem.*, 2017, **129**, 588.
40. J. Fu, S. Cao and J. Yu, *Journal of Materiomics*, 2015, **1**, 124.
41. M. A. Mahadadalkar, S. W. Gosavi and B. B. Kale, *J. Mater. Chem. A*, 2018, **6**, 16064.
42. J. Bisquert, G. G. -Belmonte, A. Munar, M. Sessolo, A. Soriano and H. J. Bolink, *Chem. Phys. Lett*, 2008, **465**, 57.
43. J. Reichman, *Appl. Phys. Lett.*, 1980, **36**, 574.
44. Y. Yuan, D. Chen, J. Zhong, L. –X. Yang, J. Wang, M. –J. Liu, W. –G. Tu, Z. –T. Yu and Z. -G. Zou, *J. Mater. Chem. A*, 2017, **5**, 15771.
45. H. Liu, Z. Jin, Z. Xu, Z. Zhang and D. Ao, *RSC Adv.*, 2015, **5**, 97951.
46. B. Lin, H. Li, H. An, W. Hao, J. Wei, Y. Dai, C. Ma and G. Yang, *Appl. Catal., B*, 2018, **220**, 542.
47. W. Shi, H. Lv, S. Yuan, H. Huang, Y. Liu and Z. Kang, *Sep. Purif. Technol*, 2017, **174**, 282.
48. I. B. Assaker, M. Gannouni, J. B. Naceur, M. A. Almessiere, A. L. A. -O, T. Ghrib, S. Shen and R. Chtourou. *Appl. Surf. Sci.*, 2015, **351**, 927.
49. B. Liu, X. Liu, J. Liu, C. Feng, Z. Li, C. Li, Y. Gong, L. Pan, S. Xu and C. Q. Sun, *Appl. Catal., B*, 2018, **226**, 234.

50. Z. Zhang, L. Huang, J. Zhang, F. Wang, Y. Xie, X. Shang, Y. Gu, H. Zhao and X. Wang, *Appl. Catal., B*, 2018, **233**, 112.
51. C. Liu, B. Chai, C. Wang, J. Yan and Z. Ren, *Int. J. Hydrogen Energy*, 2018, **43**, 6977.
52. Y. –J. Yuan, J. –R. Tu, Z. –J. Ye, D. –Q. Chen, B. Hu, Y. –W. Huang, T. –T. Chen, D. –P. Cao, Z. -T Yu and Z. –G. Zou, *Appl. Catal., B*, 2016, **188**, 13.
53. Y. Xia, Q. Li, K. Lv, D. Tang and M. Li, *Appl. Catal., B*, 2017, **206**, 344.

Chapter 6

Thesis Overview and Future Scope

This chapter briefly summarizes the overall findings and outcome of this thesis. It also highlights few promising prospects which could be carried out in future for further improvement of photocatalytic properties.

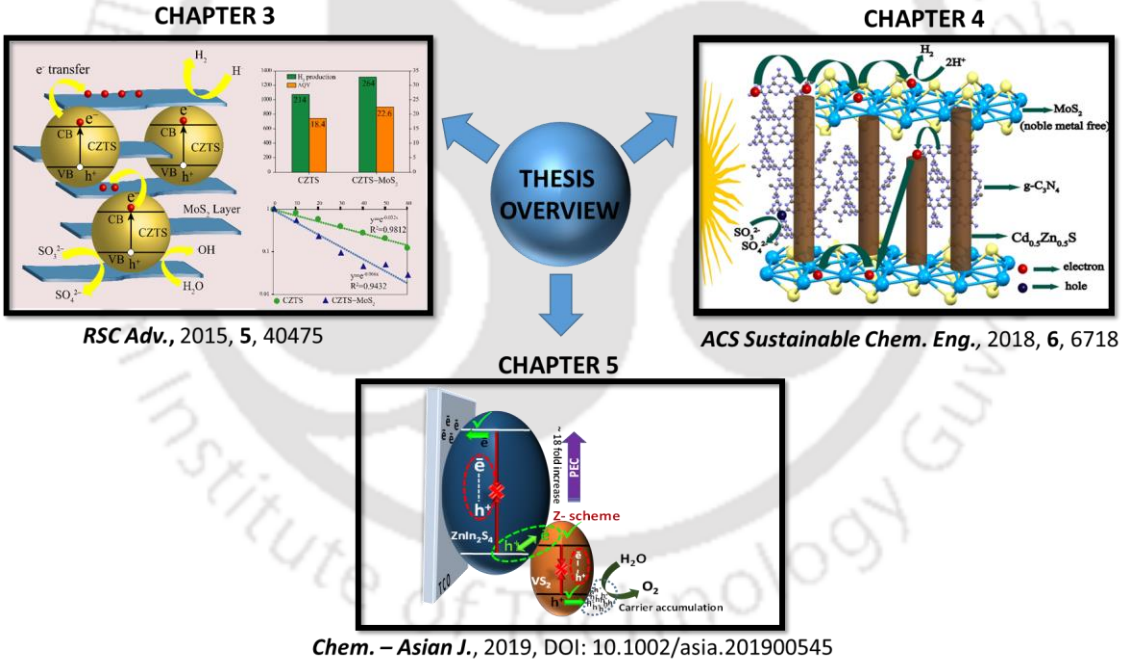

Thesis Overview:

The present thesis describes the development of multinary sulfide based semiconductor materials for utilization as efficient photocatalysts for water reduction/oxidation or dye degradation. The bare sulfide semiconductor materials are modified basically by adopting the strategy of heterojunction formation with other suitable photocatalyst materials for efficient separation of photogenerated charge carriers which is one of the prime condition to be satisfied by a semiconductor for efficient photocatalytic activity. Besides, the heterojunctions also show visible light absorption, high surface area due to the hierarchical morphology of the components and an increased number of active sites due to co–catalyst loading which further supplements enhanced photocatalytic activity. A detailed mechanistic insight of the favouable charge carrier dynamics in these model systems were carried out by several experimental techniques which proves as a scope of understanding the mechanism of similar heterojunctions with enhanced activity. In **Chapter 1**, we have discussed the basic principles of photocatalytic processes and have given an overview of the recent progress of sulfide based semiconductors in these field. **Chapter 2** describes all the synthesis and characterisation techniques along with the adopted photocatalytic evaluation parameters**. Chapter 3, 4 and 5** consists details of the work carried out and included in this thesis. The summary of each chapter is given below.

In **Chapter 3** we have utilised a quaternary semiconductor, Cu_2ZnSnS_4 and modified it by making a heterojunction with a cocatalytst, MoS_2. The components have a favourable band alignment for the photogenerated electrons in Cu_2ZnSnS_4 to be transferred to MoS_2, which being a highly active co–catalyst material provides active site for water reduction to generate H_2 efficiently. Both Cu_2ZnSnS_4 and the composite Cu_2ZnSnS_4–MoS_2 were studied for photocatalytic H_2 generation and degradation of a pollutant dye, Rhodamine B. It is observed that the activity of photocatalytic H_2 production is ~ 20% higher in the composite than in the bare counterpart. The rate of degradation of Rhodamine B dye is also observed to be almost twice in the composite than in bare Cu_2ZnSnS_4. The increase in the rate of photocatalytic activity is due to the efficient separation of photogenerated charge carriers in the composite. Further, experiments were also carried out to determine the active species involved in the dye degradation process by using various active species scavengers. Hydroxyl radical ($OH^{\bullet}$) was found to be the active species in controlling the kinetics of the dye degradation.

In **Chapter 4** we present a noble–metal free ternary hierarchical composite of $Cd_{0.5}Zn_{0.5}S$ intercalated with g-C_3N_4 sheets and loaded with a co–catalyst, MoS_2 for an excellent photocatalytic activity owing to its enhanced interfacial charge transfers leading to a reduced photoinduced charge carrier recombination for efficient H_2 generation as well as degradation of an organic pollutant, Rhodamine B dye. The binary and ternary composite reveals an enhancement in the yield of H_2 production by ~ 120% ($Cd_{0.5}Zn_{0.5}S$–g-C_3N_4) and ~ 197% ($Cd_{0.5}Zn_{0.5}S$–g-C_3N_4-MoS_2) compared to bare $Cd_{0.5}Zn_{0.5}S$. Taking Rhodamine B dye as a model system, it is observed that the rate of degradation is much higher in $Cd_{0.5}Zn_{0.5}S$–g-C_3N_4–MoS_2 in comparison to $Cd_{0.5}Zn_{0.5}S$ and $Cd_{0.5}Zn_{0.5}S$–g-C_3N_4. Active species trapping experiments confirmed that $O_2^{\bullet-}$ is the main active species in the photo–oxidation of the dye. An extensive study of the mechanism of charge transfer in the composite was carried out by several instrumental techniques like XPS, PL, TRPL etc. The charge carrier dynamics as established by various experimental analyses confirms the favourable charge transfer pathways in the composite owing to the suitable band alignment which contributes to the increased availability of photogenerated electrons in the composite, preventing recombination.

In **Chapter 5** we have designed a composite of $ZnIn_2S_4$ with VS_2 to form a novel direct Z–scheme and studied its photoelectrochemical properties. The composite shows a significantly improved (~ 18 fold) photocurrent over bare counterpart, $ZnIn_2S_4$. $ZnIn_2S_4$–VS_2 is experimentally proven to form a direct Z–scheme heterostructure which leads to efficient separation of photogenerated electron–hole pair. A thorough investigation of dynamics of charge transfer in the composite is carried out by EIS experiments. The intrinsic electronic charge transport properties in the bulk and interface of the photoelectrode obtained from the EIS data proves a favourable movement of charge carriers both in bulk and at the surface states in the composite leading to an enhanced photocurrent. Also, a slow kinetics of charge transfer through the surface states is observed which leads to dark current providing significant current contribution even in the absence of light.

Future Scope:

We have observed that the research findings in this thesis work provides an ample scope for design and development of heterojunction photocatalysts based on suitable band alignment, and offers detailed understanding of the charge transfer mechanism in the heterostructure. However, there is still scope for further extension of this research work. Few of the research scopes for future study might be as follows:

- In order to prevent from the intrinsic drawback of photocorrosion, sulfide photocatalysts can be made composite with oxide materials with layered structure or integrated with a protective layer of oxide materials
- Being polymorphic in nature, sulfide based semiconductors can be studied for their phase dependent photocatalytic activities
- Another scope of study is the control of crystallinity in sulfide materials in order to prevent defect states which act as recombination centers
- As sulfide materials have several defect/trap states, a deeper understanding of the defect properties of these compounds would be useful to prepare materials with high quality suitable for photocatalysis
- Combining sulfide based semiconductors with electro catalytic materials for use in photoelectrochemical process
- Utilisation of these optimised semiconductor photocatalysts along with suitable counter electrode materials to form tandem cell for photoelectrochemical water splitting

List of Publications and Conferences Attended

Journal Articles

1) A Z-Scheme Strategy Utilizing $ZnIn_2S_4$ and Hierarchical VS_2 Microflowers with Improved Charge Carrier Dynamics for Superior Photoelectrochemical Water Oxidation. **G. Gogoi**, C. T. Moi, A. S. Patra, D. Gogoi, N. R. Peela and M. Qureshi, ***Chem. – Asian J.,*** 2019, DOI: 10.1002/asia.201900545.
2) Hybrid of g-C_3N_4 and MoS_2 Integrated onto $Cd_{0.5}Zn_{0.5}S$: Rational Design with Efficient Charge Transfer for Enhanced Photocatalytic Activity. **G. Gogoi**, S. Keene, A. S. Patra, T. K. Sahu, S. Ardo and M. Qureshi, *ACS Sustainable Chem. Eng.*, 2018, **6**, 6718.
3) Quaternary semiconductor Cu_2ZnSnS_4 loaded with MoS_2 as a co-catalyst for enhanced photo-catalytic activity. **G. Gogoi**, S. Arora, N. Vinothkumar, M. De and M. Qureshi, *RSC Adv.*, 2015, **5**, 40475.
4) Design of noble metal free hierarchical VS_2 onto WO_3 nanoflakes as an effective heterojunction strategy for enhanced photoelectrochemical water oxidation. C. T. Moi, **G. Gogoi**, T. K. Sahu, D. Gogoi, N. R. Peela and M. Qureshi, ***Sustainable Energy Fuels***, 2019, DOI: 10.1039/C9SE00719A.
5) Combined Experimental and Theoretical Insights into the Synergistic Effect of Cerium Doping and Oxygen Vacancies in $BaZrO_{3-\delta}$ Hollow Nanospheres for Efficient Photocatalytic Hydrogen Production. A. S. Patra, M. S. Chauhan, S. Keene, **G. Gogoi**, K. A. Reddy, S. Ardo, D. L. V. K. Prasad and M. Qureshi, *J. Phys. Chem. C*, 2019, **123**, 233.
6) Effect of surface overlayer in enhancing the photoelectrochemical water oxidation of *in situ* grown one-dimensional spinel zinc ferrite nanorods directly onto the substrate. T. K. Sahu, A. K. Shah, **G. Gogoi**, A. S. Patra, M. S. Ansari and M. Qureshi, *Chem. Commun.*, 2018, **54**, 10483.
7) Ordered-Disordered $BaZrO_{3-\delta}$ Hollow Nanosphere/Carbon Dot Hybrid Nanocomposite: A New Visible-Light-Driven Efficient Composite Photocatalyst for Hydrogen Production and Dye Degradation. A. S. Patra, **G. Gogoi**, M. Qureshi, *ACS Omega,* 2018, **3**, 10980.

8) Modulating the electronic structure of lanthanum manganite by ruthenium doping for enhanced photocatalytic water oxidation. A. S. Patra, **G. Gogoi**, R. K. Sahu and M. Qureshi, *Phys. Chem. Chem. Phys.*, 2017, **19**, 12167.

9) Noble metal-free counter electrodes utilizing Cu_2ZnSnS_4 loaded with MoS_2 for efficient solar cells based on ZnO nanowires co-sensitized with $CuInS_2$–CdSe quantum dots. D. Barpuzary, A. Banik, **G. Gogoi** and M. Qureshi, *J. Mater. Chem. A*, 2015, **3**, 14378.

Conferences Attended

1) 3th International Conference on Advanced Nanomaterials and Nanotechnology (**ICANN-2013**), 1st-3rd December, 2013, Indian Institute of Technology Guwahati, Guwahati, India (*Attended*).

2) International Conference on Advances in Nanomaterials and Nanotechnology (**ICANN-2016**), 4th-5th November, 2016, Jamia Millia Islamia, New Delhi, India (*Poster presented*).

3) National Conference on Frontiers in Chemical Sciences (**FICS-2016**), 8th-10th December, 2016, Indian Institute of Technology Guwahati, Guwahati, India (*Poster presented*).

4) 20th CRSI National Symposium in Chemistry, 3rd-5th February, 2017, Department of Chemistry, Gauhati University, Guwhatai, India (*Poster presented*).

5) 3rd National Workshop on NEMS/MEMS and Theranostic Devices, 21st-23rd March, 2017, Centre for Nanotechnology, Indian Institute of Technology Guwahati, Guwahati, India (*Participated*).

6) One–Day Workshop on Vacuum Technology and its Application in Optical Science, 19th August, 2017, Department of Physics, Indian Institute of Technology Guwahati, Guwahati, India (*Paticipated*)

7) 5th International Conference on Advanced Nanomaterials and Nanotechnology (**ICANN-2017**), 18th-21st December, 2017, Indian Institute of Technology Guwahati, Guwahati, India (*Poster presented*).

8) Conference on Advances in Catalysis for Energy and Environment (**CACEE-2018**), 10th-12th January, 2018, Tata Institute of Fundamental Research (TIFR), Mumbai, India (*Poster presented*).

9) Frontiers in Chemical Sciences (**FICS-2018**), 6th-8th December, 2018, Department of Chemistry, Indian Institute of Technology Guwahati, Guwahati, India (*Poster presented*).